



FLINDERS UNIVERSITY
College of Science and Engineering

New Generation Titanium Alloys with Low Elastic Modulus for Orthopaedic Implants

Submitted in partial fulfilment of the requirements for the
Master of Engineering (Materials)

Author: Magdalen H.C. Tan

Supervisors: Dr. Reza Oskouei & A/Prof. Reza Ghomashchi

Date Submitted: 15-October-2018

This page is intentionally left blank

Declaration

I certify that this thesis does not incorporate without acknowledgment any material previously submitted for a degree or diploma in any university; and that to the best of my knowledge and belief it does not contain any material previously published or written by another person except where due reference is made in the text.

Signed: _____

Date: 15/10/2018

This page is intentionally left blank

Acknowledgments

I would like to sincerely thank Dr Reza H. Oskouei and A/Prof. Reza Ghomashchi for their guidance and continuous support throughout the whole process of the project. Their passion, motivation, encouragement and enthusiasm has determined me to complete the project at my highest standard possible. Their dedication to my project was paramount and beyond my expectations, and their willingness to share their vast array of knowledge was admirable.

My sincere thanks also to Professor Wenlong Xiao from Beihang University, Beijing, China for his assistance with the fabrication of samples.

Thanks to Mr. Alireza Baghi for his assistance with sample preparation, characterisation and testing.

Finally, and most importantly, I am thankful to my close friends and family for their advice and encouragement throughout the challenging yet exciting period of the project. I would like to specifically thank my mum, sister and brother, who keep me in their prayer and also their unconditional love and support to keep me going.

This page is intentionally left blank

Abstract

Total hip replacement (THR) has progressively become a common treatment for patients with osteoarthritis or hip damage, which involves mostly the ageing population. The expectant rapid growth of the ageing population thus has necessitated a steady demand for the THR market. However, the current biomaterials used to fabricate the THR implants are found having much higher Young's moduli compared to the bones and thus resulted in stress-shielding that causes failure and surgery revision. Owing to these circumstances, studies and research to develop biomaterials with Young's moduli closer to that of cortical bones are gaining an extensive attention. This study therefore aims to investigate and develop titanium-based alloys (Ti-Nb-Zr) with new chemical composition which offer Young's moduli lower than 50GPa.

The alloys were designed after extensive research on the alloying effect, phase analysis, and the comparison of previously fabricated Ti-Nb-Zr alloys (of different compositions). Three alloys were therefore designed for investigation including Ti-23Nb-7Zr (sample 1), Ti-28Nb-7Zr (sample 2) and Ti-33Nb-7Zr (sample 3). Thermo Calc Software was utilised to predict the phases formed within the designated alloys prior to the fabrication process. The alloys were fabricated using a non-consumable vacuum arc melting furnace through the courtesy of Beihang University. Samples for microstructure examination and X-ray diffraction (XRD) analysis were prepared in accordance to the ASM standard (Volume 9: Metallography and Microstructures of Titanium and Its Alloys). Microstructures were observed under both optical microscope and scanning electron microscope (SEM). Hardness of the alloys were compared through microhardness and nanoindentation testing. The nanoindentation system was also employed to calculate the Young's modulus of the alloys. The XRD analysis was carried out to identify the phases present in the alloys after the casting and solution treatment process.

The microstructure results showed a platelike martensitic (α'') structure in the beta (β) matrix. The martensitic structure was most distinct and coarser in sample 1, with decreasing amount and coarseness towards sample 3. Basketweave and Widmanstätten patterns were also observed which resembles the α'' distorted alpha structure. The XRD analysis exhibited the presence of two phases which are alpha (α'') and beta (β). As the most important finding, all the three fabricated alloys were measured to have a significantly reduced stiffness level as they offer a Young's modulus of 40.0, 37.5 and 41.5 GPa that are all less than the initial target of 50GPa.

The findings of this project are being proposed for publication in a relevant journal such as the Journal of Alloys and Compounds (a manuscript will be submitted in Dec 2018).

Table of Contents

1.0 Introduction.....	1
1.1 Introduction	2
2.0 Literature Review	5
2.1 Metallic Load-bearing Orthopaedic Implants.....	6
2.2 Currently Used Metallic Biomaterials and Their Limitations.....	7
2.2.1 Stainless Steel 316L.....	7
2.2.2 Cobalt-Chromium Alloys	9
2.2.3 Ti-6Al-4V.....	10
2.3 Requirements and Limitations of Biomaterials.....	12
2.3.1 Mechanical Properties.....	12
2.3.1.1 Stress Shielding	12
2.3.2 Biocompatibility	13
2.3.3 Corrosion Resistance.....	14
2.4 New Generation of Titanium alloys for Implants.....	15
2.4.1 Advantages of Ti-alloys Compares to Other Metallic Alloys	15
2.4.2 Early Development of New Generation Ti-alloys	15
2.4.3 β -type Ti-alloys with Nontoxic Elements	16
2.4.4 Heat Treatment and Strengthening Effects	19
2.4.5 Microstructure Characterization of Ti-Nb-Zr alloys.....	20
2.4.6 Different Methods Applied to Develop Low Young's Modulus Ti-alloys.....	22
2.5 Fabrication Methods for Titanium Alloys	23
2.5.1 Ball Milling/Powder Metallurgy.....	23
2.5.2 Arc Melting	24
2.6 β -type Ti-Nb-Zr Alloys.....	24
2.6.1 The Alloying Effects of Nb and Zr in Ti-alloys.....	25
2.6.2 Ternary Diagram for Ti-Nb-Zr Alloys	26
2.7 Research Objectives/Motivation	30
3.0 Methodology	33
3.1 Fabrication of β -phase Ti-Nb-Zr Alloys.....	34
3.1.1 Solution Treatment of Samples.....	35
3.1.2 Sectioning of Samples	35
3.2 Microstructure Characterization	37
3.2.1 Microstructure Examination.....	40
3.2.1.1 Optical Microscopic Observation.....	40
3.2.1.2 SEM with EDS Analysis	40

3.2.2	Thermo Calc Phase Analysis.....	42
3.2.3	Phase Analysis (XRD).....	42
3.3	Alloy assessment	43
3.3.1	Microhardness Measurements	43
3.3.2	Young’s Modulus and Nanoindentation.....	44
4.0	Results.....	48
4.1	Microstructure Results.....	49
4.1.1	Optical Microscopy.....	49
4.1.2	SEM Results	53
4.2	Thermo Calc Results	58
4.3	XRD analysis	60
4.4	Microhardness Results.....	61
4.5	Nanoindentation Results	64
4.6	Chemical Composition Results.....	66
4.7	Homogeneity.....	73
5.0	Discussion.....	76
5.1	Phases Analysis	77
5.2	Microscopy Analysis	78
5.2.1	Optical microscopy	78
5.2.2	Scanning Electron Microscopy.....	80
5.3	XRD Analysis	81
5.4	Microhardness.....	81
5.5	Nanoindentation	82
5.6	Homogeneity.....	84
5.7	Etching Process	84
6.0	Conclusions.....	87
6.1	Concluding Remarks	88
6.2	Suggestions for Future Work	89
7	References.....	90

List of Figures

Figure 1: Research plan.....	2
Figure 1: Component of a total hip replacement.....	6
Figure 3: Plot of Ti-Nb-Zr alloy vs Young's modulus with respect to Ti% in an increasing order.....	18
Figure 4: Plot of Ti-Nb-Zr alloy vs Young's modulus with respect to Nb% in an increasing order.....	18
Figure 5: Plot of Ti-Nb-Zr alloy vs Young's modulus with respect to Zr% in an increasing order.....	19
Figure 6: SEM ($\alpha+\beta$)-phase: Decomposition of undeformed α laths with precipitation of β phase between them.	21
Figure 7: Optical micrograph showing α' -phase after homogenized at (950 °C) for 5h, followed by water quenched and then solution treated at 900°C for 1h and water quenched ⁹⁰	21
Figure 8: Optical micrographs showing Widmanstätten α'' -phase (a) after water quenched from 1050°C with martensitic transformation and the formation of laths, (b) tempered at 750°C for 1hr after water quenched from 1050°C ⁵²	21
Figure 9: TEM dark-field images showing diffusion of ω phase.....	22
Figure 10: SEM images of acicular and lamellae α' phases.....	22
Figure 11: SEM images of primary, secondary, tertiary and quartic α' ; prior β grain boundary.....	22
Figure 12: Calculated isothermal diagram of the Ti-Nb-Zr system at 570°C ⁶⁷	26
Figure 13: Calculated liquidus surface projection in the Ti-Nb-Zr system ⁶⁷	27
Figure 14: Vacuum arc melting furnace schematic diagram.....	35
Figure 15: Sample shows homogeneous after melting and casting process.....	35
Figure 16: Wire Electric Discharge Machine (WEDM) from Toolcraft.....	36
Figure 17: Before and after sectioning the sample with WEDM.....	36
Figure 18: Diamond cutting machine used to cut the samples into adequate pieces for microscope and XRD test.....	37
Figure 19: 3-step, automatic grinding and polishing method for titanium alloys.....	38
Figure 20: Mounting machine for sample preparation.....	39
Figure 21: Polishing machine.....	39
Figure 22: Samples in etching process.....	39
Figure 23: ZEISS Optical Microscope used for porosity and microscope observation.....	40
Figure 24: Scanning Electron Microscope Quanta 450 with EDS Analyser.....	41
Figure 25: XRD Machine.....	43
Figure 26: LM 700AT Microhardness Tester.....	43
Figure 27: Matrix for microhardness measurements.....	44
Figure 28: IBIS Nanoindentation machine.....	45
Figure 29: Matrix for nanoindentation measurements.....	45

<i>Figure 30: Microhardness and Nanoindentation marks</i>	45
<i>Figure 31: Optical images of sample 1 – Ti-23Nb-7Zr</i>	49
<i>Figure 32: Optical images of sample 2 – Ti-28Nb-7Zr</i>	51
<i>Figure 33: Optical images of sample 3 – Ti-33Nb-7Zr</i>	52
<i>Figure 34: SEM micrographs for Ti-23Nb-7Zr</i>	53
<i>Figure 35: SEM micrographs for Ti-28Nb-7Zr</i>	55
<i>Figure 36: SEM micrographs for Ti-33Nb-7Zr</i>	56
<i>Figure 37: Comparison of acicular and lath martensitic structure</i>	57
<i>Figure 38: Ternary diagram for Ti-Nb-Zr alloy with increasing temperature, region of interest</i>	58
<i>Figure 39: Phase diagrams for the alloying elements with region of interest defined</i>	59
<i>Figure 40: XRD profiles for the three samples a) Ti-23Nb-7Zr, b) Ti-28Nb-7Zr, and c) Ti-33Nb-7Zr</i>	60
<i>Figure 41: Comparison of hardness points before and after etching and marking of points</i>	62
<i>Figure 42: The changes of Vickers hardness with increasing of Nb content%</i>	63
<i>Figure 43: Load-displacement curves for three samples. The curves were plotted through nanoindentation system</i>	65
<i>Figure 44: Comparison of Young's Modulus and Nanohardness with increasing of Nb Content %</i> ...	65
<i>Figure 45: Comparison of hardness in micro and nano scale</i>	66
<i>Figure 46: Electron Image for EDS analysis (Ti-23Nb-7Zr)</i>	66
<i>Figure 47: Chemical composition from EDS analysis for Ti-23Nb-7Zr</i>	67
<i>Figure 48: Spectrum analysis from EDS (Ti-23Nb-7Zr)</i>	68
<i>Figure 49: Electron Image for EDS analysis (Ti-28Nb-7Zr)</i>	69
<i>Figure 50: Chemical composition from EDS analysis for Ti-28Nb-7Zr</i>	70
<i>Figure 51: Spectrum analysis from EDS (Ti-28Nb-7Zr)</i>	70
<i>Figure 52: Electron Image for EDS analysis (Ti-33Nb-7Zr)</i>	71
<i>Figure 53: Chemical composition from EDS analysis for Ti-33Nb-7Zr</i>	72
<i>Figure 54: Spectrum analysis from EDS (Ti-33Nb-7Zr)</i>	72
<i>Figure 55: Mapping images of sample alloys via EDS analyser</i>	73
<i>Figure 56: Schematic phase diagram of titanium alloys with the decomposition products of the β-phase</i>	77
<i>Figure 57: The evolution process of α_p and α_s phases when cooled from a two-phase field in Ti-alloys</i>	78
<i>Figure 58: Microstructure of the nanoindentation</i>	83

List of Tables

<i>Table 1: Chemical compositions of SS 316L surgical implants (ASTM, 2000).....</i>	<i>8</i>
<i>Table 2: Mechanical properties of 316L Stainless Steel</i>	<i>8</i>
<i>Table 3: Chemical composition of cobalt chromium alloy (ASTM, 2000)¹⁰.....</i>	<i>9</i>
<i>Table 4: Mechanical properties of CoCr alloys</i>	<i>10</i>
<i>Table 5: Chemical composition of Ti-6Al-4V.....</i>	<i>10</i>
<i>Table 6: Mechanical properties of Ti-6Al-4V¹⁵</i>	<i>11</i>
<i>Table 7: Current metallic alloy in used as biomaterials by various manufacturers</i>	<i>11</i>
<i>Table 8: Mechanical properties of human bones.....</i>	<i>12</i>
<i>Table 9: Biological impact of some common alloying elements for implantation.....</i>	<i>14</i>
<i>Table 10: Some of the β-type Ti alloy developed and the Young's modulus.....</i>	<i>16</i>
<i>Table 11: Ti-Nb-Zr-Ta alloy in binary, ternary and quaternary combination and their Young's modulus^{12,22}</i>	<i>17</i>
<i>Table 12: Ti, Nb, Zr, Ta and their properties, Tm and price</i>	<i>24</i>
<i>Table 13: Table showing Ti-Nb-Zr alloys of different elements composition, their mechanical properties and arguments of findings from some articles.....</i>	<i>28</i>
<i>Table 14: Purity and wt% of Ti, Nb and Zr.....</i>	<i>34</i>
<i>Table 15: Operating conditions for quantitative analysis using EDS on Quanta 450 SEM.....</i>	<i>42</i>
<i>Table 16: Specifications for Nanoindentation.....</i>	<i>44</i>
<i>Table 17: Microhardness results of the samples (each of 7 points) with average and standard deviation</i>	<i>61</i>
<i>Table 18: Nanoindentation hardness and Young's modulus results for the samples (each of 24 points) with average and standard deviation.....</i>	<i>64</i>
<i>Table 19: Chemical composition from EDS analysis for Ti-23Nb-7Zr.....</i>	<i>67</i>
<i>Table 20: Chemical composition from EDS analysis for Ti-28Nb-7Zr.....</i>	<i>69</i>
<i>Table 21: Chemical composition from EDS analysis for Ti-33Nb-7Zr.....</i>	<i>71</i>

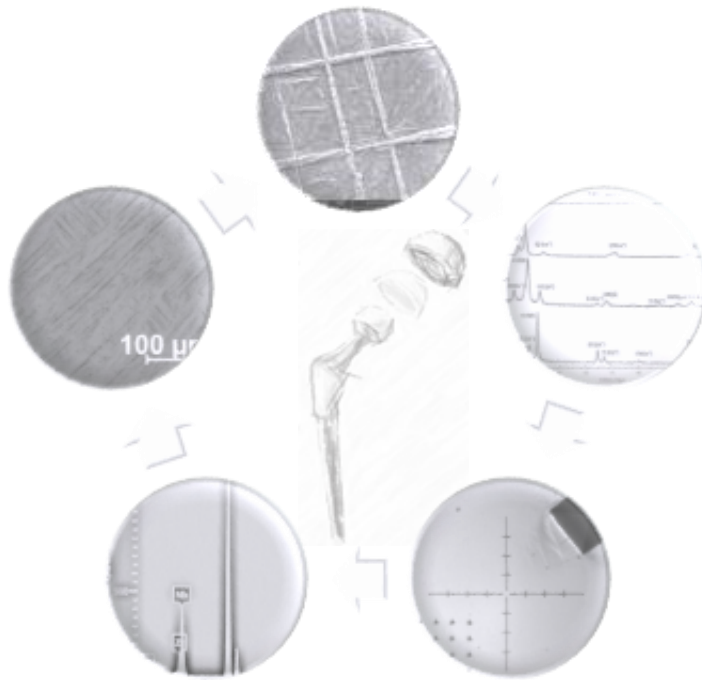
Nomenclature

BE	Blended Element
BCC	Body-centred Cubic
BSED	Backscattered Electron Detector
CALPHAD	Calculation of Phase Diagram
CCD	Charge-coupled Device
Co	Cobalt
Cr	Chromium
EDS	Energy Dispersive X-ray Spectrometry
GPa	Gigapascal (1×10^9 Pa)
g	Gram
HCP	Hexagonal Closed-packed
H ₂ O	Water
HF	Hydrofluoric Acid
HNO ₃	Nitric Acid
HV	Hardness Vickers
ht	Depth of Penetration
kg	Kilogram (1×10^3 g)
m	Metre
μm	Micrometre (1×10^{-6} m)
Mo	Molybdenum
MPa	Megapascal (1×10^6 Pa)
N	Newton
Nb	Niobium
Ni	Nickel
nm	Nanometre (1×10^{-9} m)

P	Force
PA	Pre-alloyed
SED	Secondary Electron Detector
SEM	Scanning Electron Microscope
THR	Total Hip Replacements
Ti	Titanium
Ti-6Al-4V	Titanium, 6 Aluminium, 4 Vanadium (Titanium alloy)
WEDM	Wire cut Electrical Discharge Machine
wt	Weight
XRD	X-ray Diffraction
Zr	Zirconium
α	Alpha
β	Beta
ω	Omega
$^{\circ}\text{C}$	Degree Celsius

This page is intentionally left blank

CHAPTER 1



Introduction

1.1 Introduction

Since the ageing population is continuously on the rise with growing demand in total hip or knee replacement, it is crucial to develop a compatible device that is sustainable. Although there has been a widespread adoption of stainless steel, Co-Cr alloy and Ti-6Al-4V as implant, all of these alloys pose a potential risk of toxicity when function *in vivo*. The discovery of Ti, Nb and Zr as non-toxic to human body has extensively promoted the scientific approach to further improve these alloys, especially in narrowing down the elasticity towards those of human bones. The evolution of Ti-Nb-Zr alloy and its impact in biomedical implant has provided the underlying principles or concepts of the research in biomedical field.

The nature of this research is empirical whereby the main focus is on Ti-Nb-Zr alloy. This research plan aims to identify the key factors that determine the Young's modulus of the Ti-Nb-Zr alloys and thus to derive a new proportion of element that yields a closer Young's modulus to the bone. The plan (Figure 1) will incorporate a whole process started with the literature review of the alloy, followed by three essential constituents of the experimental procedures which are alloy fabrication, alloy characterisation and alloy assessment. There will be further elaborated in the following sections.

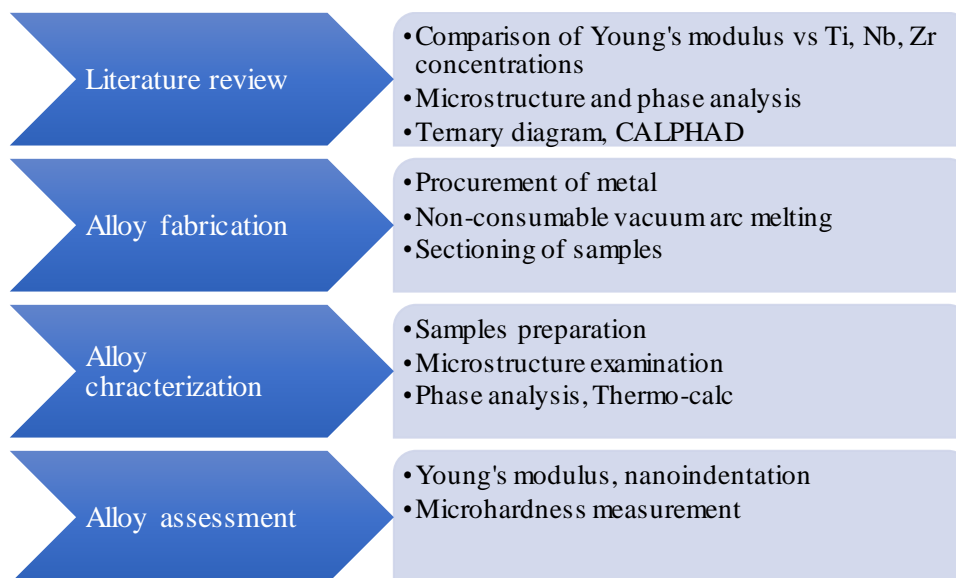


Figure 1: Research plan

One of the main purposes of literature review is to observe the relationship between the alloys' composition and their Young's moduli. Three graphs with an increasing order of Ti%, Nb% and Zr% in Ti-Nb-Zr alloys with regards to Young's modulus were plotted. The graphs serve as a purpose to monitor the effect of element composition on the Young's modulus value. Another objective of literature review is to analyse the implication of different phases in alteration of Young's modulus. The

ternary diagram for Ti-Nb-Zr alloy was produced with Thermo-Calc software, one of the methods available in CALPHAD. It represents an equilibrium state with either axes for temperature or composition of a chemical system or both. It allows the implication of stable or metastable regions and simulates the substances or solutions that existed within a certain amount of element at a temperature without actual experimental works¹. Through this program, prediction of phases present in the alloy at various element portion across a wide range of temperature can be identified. The collaboration between the amount of each elements and the phases can be linked to Young's modulus value.

The structural planning and conceptual design of the methodologies are shaped through the objectives listed in Section 2.7. The design method of this thesis not only relies on the observation, analysis from the literature review alone, experiments will be carried out to gather evidence to support the hypothesis and assumptions made. Problems concerning the fabrication method, the implication behind lowering the modulus of elasticity and the alloy's proportion will be discussed in the literature review. The intended experiments together with the justification of the approach made will be highlighted in the methodology section. Employment of various techniques to be applied in the search of the relationship will be presented as well.

The result chapter aims to describe the findings and outcomes of the experiments or testings being conducted. Microscopy images obtained from both optical microscope and scanning electron microscope (SEM) will be displayed accordingly. Following that, the phases identified from X-ray diffractometer and predicted with Thermo Calc will be presented sequentially. Additionally, the results from microhardness and nanoindentation testing will be listed. The last section in this chapter will be based on the chemical composition analysis and the mapping of homogeneity obtained from energy-dispersive X-ray spectroscopy (EDS).

The discussion section will serve a purpose to analyse extensively all the results obtained and justify them against the information retrieved from the literature review. The relationship of Ti, Nb and Zr concentration in determining the microstructure and phases of the alloys will be derived. Most importantly, the implication on the modulus of elasticity of these alloys will be compared and highlighted.

This thesis will end with the conclusion chapter whereby it summarises all information from the beginning of the research such as literature review, methodologies employed, results explored, justification reached to the final achievement. This chapter will also include suggestions for future work to deliver recommendations on how these alloys could be further verified as potential and competitive biomaterials as biomedical implant.

This page is intentionally left blank

CHAPTER 2



Literature Review

- 2.1 Metallic Load-bearing Orthopaedic Implants
- 2.2 Currently Used Metallic Biomaterials & Their Limitations
- 2.3 Requirements and Limitations of Biomaterials
- 2.4 New Generation of Titanium Alloys in Orthopaedic Implants
- 2.5 Fabrication Method for Titanium Alloys
- 2.6 β -type Ti-Nb-Zr Alloys
- 2.7 Research Objectives/Motivation

2.1 Metallic Load-bearing Orthopaedic Implants

Orthopaedic implants are not new. Owing to the high demand in replacement of failed soft and hard tissues with mainly artificial prostheses due to the fast-growing ageing population, extensive research has been always carried out to continuously improve them. The common damaged tissues associated with orthopaedic conditions are arthritis, acute fractures, trauma, joint and bone diseases. One of the distinguished prostheses components is the total hip replacement, as shown in Figure 1.

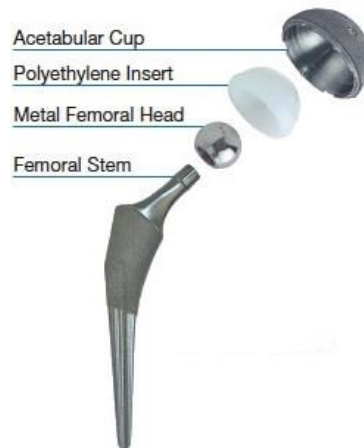


Figure 1: Component of a total hip replacement²

The total hip replacement is designed to relieve pain and to restore function of body mobility (walking, running, squatting) in addition to withstand the weight bearing of a patient. Thus, load bearing is one essential criterion to define a successful total hip replacement invention. Metallic biomaterials are the most suitable to replace the damaged or diseased hard tissue currently due to their excellent resistance to hold heavy weights. The importance of metallic biomaterials is more significant as 70-80% of the total hip replacement could be manufactured from metal, and they are acetabular cup, femoral head and stem (Figure 1).

The substantial increasing number of hip replacements has a great impact on the developed nations due to the immense growing proportion of the ageing population. According to Dr. Mark Pagnano, chairman of the department of orthopaedic surgery at the Mayo Clinic in Rochester, Minn, 2015, he commented the evolution of hip replacements will remain as the most considerable and effective ways to alleviate the pain of patients with knee and hip arthritis³.

Based on Australian Institute of Health and Welfare (AIHW) research data, among the surgeries in Australian hospitals from 2010 to 2011, knee disorder was the main reason, whereas hip fracture was ranked one of the five most common causes for inpatient surgery. Moreover, the number of knee replacement had drastically increased from 128 per 100,000 population in 2004 to 169 per 100,000

population in 2014. Similarly, the amount of hip replacement also picked up from 83 to 104 per 100,000 population during the same period⁴.

The prominent growth of the ageing population in Australia has also driven the demand of orthopaedic implants. AIHW data showed that in 2016, the number of people aged 65 and above is 3.7 million (15%). By 2056, it is predicted the population of elder Australians will expand to 8.7 million (22% of the population); and, it is projected it will go as high as 12.8 million people (25%) by 2096⁵.

Australian Orthopaedic Association National Joint Replacement Registry revealed the numbers of revision hip replacements and knee replacements in 2014 were 4,307 and 4,104 cases respectively. AIHW also claimed a 5% chance of revision surgery within 10 years of a hip or knee replacement. The data also showed an increase of 19.2% hip replacement in the private sector whereas 33.8% in the public sector in between 2003 and 2014. Simultaneously, revision knee replacements recorded a hike of 78.1% and 75.3% in the private and public sector respectively⁴.

The statistics above had shown the importance of orthopaedic implants in the future and therefore continuous evolution of knee and hip replacements are vital to fulfil the quality of life of the ageing people. In accordance to that, the quality of the implants needs to be raised through increasing the longevity of it in the human body, hence decreasing the revision surgery accordingly.

2.2 Currently Used Metallic Biomaterials and Their Limitations

Metallic materials are most practical in the reconstruction and replacement of hard tissues as at today due to their load bearing properties, durability and availability. The main metallic biomaterials that are most extensively utilised in the current market are stainless steel, cobalt-chromium and Ti-6Al-4V alloys.

2.2.1 Stainless Steel 316L

Stainless steel was first used because of its greater strength than steel and of higher corrosion resistance. The major component in the stainless steel that contributes to its high corrosion resistance is chromium. The inclusion of molybdenum on the other hand prevents pitting corrosion in salt water and this alloy was later regarded as 316. 316L became known with the reduction in carbon content from 0.08 w/o to 0.03 w/o maximum to further enhance the corrosion resistance in a chloride solution. The stainless steels that are most widely used for implants are the austenitic stainless steels, type 316 and 316L which is applicable to being hardened via cold working but not heat treatment. Both of these types are of better corrosion resistance than any other stainless steel. Type 316L is more recommendable for fabrication of implant compared to 316 as suggested by the ASTM (American Society for Testing and Materials)⁶.

The specifications for 316L stainless steels are shown in Table 1. Despite the reduction of carbon content to 0.03 w/o in 316L which aims to reduce the vivo corrosion in medical implant, it may still corrode under extreme circumstances in the human body in a highly stressed and oxygen-depleted region. However, they are applicable to be used as bone screws, bone plates, intramedullary nails and external fixators as temporary implant devices⁶. Table 1 indicates that nickel is also a major element in stainless steel. Nickel and chromium are reported to cause allergic contact dermatitis (ACD)⁷, thus it should be avoided to use in patients who are allergic or hypersensitive to these elements, especially nickel since there is a notable increase in the incidence of nickel sensitization⁸.

Table 1: Chemical compositions of SS 316L surgical implants (ASTM, 2000)⁹

Element	Composition (w/o)
Carbon	0.030 max
Manganese	2.00 max
Phosphorus	0.025 max
Sulfur	0.010 max
Silicon	0.75 max
Chromium	17.00–19.00
Nickel	13.00–15.00
Molybdenum	2.25–3.00
Nitrogen	0.10 max
Copper	0.50 max
Fe	Balance

Stainless steels (F138 and F139 of ASTM).

The mechanical properties of 316L stainless steel are listed in Table 2. It has sufficient strength to withstand the weight of the extra load carried on a human body, and also high modulus of elasticity to resist the external force.

Table 2: Mechanical properties of 316L Stainless Steel¹⁰

Mechanical Properties	Metric
Modulus of Elasticity	193 GPa
Tensile strength, Ultimate	515 MPa
Tensile strength, Yield	205 MPa
Elongation at break	60 %
Hardness, Vickers	155 HV
Density	8.0 g/cm ³

2.2.2 Cobalt-Chromium Alloys

Two most common types of cobalt chromium alloys are cast CoCrMo (Cobalt chromium molybdenum) alloys and wrought CoCrNiMo (Cobalt chromium nickel molybdenum) alloys. There are basically four major elements that form the solid solution of this alloy, namely cobalt, chromium, molybdenum and nickel (Table 3). While molybdenum is used to refine the grains in order to strengthen the alloy during casting or forging, nickel is included to improve the corrosion resistance of the alloy¹¹. Despite their benefit, it is pronounced that nickel, chromium and cobalt should be avoided in use with patients who are allergic to them.

One method that applies to increase the strength of this alloy is hot-forging. Even though cold-working is extensively used for the same effect, it is not recommended for cobalt chromium alloy especially in large devices fabrication for example hip joint stems because of the complicated process. CoCrMo is normally cast into dentistry devices and artificial joints whereas wrought CoCrNiMo is hot forged into prostheses stems for knee and hip which are of heavily load bearing joints¹⁰.

Both CoCrMo and CoCrNiCo have poor frictional properties thus are not beneficiary to be fabricated as the bearing surfaces of any joint prosthesis which require high wear resistance. However, they are much appreciated for their long service life as the stem of hip prosthesis to secure the complicated procedure of replacement and surgery revision due to a shorter lifespan¹⁰.

Table 3: Chemical composition of cobalt chromium alloy (ASTM, 2000)¹⁰

Element	Co28Cr6Mo (F75) Castable		Co20Cr15W10Ni (F90) Wrought		Co28Cr6Mo (F1537) Wrought		Co35Ni20Cr10Mo (F562)	
	Min.	Max.	Min.	Max.	Min.	Max.	Min.	Max.
Cr	27.0	30.00	19.00	21.00	26.0	30.0	19.0	21.0
Mo	5.0	7.00	–	–	5.0	7.0	9.0	10.5
Ni	–	2.5	9.00	11.00	–	1.0	33.0	37.0
Fe	–	0.75	–	3.00	–	0.75	9.0	10.5
C	–	0.35	0.05	0.15	–	0.35	–	0.025
Si	–	1.00	–	1.00	–	1.0	–	0.15
Mn	–	1.00	–	2.00	–	1.0	–	0.15
W	–	0.20	14.00	16.00	–	–	–	–
P	–	0.020	–	0.040	–	–	–	0.015
S	–	0.010	–	0.030	–	–	–	0.010
N	–	0.25	–	–	–	0.25	–	–
Al	–	0.30	–	–	–	–	–	–
Bo	–	0.01	–	–	–	–	–	0.015
Ti	–	–	–	–	–	–	–	1.0
Co	–	–	–	–	–	–	–	–
				Balance				

The mechanical properties of the commonly used cobalt chromium-based alloys are listed in Table 4. It has higher strength and modulus elasticity compared to stainless steel 316L.

Table 4: Mechanical properties of CoCr alloys¹²

Condition	Yield strength (MPa)	Tensile strength (MPa)	Elastic modulus (GPa)	Elongation (%)
Co28Cr6Mo (F75) cast	450	655	248	8
Co28Cr6Mo (F1537) annealed	517	897	220	20
Co20Cr15W10Ni (F90) wrought	379	896	242	-
Co35Ni20Cr10Mo (F562) annealed	241-448	793-1000	228	50

2.2.3 Ti-6Al-4V

Titanium alloys cover a wider range of implants devices as compared to stainless steel 316L and cobalt chromium alloy owing to their highly desirable biocompatibility, corrosion resistance, specific strength and comparatively lower Young's modulus¹³. One titanium alloy which is extensively used is Ti-6Al-4V. The chemical composition is given in Table 5.

Table 5: Chemical composition of Ti-6Al-4V¹⁴

Element	Wrought, forging (F136, F620)	Casting (F1108)	Coating (F1580)
N	0.05	0.05	0.05
C	0.08	0.10	0.08
H	0.012	0.015	0.015
Fe	0.25	0.30	0.30
O	0.13	0.20	0.20
Cu	-	-	0.10
Sn	-	-	0.10
Al	5.5–6.50	5.5–6.75	5.50–6.75
V	3.5–4.5	3.5–4.5	3.50–4.50
Ti		Balance	

Although of being widely used, Ti-6Al-4V is not well developed as a medical implant material because of its vanadium content which has been shown to be toxic according to Domingo J, 2002¹⁵. Furthermore, Boyce B et al, 1992 had confirmed that aluminium is also neurotoxic¹⁶.

The mechanical properties of Ti-6Al-4V is given in Table 6. The tensile strength of Ti-6Al-4V is equivalent to 316L stainless steel and cobalt chromium-based alloys. Nevertheless, it is preferable because of its lower modulus elasticity, which is almost half of those two materials. In respect to specific strength, Ti-6Al-4V is much preferable as it weights lighter but stronger. Titanium, however has some

drawbacks which include poor shear strength thus less suitable to be used as bone screws, plates, and similar applications. Besides, it galls or seizes on the sliding contact between itself and another metal⁷.

Table 6: Mechanical properties of Ti-6Al-4V¹⁵

Properties	Wrought (F136)	Casting (F1108)
Yield strength (MPa)	795	758
Tensile strength (MPa)	860	860
Elastic modulus (GPa)	110	110
Elongation (%)	10	8
Reduction area (%)	20	14

In comparison of stainless steel 316L, cobalt chromium alloys and Ti-6Al-4V, stainless steel exhibits a higher ductility and cyclic load whereas cobalt chromium alloys show the highest tensile strength, stiffness and wear resistance. Ti-6Al-4V on the other hand demonstrates properties nearest to the bone in terms of Young's modulus as it has lower stiffness than its counterparts¹⁸.

The main manufacturers of prostheses are shown in Table 7, which include Zimmer Biomet, Depuy and Smith & nephew. Most of the recent femoral stems are made of Ti-6Al-4V and cobalt chromium alloy.

Table 7: Current metallic alloy in used as biomaterials by various manufacturers

Metallic Alloy	Application	Manufacturer
Forged Ti-6Al-4V,	Femoral stem	Zimmer Biomet (Avenir)
Forged Ti-6Al-4V, porous plasma spray coating	Femoral stem	Zimmer Biomet (Echo)
Cobalt Chromium	Femoral Stem	Zimmer Biomet (CPT) Hip
Ti-6Al-4V,	Femoral Stem	Zimmer Biomet (Fitmore)
Porous titanium structure,	Femoral stem	Altimed
Ti alloy stem	Femoral stem	Depuy Total Hip System & Bone Preservation Stem
Cobalt-chromium & porous coating	Femoral stem	Smith & nephew Echelon
CpTi based	Femoral stem	Smith & nephew Polarstem
Cobalt-chromium	Femoral stem	Smith & nephew CPCS
Titanium Alloy	Femoral stem	Smith & nephew SL Plus

2.3 Requirements and Limitations of Biomaterials

The selection of biomaterial must address at least three criteria. The first being biocompatibility in which the material must be able to function and perform with an appropriate host response in a specific situation¹⁹ that is not harmful or toxic to the living tissues in the human body. Secondly, it should be strictly inert chemically to discourage passivation or corrosion that facilitates removal or revision surgery. Lastly, it depends on the intended medication application whether the implant should be resorbable over time or osseointegrate with the host bone, promoting bone ingrowth at the implant surface or securely linking the bone to the surface of the implant²⁰.

2.3.1 Mechanical Properties

The geometry of the implant for a specific application is one selection criterion of materials with regards to mechanical properties. It determines the stress distribution within the bone-implant interface as well as the surrounding bones. In addition to that, the geometry of articulating surfaces defines the range of motion of the prosthetic joint and the kinematic stability of the articulation²¹.

The dominant mechanical properties in determining the biomechanical compatibility of the implant are Young's modulus, tensile strength, yield strength and elongation. Another significant criterion is fatigue strength which determines the success of long service life of implant subjected to cyclic loading. The material to replace bone is required to have stiffness matches the bone, which is shown in Table 8. It is targeted to prevent inadequate strength or mismatch of stress (stress shielding) between the living bone and implant that lead to crack nucleation and fracture. The material aimed to replace bone is expected to have modulus ranges from 4 to 30 GPa within a variety of bone type and the angles or phases of measurement²².

Table 8: Mechanical properties of human bones²³

	Yield strength, MPa	Ultimate strength, MPa	Elastic Modulus, GPa	Elastic strain, %	Density, g/cm ³
Fibula	-	80-100	15.2-19.2	1.19-2.10	1.73-1.91
Humerus	-	149-151	15.6-16.1	1.90-2.20	1.72-1.77
Tibia	129	84-156.71	16.2-23.83	1.56-3.09	1.83-1.96
Femur	114.14	68-141	13.6-16.8	1.07-2.83	1.80-1.91

2.3.1.1 Stress Shielding

The most common problem of current implant materials that is related to mechanical factor is of high stiffness. In this scenario, the implant shields the adjacent bones from the stress transferred, thereby

preventing bone from functioning and thus causing bone resorption and consequently implant loosening. This phenomenon is called the stress shielding effect which leads to bone cells death²⁴. Cases of stress shielding effect are normally observed in medial side of proximal femur after hip replacement, or under tibial implant²⁵. Thus, selection of material with optimized coexistence of sufficient strength yet Young's modulus closest to bone is vital in promoting a good quality and durable implant.

To avoid stress shielding, more flexible components have been proposed²⁶. Current research has shown improvements especially in Young's modulus and strength/ductility balance of metallic biomaterials. However, a high flexible metal may create unsustainable interface stresses between bone and implants and eventually damage accumulation in cemented implants or failed ingrowth within cementless implants²⁷.

Young's modulus is most extensively researched because of its close connection to alleviate stress shielding that causes bone atrophy and poor bone remodelling²⁸. Therefore, many scientists and engineers have been since developing materials with comparative Young's modulus to bones and sufficient structural strength to be used in prostheses.

2.3.2 Biocompatibility

It is essential that the metallic biomaterials that are used in medical implants to be biocompatible, nontoxic and not causing any inflammatory or allergic responses in the body. An implant may cause alteration mechanically or chemically in its adjacent environment or systemically, such as materials degradation *in vivo* and the human body reaction towards the implant²⁹.

Three groups of responses from the human body towards biomaterials are biotolerant, bioactive and bioresorbable. The exposure of the implants to human tissues and fluids will result in reactions that will determine either the body system accept or reject the implant³⁰. There are four reactions that happen more frequently than any other cases. Firstly, the protein absorption, whereby protein immediately spread over the outer layer of the implant and controls the response of the host, including cells and tissues. Secondly is the degradation of material in whereby a metallic implant corrodes, a ceramic implant is resorbed or the occurrence of polymer hydrolysis. Thirdly, the evolution of local host response through initiation of inflammatory which is followed consequently by repair process until the reaction becomes stable. Lastly, the systemic effects that happen remotely at a distance from the implant via chemical and mass transport phenomena in which implants release small particles from wear or damage and induce interference that might be carcinogenic to our immunologic system³¹.

Table 9 shows the biological impact of different elements. From the data given, there are four elements which are considered safe to our body system as no sign of toxicity or allergenic has been traced. The four elements are titanium (Ti), niobium (Nb), zirconium (Zr), and tantalum (Ta).

Table 9: Biological impact of some common alloying elements for implantation³²

Periodic position	Element	Biocompatible	Carcinogenic	Genotoxic	Mutagenic	Cytotoxic	Allergenic	Prone to corrosion	Other*	
3d	Ti	Yes	No	No	No	Med	No	No	No	
	V	No	Yes	Yes	Yes	High	Disputed	No	No	
	Cr	No	Disputed	Yes	Yes	High	Yes	No	No	
	Mn	No	No	Yes	No	High	No	Yes	No	
	Fe	No	No	Yes	Disputed	Med	No	Yes	No	
	Co	No	Yes	Yes	Yes	High	Yes	Yes	Yes	
	Ni	No	Yes	Yes	Yes	High	Yes	Yes	Yes	
	Cu	No	No	Yes	Yes	High	Yes	Yes	Yes	
4d	Zr	Yes	No	No	No	Low	No	No	No	
	Nb	Yes	No	No	No	Low	No	No	No	
	Mo	No	Disputed	Yes	Yes	Low	Yes	Yes	Yes	
	Tc	- Radioactive -								
	Ru	Yes	No	No	No	Med	No	No	Yes	
	Rh	No	Yes	Yes	Yes	High	Unknown	No	No	
	Pd	No	Yes	No	Disputed	Med	Yes	No	No	
	Ag	No	No	No	No	High	Yes	No	Yes	
5d	Hf	Unknown	Unknown	Unknown	Unknown	Med	No	No	Unknown	
	Ta	Yes	No	No	No	Low	No	No	No	
	W	No	Yes	Yes	No	Med	No	Yes	No	
	Re	Unknown	Unknown	Unknown	Unknown	Unknown	No	No	Unknown	
	Os	No	Unknown	Yes	Yes	High	No	Yes	No	
	Ir	No	No	No	Yes	High	No	No	Yes	
	Pt	No	Yes	Yes	Yes	High	Yes	No	No	
	Au	Yes	No	No	No	High	No	No	No	
Other	Al	No	No	Yes	No	Low	No	No	Yes	
	Zn	No	No	No	No	High	No	No	Yes	
	Sn	Yes	No	No	No	Low	No	No	Yes	

Red - serious concern; Yellow - moderate concern; Green - minimal/no concern, Other* - issues beyond those already listed.

2.3.3 Corrosion Resistance

The *in vivo* condition provides an aggressive and extreme platform that accelerates the corrosion rate for implant metals and alloys. Agents present *in vivo* such as body fluid, proteins, enzymes, and various cells may release toxicity and allergy from the interaction with the artificial implants. The residual released has great potential in resulting implant failure and may be life threatening. Non-compatible metal ions from the implant of low corrosion resistance tend to release into the body and initiate allergic and toxic reactions³³. Nevertheless, the amount of ion released alters and relies on different factors such as the strength of the metal-oxide bond, structure, role of alloying element, composition, nature and thickness of the protective oxide films. A passive layer is formed on the implant surface that acts as physiological protection against the body agents thus increases the corrosion resistance and reducing the inflammation caused by implants³⁴. Metallic biomaterials corrode in various ways, which are galvanic corrosion, pitting, crevice, intergranular, stress-corrosion cracking, corrosion fatigue, and

tribocorrosion or fretting corrosion³⁵. Several elements which are prone or susceptible to corrosion are illustrated in Table 9.

2.4 New Generation of Titanium alloys for Implants

As previously discussed in Section 1.2, metallic implants are vulnerable and prone to common problems such as high Young's modulus compared to bones', poor biocompatibility and low corrosion resistance. And since the demand of implants has significantly increased over the last decade, engineers and researchers across the globe have started addressing these issues earnestly through either modification of the existing alloys or exploring on new alloys which are resilient to the requirements.

2.4.1 Advantages of Ti-alloys Compares to Other Metallic Alloys

Titanium alloy has the highest biocompatibility among stainless steel 316L and cobalt chromium alloys. It also exhibits a high specific strength and superior corrosion resistance. Owing to these advantages of titanium alloy, Ti-6Al-4V is ranked the most widely used metal in medical implants. Until recently, stress shielding has been a concern in causing failure in metallic implants due to loosening of the implant or fracture of the bone resulted from bone resorption. This happens because of a higher Young's modulus of the implant compared to that of bone.

Among all applicable materials, titanium alloys have the lowest Young's modulus³⁶. The elastic modulus of titanium alloy, Ti-6Al-4V (110 GPa) is half of the stainless steel and Co-Cr based alloys where their stiffness is 190 and 220 GPa respectively, however they are still considered too high compared with bones. Researchers and engineers are still experimenting on the new generation of titanium alloys with intention to lower the Young's modulus as much as possible to approach that of the bone.

2.4.2 Early Development of New Generation Ti-alloys

One thing that have shown promising result is that β -type Ti alloys has the lowest modulus compared with other types such as α , α' , $(\alpha+\beta)$, and ω -type. This is achievable due to the crystal structure of the phases, which β -type Ti alloys have body-centred (BCC) cubic structure and α -phase owns the hexagonal closed-packed (HCP) component. BCC structure has the lowest lattices density, therefore effort in developing low modulus β -type Ti alloys (Table 10) for biomedical devices was further explored and progressed³⁷. The first generation of β -type Ti alloys developed consist of a wide range of elements, such as molybdenum (Mo), iron (Fe) and silicon (Si). Later on, cheaper elements are proposed as alloying elements such as manganese (Mn), magnesium (Mg) and tin (Sn).

Even though these combinations offer a low Young's modulus, as shown in Table 10, they are found to be either toxic or easily biodegradable which is harmful and unsustainable³⁵. Due to significant impact

of the toxic elements, the preliminary purpose of the thesis will be based on non-toxic elements which are Ti, Nb, Zr and Ta, which will be further discussed in the next section.

Table 10: Some of the β -type Ti alloy developed and the Young's modulus³⁸

Alloy Designation (wt%)	Elastic Modulus (GPa)
Ti-12Mo-6Zr-2Fe	74-85
Ti-15Mo	78
Ti-15Mo-5Zr-3Al	80
Ti-15Mo-2.8Nb-0.2Si	83
Ti-12Mo-3Nb	105
Ti-12Mo-5Ta	74
Ti-12Mo-5Zr	64
Ti-25Nb-11Sn	53
Ti-25Nb-2Mo-4Sn	65
Ti-16Nb-10Hf	81
Ti-24Nb-4Zr-7.9Sn	46
Ti-24Nb-4Zr-7.9Sn	55
Ti-24Nb-4Zr-7.9Sn	53
Ti-35Nb-7Zr-5Ta-0.4O	66
Ti-22.3Nb-4.6Zr-1.6Ta-6Fe	52
Ti-29Nb-13Ta-4Mo	50-80
Ti-29Nb-13Ta-6Sn	65-70
Ti-29Nb-13Ta-4.6Sn	55-78
Ti-29Nb-13Ta-2Sn	45-48
Ti-35Nb-4Sn	42-55
Ti-30Zr-3Cr-3Mo	66-78
Ti-30Zr-(5,6,7) Mo	59-75
Ti-80Mg	59.2-67.1 ³⁹

2.4.3 β -type Ti-alloys with Nontoxic Elements

A new evolution of low modulus β -type Ti alloys composed of rare metals Nb, Zr and Ta have been extensively reviewed and studied. This approach has a promising potential in resolving the problem of getting the best biomaterial for an implant. From Table 9, these four elements (Ti, Nb, Zr, and Ta) are the sole material accountable of good biocompatibility and high corrosion resistance. Since then, modification on β -type Ti alloys focusing on these four elements in various concentration have been studied and developed to obtain Young's Modulus closest to the bones, which is approximately 5-30 GPa. Table 11 shows the research results based on a vast range of combination of Ti alloys with the

different composition of Nb, Zr and Ta and their properties. They can be grouped into binary, ternary and quaternary combination. The Young's modulus can span from 140 GPa to as low as 14 GPa.

Table 11: Ti-Nb-Zr-Ta alloy in binary, ternary and quaternary combination and their Young's modulus^{12,22}

Alloy elements	Young's modulus (GPa)	Alloy elements	Young's modulus (GPa)
Binary		Binary	
Ti ₂₀ Nb	74	Ti ₂₈ Nb _{35.4} Zr	64±4.5
Ti _{25.6} Nb	62	Ti ₃₀ Nb ₃₂ Zr	65±4.2
Ti ₃₅ Nb	67.8	Ti ₃₄ Nb ₂₅ Zr	62±3.6
Ti ₃₆ Nb	60	Ti ₃₅ Nb ₅ Zr	65/59.8
Ti ₄₀ Nb	62	Ti ₃₅ Nb ₁₀ Zr	50-90
Ti ₄₄ Nb	70	Ti ₃₅ Nb ₁₅ Zr	62.9
Ti ₁₀ Ta	99	Ti _{41.1} Nb _{7.1} Zr	65±1
Ti ₂₀ Ta	82	Ti ₄₅ Zr ₁₀ Ta	109±2
Ti ₂₅ Ta	64±3.7	Ti ₄₀ Zr ₁₄ Ta	120±20
Ti ₃₀ Ta	69	Ti ₃₅ Zr ₁₈ Ta	130±10
Ti ₄₀ Ta	81	Ti ₃₀ Zr ₂₂ Ta	112±5
Ti ₅₀ Ta	77-93	Quaternary	
Ti ₆₀ Ta	82	Ti _{22.5} Nb ₂ Ta _{0.7} Zr	50-70
Ti ₇₀ Ta	67	Ti _{23.72} Nb _{4.83} Zr _{1.74} Ta	42
Ti ₈₀ Ta	104	Ti ₂₉ Nb ₁₃ Ta _{7.1} Zr	55
Ti ₁₀ Zr	100	Ti ₂₉ Nb ₆ Ta ₅ Zr	43
Ti ₂₀ Zr	125	Ti ₂₉ Nb ₁₁ Ta ₅ Zr	60
Ti ₃₀ Zr	124	Ti ₂₉ Nb ₁₃ Ta _{4.6} Zr	55-97
Ti ₄₀ Zr	123	Ti ₃₅ Nb ₂ Ta ₃ Zr	40-48
Ternary		Ti ₃₅ Nb _{5.7} Ta _{7.2} Zr	57
Ti ₁₇ Nb ₆ Ta	71	Ti ₃₅ Nb _{2.5} Ta _{2.5} Zr	60-80
Ti _{19.7} Nb _{5.8} Ta	10-60	Ti ₃₅ Nb ₅ Ta ₅ Zr	65-80
Ti ₂₅ Nb ₂₅ Ta	55	Ti ₃₅ Nb _{7.5} Ta _{2.5} Zr	58-78
Ti ₃₅ Nb ₁₀ Ta	55-75	Ti _{23.7} Nb _{4.83} Zr _{1.74} Ta	35-42
Ti ₁₃ Nb ₁₃ Zr	44-84	Ti ₃₀ Nb ₁₀ Ta ₅ Zr	66.9
Ti _{18.20} Nb _{5.6} Zr	45-55	Ti ₃₅ Nb ₇ Zr ₅ Ta	55
Ti ₁₉ Nb ₁₄ Zr	14	(TiOsteum)	
Ti _{24.8} Nb _{40.7} Zr	63±4.2	Ti _{39.3} Nb _{13.3} Zr _{10.7} Ta	71
Ti ₂₇ Nb ₈ Zr	70-120	Ti ₁₀ Zr ₅ Ta ₅ Nb	46-58

Three graphs were plotted, using the data available in open literature, to highlight the changes of Young's modulus with respect to Ti%, Nb% and Zr% in an increasing order. As it is evident from the

histogram distribution graphs in Figure 3, Figure 4 and Figure 5, it is difficult to establish a trend on the effect of the alloying elements on the modulus of Ti-Nb-Zr alloys.

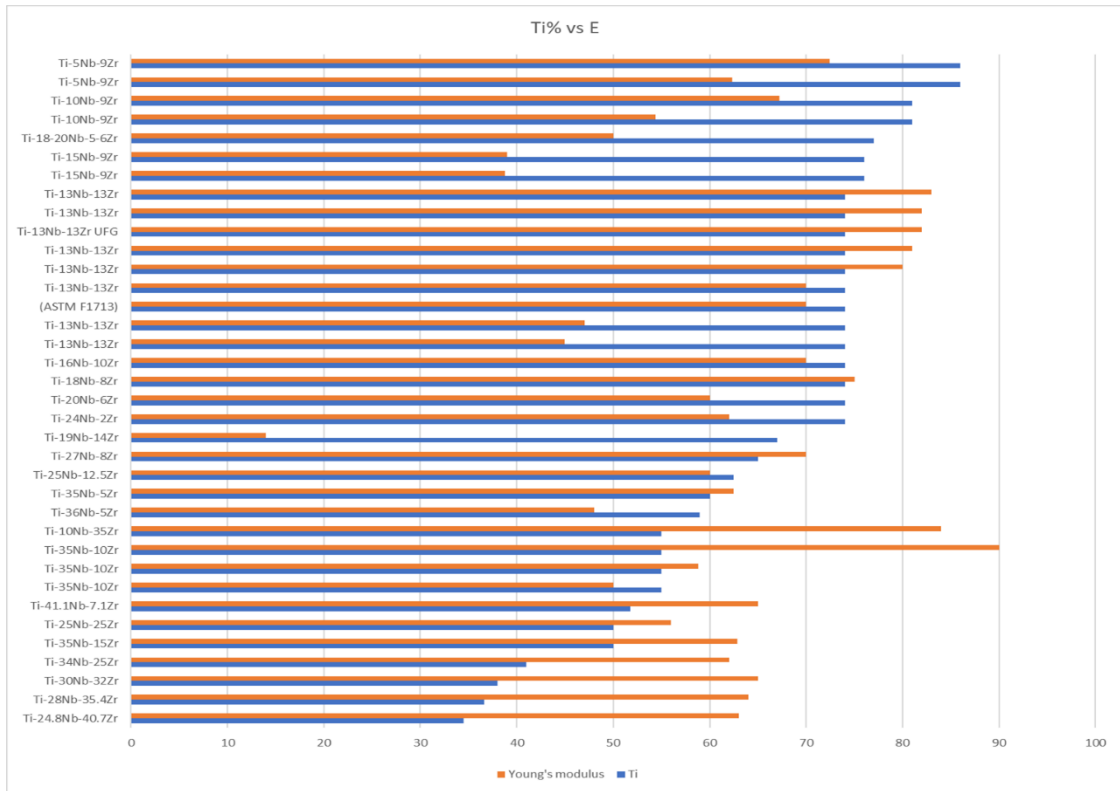


Figure 3: Plot of Ti-Nb-Zr alloy vs Young's modulus with respect to Ti% in an increasing order

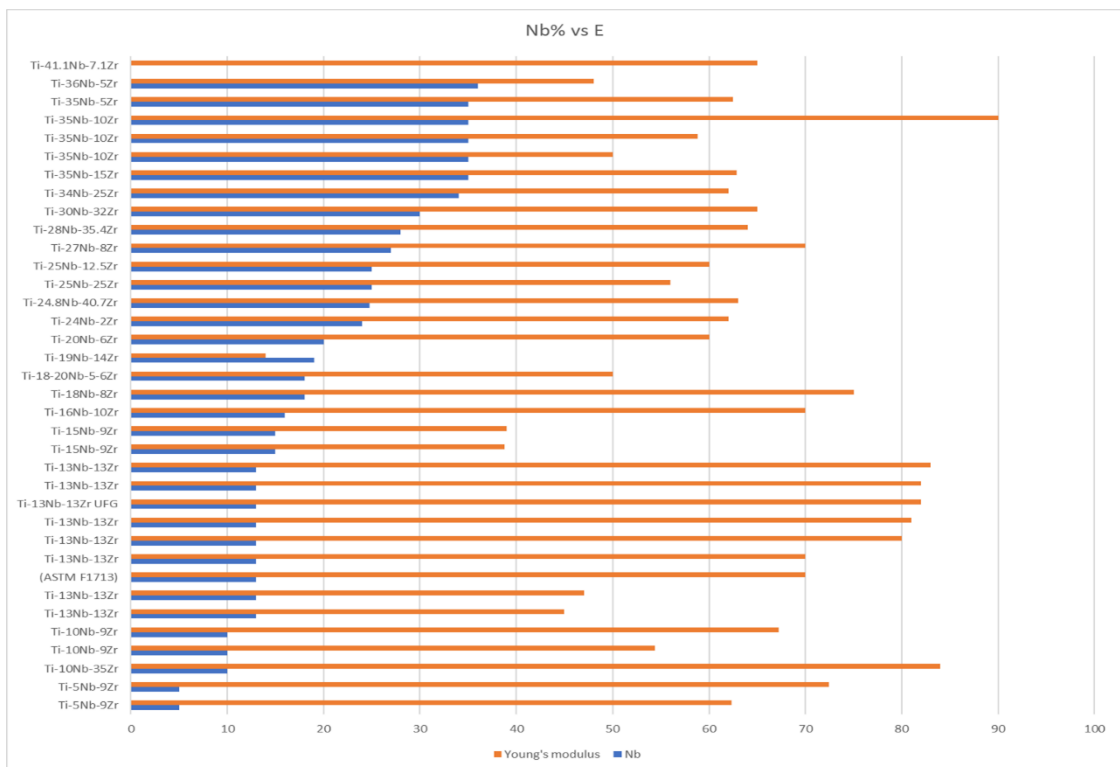


Figure 4: Plot of Ti-Nb-Zr alloy vs Young's modulus with respect to Nb% in an increasing order

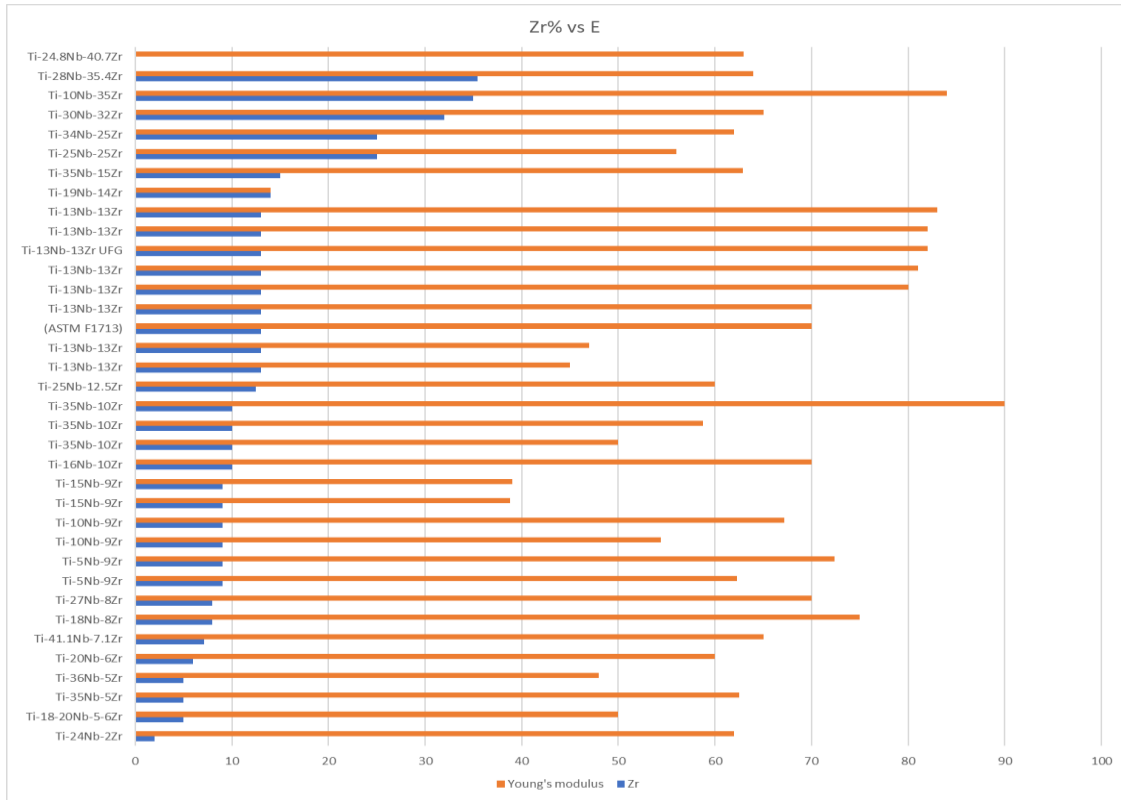


Figure 5: Plot of Ti-Nb-Zr alloy vs Young's modulus with respect to Zr% in an increasing order

2.4.4 Heat Treatment and Strengthening Effects

Heat treatment and strengthening work are two potential methods that could be utilised to enhance the mechanical properties of the β -type Ti alloy. The strengthening works include cold working, severe cold swaging or plastic deformation. The disadvantages of cold working include strain hardening, use of expensive equipment, undesirable residual stresses and less ductility⁴⁰ because tensile strength is increased during the process. However, the ductility and the Young's modulus are retained⁴¹. Along with the strengthening effect, cold working also provides some advantages which are; good control of dimensional deviations, better reproducibility, as well as high levels of straightness and machinability⁴².

While cold working increases tensile and yield strength, hot working of Ti-alloy reduces the strength thus increases the ductility. The elevated temperature involved is less cost-effective as it slows down the production rate thus increases the time. However, the diffusion from the heat enhances the removal or reduction of chemical in-homogeneities. Other undesired consequences from hot working are poor dimension, tolerances from uneven cooling, thermal shock and possible surface defect from low thermal conductivity⁴³. Hydrogen absorption might occur induces poorer mechanical properties that required alleviation through preheat⁴⁴.

Heat treatment is one common method used to improve the mechanical strength of titanium alloys. Solution treatment is utilised to enhance the uniform distribution and microstructure across the element.

Aging process after the solution treatment is aimed to prevent the formation of brittle ω -phase⁴⁵. However, a very little amount of ω -phase is considered effective in increasing the fatigue strength of the alloy without having any impact on the Young's modulus. Secondary to that, some literatures have shown effective signs of fine ω precipitates in increasing Ti-alloy's super-elastic property⁴⁶. Nevertheless, the amount of ω phase precipitation should be strictly controlled as there had been reported occurrence of embrittlement due to intolerable amount⁴⁷. ω -phase belongs to hexagonal structure and is metastable. It can be produced by short-aging time at a relatively low temperature or intermediate temperature and the amount decreased with increasing β -stabilizer⁴⁸. Besides, quenching of β -phase from high temperature also produces a small amount of ω -phase⁴⁹. In addition to ω phase, the formation of other phases influences the mechanical properties of Ti-alloys. According to Nakai M 2012, by optimising α phase precipitation through aging treatment and cold rolling, it is possible to increase the fatigue strength while maintaining relatively low Young's modulus⁵⁰.

For powder metallurgy fabrication route of Ti-alloys, a higher sintering temperature optimises the solubility of the alloying element such as Nb and Zr in the Ti matrix besides effectively suppresses the β - α phase change which directly increases the amount of β -phase. This result thus suggests that a high sintering temperature increase the amount of β phase in alloys⁵¹.

2.4.5 Microstructure Characterization of Ti-Nb-Zr alloys

The microstructure characterization of Ti-Nb-Zr alloys were found to contain five individual phases in the literatures published, specifically β -phase, α -phase, α' -phase (Figure 7), α'' -phase (Figure 8) and ω -phase (Figure 9) or a combination of two (Figure 6) or more of these phases. The crystal structure of β -phase is BCC. Whereas α -phase, α' -phase, and ω -phase are of HCP crystal structure. The α'' -phase belongs to orthorhombic crystal structure. Among these phases, β -phase has the dominant volume matrix in Ti-Nb-Zr alloy compared to other phases and is mostly desired and has been proven to offer the lowest Young's modulus among other phases. Additionally, several types of micro constituents and microstructures are also observed, namely Widmanstätten and basketweave patterns, acicular martensitic, lamellar (Figure 10), primary and secondary α (Figure 11). The transformation of microstructures and phase of these alloys are highly dependent on the cooling rate, prior heat treatment and work hardening process¹⁰⁶.

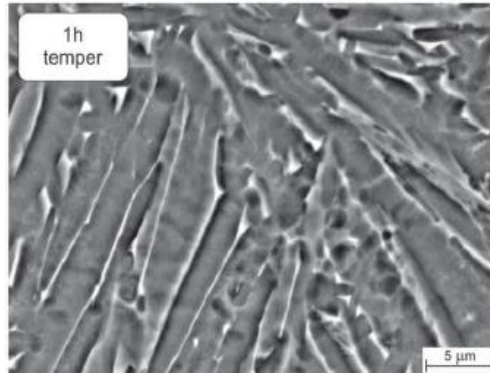


Figure 6: SEM ($\alpha+\beta$)-phase: Decomposition of undeformed α laths with precipitation of β phase between them⁵².

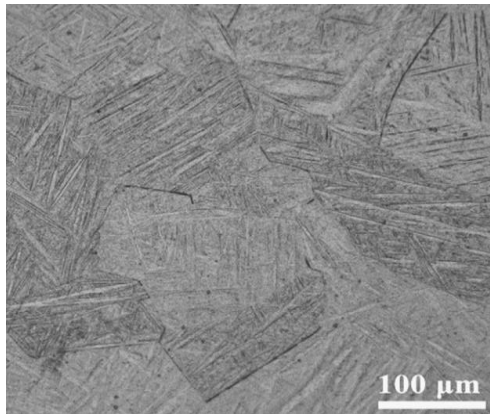


Figure 7: Optical micrograph showing α' -phase after homogenized at (950 °C) for 5h, followed by water quenched and then solution treated at 900°C for 1h and water quenched⁹⁰.

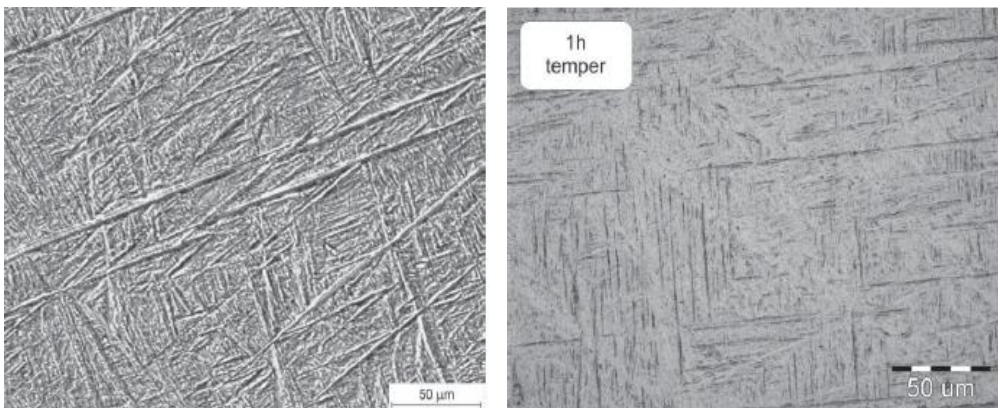


Figure 8: Optical micrographs showing Widmanstätten α'' -phase (a) after water quenched from 1050°C with martensitic transformation and the formation of laths, (b) tempered at 750°C for 1hr after water quenched from 1050°C⁵².

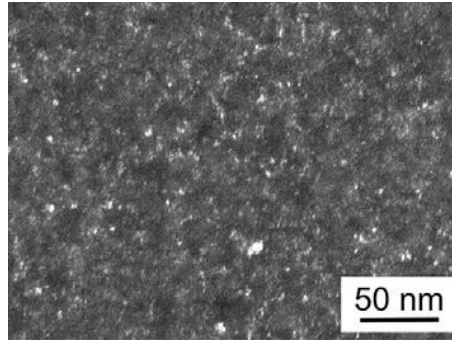


Figure 9: TEM dark-field images showing diffusion of ω phase⁵³

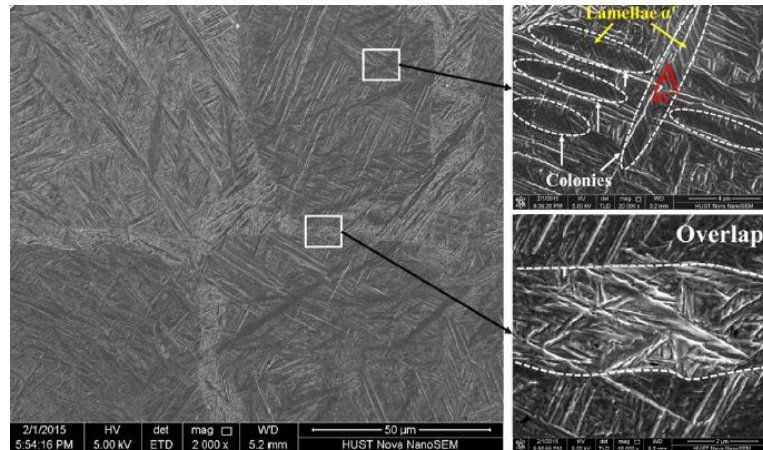


Figure 10: SEM images of acicular and lamellar α' phases⁵⁴

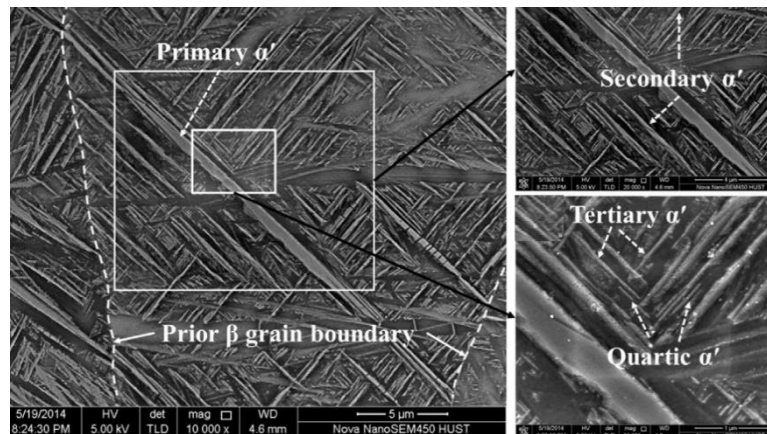


Figure 11: SEM images of primary, secondary, tertiary and quartic α' ; prior β grain boundary⁵⁵

2.4.6 Different Methods Applied to Develop Low Young's Modulus Ti-alloys

Various theoretical approaches have been developed to further reduce the intrinsic Young's modulus of β -Ti alloys through alloying elements selection and composition design. While Kuroda et al. 1998, have first implied a method in increasing two alloying parameters which are the average covalent bond strength (B_0) and average d orbital energy level (M_d) to acquire low elastic modulus of β -phase Ti-

alloys, it is however could not be further clarified due to the complicated quantitative relationships between Young's modulus, B_0 , and M_d . After 13 years, on 2011, Friak et al proposed a method namely *ab initio* prediction to calculate the elastic constant of various elastic properties. In Wang et al, 2016 report, it is concluded that single crystal along the $\langle 100 \rangle$ direction has a lower Young's Modulus than the polycrystalline which is restricted to 30–40 GPa. This is derived from a strong elastic anisotropy for Ti-rich compositions. Nevertheless, only few studies concerning single crystalline materials for biomedical appliances are reported due to difficult processing and preparation as mentioned by Takesue et al., 2009 and Tane et al., 2010. In addition to this, another estimation through calculations by first principle (FP) was proposed by Ikehata et al., 2004 and Ma et al., 2008. All of the above problems and solutions have outlined the application of CALPHAD (Calculation of Phase Diagram), a method used to describe single-crystal elastic constants based on the available experimental data and first-principle calculations⁵⁶.

2.5 Fabrication Methods for Titanium Alloys

There are two most commonly used methods in the fabrication of Ti alloys, which are ball milling or powder metallurgy and arc melting.

2.5.1 Ball Milling/Powder Metallurgy

Powder metallurgy is a good method in fabricating titanium alloys compared to the conventional way. It utilises either blended elemental (BE) powders or pre-alloyed (PA) powders to produce the desired composition. With blended elemental, the powder is cold pressed via gas or fluid into desired 'green shape' isostatically through mechanical pressing. This process guarantees a product of 95-99% density after being vacuum sintered. Besides, its simplicity yields some significant advantages such as cheap and versatile, with lower sintering temperatures than the melting points of each constituent element⁵⁷. Another option for PM is using pre-alloyed powders which the desired elements composition is being set. Compared with BE, this method requires a more sophisticated equipment thus it is abstained from cold or hot pressing.

Both BE and PA powder metallurgy own their advantages and drawbacks. The benefits of BE are that it demonstrates competent tensile strengths, fracture toughness while inhibited fatigue crack propagation although there is a slight reduction in fatigue strength. PA method on the other hand gives a finishing product that yields near full density with mechanical properties, including fatigue strength that exceed an equivalent wrought sample⁵⁸.

2.5.2 Arc Melting

Another common method for the fabrication of Ti-Nb-Zr-Ta is arc melting. It can be produced with high-purity alloy elements in a desired proportion. The melting process is carried out in an arc furnace under argon atmosphere furnished with water-cooled copper hearth. Due to a considerably difference of melting point and density between these four elements (Table 12), especially tantalum, the designed alloy is required to be melted multiple times and also at an extended time to ensure an existence of a homogeneous solid solution phase. At the same time, ingots may be flipped between the melting processes to further enhance the chemical homogeneities. The heating temperature is subjected to the designed alloy and whereby it must be above the β -transus temperature from the phase diagram⁵⁹.

2.6 β -type Ti-Nb-Zr Alloys

An array of combination between the elements of Ti-Nb-Zr-Ta has been engineered and studied in order to obtain the optimised composition that yields the least Young's modulus yet sufficient tensile strength for implant devices. This research project will be based on the same approach. However, tantalum is found to have a very high melting point which is almost twice that of titanium. It possesses a density of 16.4g/cm³, which is almost fourfold of titanium, as shown in the Table 12. Furthermore, pricing at USD139 per kg, it is substantially expensive compared to the other elements, which as a result makes it less favourable. Having considered these drawbacks, Ta was excluded in this project and the research outline will only focus on Ti, Nb and Zr. Although the study of this ternary combination is not new at this stage, and an extensive combination of various composition has been meticulously researched, yet achievement to obtain the Ti-Nb-Zr alloy of Young's modulus and strength nearest to the human bone is still to be resolved.

Table 12: Ti, Nb, Zr, Ta and their properties, T_m and price^{60,61}

Metal	Melting point (°C)	Young's Modulus GPa	Yield strength MPa	Density g/cm ³	Price (USD/kg) 2017
Titanium	1668	116	140	4.51	4.80
Niobium	2468	103	207	8.57	42.28
Zirconium	1852	94.5	230	6.51	100-150
Tantalum	3017	186	230	16.4	151.80

Listed under Table 13 are articles correspondence to studies and experiments of Ti-Nb-Zr as biomaterial with the purpose to obtain the lowest Young's modulus. The majority literatures established agreed to a better solution to acquire the best constitution of Ti-Nb-Zr alloy (which is low Young's modulus and high tensile) through tangible experiments in a scientific way. Others suggest using first principles theory known as parameter-free density functional theory calculations to get the composition which

gives the optimise Young's modulus and strength. A finer and homogeneous β -phase Ti alloy has been confirmed producing the lowest Young's modulus among other or combination of any other phases. Zirconium could form a complete solid solution in titanium alloy while niobium is a β -phase stabilising element.

The prominent outline of most literatures contains fabrication of this alloy, mechanical testings (tensile or compression test), microstructure and phases observation, cytotoxicity testing, monitoring of bone resorption and corrosion testing. Fabrication through arc melting is rather popular among the scholars because of its straightforward method and also the availability. More recently, porous titanium-based alloys were found increasingly capturing the interests of many researchers and engineers by the virtue of its porosity which could significantly reduce the Young's modulus. Although this alloy has many beneficiaries and yet to explored prospects, it also faces multiple unknown challenges in regard to fabrication, obstacles for expanded applications, and future opportunities.

Many studies have been done to modify titanium alloy with Young's modulus closest to the bone, ranging from 0.2-30 GPa, and results have proven satisfactory, nevertheless, this alloy has not been applied as at today as according to M Niinomi, 2012⁶², a well-known researcher in this field, because there are still rooms for improvement.

2.6.1 The Alloying Effects of Nb and Zr in Ti-alloys

One of the greatest advantages for Nb and Zr is that both are of nontoxic elements and corrosion resistant. In addition to that, Nb and Zr have unique roles and characteristics as alloying element. An addition of Zr actually helped stabilize the body-centered cubic β phase. There is an indication that increasing Zr content improve the strength of the alloy. Part of the reason could be attributed to the strengthening mechanism via substitution of Zr atom which anchors dislocation. By increasing Zr content, the amount of α phase is decreased. The improvement of mechanical strength can also be attributed to the refined grain size upon peak-aging treatment. The increasing Zr content helps to reduce the peak-aging time but is irrelevant in influencing the elastic modulus and elongation of Ti-alloy⁶³. Zr is regarded as a superior ternary element because of its biocompatibility and ability to reduce the unwanted phases such as ω phase which is known to increase the Young's modulus⁶⁴.

Since Nb is a β -stabilizer, the larger the Nb concentration, the higher are the percentage of β phase. As the Nb concentration increases, few scenarios are observed which include the slow disappearance of the α -phase mixture and a more homogeneous microstructure within niobium in the titanium matrix⁶⁵. K Rajamallu et al 2017 reported the Young's modulus increases with Nb content and above 25 at% of Nb, Young's modulus varies within the range of 60–80 GPa. This phenomenon happens subsequent to the increase in density due to the addition of Nb element which is heavier than pure Ti element⁶⁶.

In β -phase Ti-Nb system, the increase of Nb content is stabilised by addition of Zr. The β phase stability of ternary system is dependent on the amount of β stabilizing elements present, thus a higher concentration of Nb enhances the stability of the system. According also to K Rajamallu et al 2017, the Ti-Nb-Zr β -phase starts stabilizing from Ti-18.75at%Nb6.25at%Zr onwards and thus the best composition for Nb and Zr is either equivalent or more than 18.75at% and 6.25at% respectively.

2.6.2 Ternary Diagram for Ti-Nb-Zr Alloys

Several researchers have reported their findings on the isothermal processing of Ti-Nb-Zr ternary system⁶⁷. The temperature range specified is from 570 to 1100°C and the studies have included the liquidus surface⁶⁸ and solidus surface⁶⁹ over the entire region of composition. As according to Tokunaga et al 2007, the Ti-Nb-Zr ternary system is made up of solution phases only, namely the liquid phase, the BCC phase (Nb, β Ti, β Zr), and the HCP phase (α Ti, α Zr). Based on the Ti-Nb⁷⁰, Ti-Zr⁷¹ and Nb-Zr⁴⁹ binary system, a thermodynamic modelling of Ti-Nb-Zr was extrapolated⁶⁷ and the relationships between the phase and composition were well defined. Shown in Figure 12 is the calculated isothermal ternary diagram with the experimental data of the Ti-Nb-Zr ternary system at 570°C.

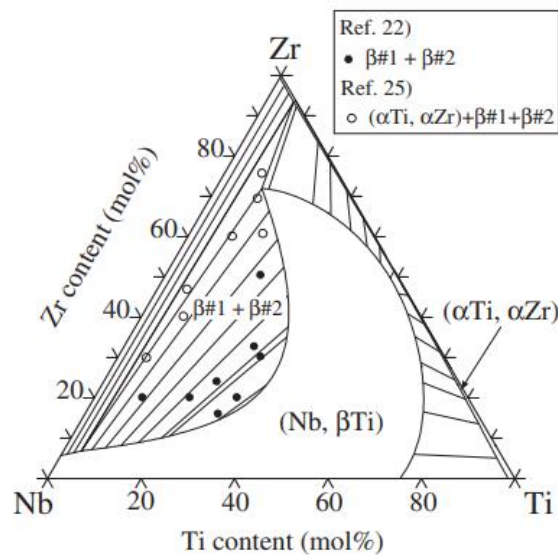


Figure 12: Calculated isothermal diagram of the Ti-Nb-Zr system at 570°C⁶⁷

Three different phases were distinguished in Figure 12, they are α -phase, β -phase, and α + β phase.

In Figure 13, the theoretical result of Ti-Nb-Zr system in liquidus surface is projected. The isothermal diagram elaborates melting point is increased proportionally with the niobium content as the melting point for niobium is the highest among the ternary system. The lowest and highest melting temperature to transform the entire range of Ti-Nb-Zr into liquid is 1577° and 2427° (Table 12).

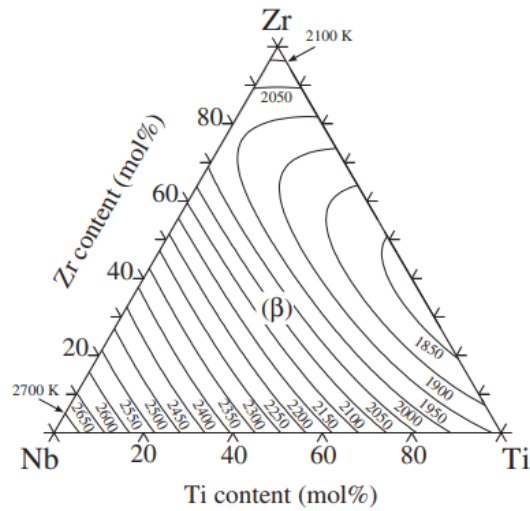


Figure 13: Calculated liquidus surface projection in the Ti-Nb-Zr system⁶⁷

Summary of Chapter 2: Literature Review

In this chapter, the demands of orthopaedic implants and their current problems are highlighted. The most concerning issue is the biomaterials used. They have been reported in causing stress shielding and releasing toxic elements to the human body. These drawbacks are resulted from the high Young's modulus and the toxicity of the alloying elements used. Thus, the new generation of Titanium alloys, especially Ti-Nb-Zr alloys, are developed to mitigate these problems as they have been found to offer low Young's modulus besides being non-toxic. Different fabrication methods, analysis on the microstructure and phase of Ti-Nb-Zr alloys from the published papers were also discussed. Ternary diagram and alloying effects which aims to obtain beta phase Ti-Nb-Zr alloys were also mentioned since beta phase has been giving a very promising Young's modulus closest to the bones.

Table 13: Table showing Ti-Nb-Zr alloys of different elements composition, their mechanical properties and arguments of findings from some articles.

Ti	Nb	Zr	Ta	E (GPa)	TS (MPa)	YS (MPa)	Strain%	Elong%	Arguments :	Ref
Ti-13Nb-13Zr (ASTM F1713)	74	13	13	79-84	973-1037	836-908	10-16	10-16	Proposing the evolution of porous Ti-based alloy as the results obtained β -type Ti-based alloys are too stiff compared with cancellous bones (0.2–2.0 GPa).	⁷²
	74	13	13	80	-	-	-	-	The α + β microstructure obtained through aging process is found superior than any other microstructure for biomedical devices as it displays a lower modulus, greater mechanical biocompatibility and moderate elongation to failure.	⁷³
	74	13	13	40-50	-	-	-	-	The authors encouraged more researches on metallic biomaterials to be investigated to help progress the development and practicability of low modulus Ti-based alloys. (Note: these alloys have not been put into use as at today)	⁷⁴
Ti-13Nb-13Zr Ultra-fine grain (UFG)	74	13	13	82	-	1021	1.4	1.4	UFG Ti-13Nb-13Zr alloy has great potential to replace Ti-6Al-4V for load bearing implants because of its excellent mechanical and biological compatibility. UFG alloy exhibits a greater combination of yield strength and Young's modulus compared to coarse-grained alloy.	⁷⁵
Ti-13Nb-13Zr	74	13	13	69-72	681-750	-	82-10.4	82-10.4	The elastic modulus and strength is enhanced remarkably with relative density. The density increases with Nb particles agglomeration as they retard the sintering mechanism and prevent homogenization. Thus, it must be avoided during the BE/PM process.	⁷⁶
Ti-10Nb-35Zr	55	10	35	-	-	-	-			
Ti-27Nb-8Zr	65	27	8	70-120	-	-	-			
Ti-16Nb-10Zr	74	16	10	70	520	485	0.69	0.69	Nb content should always be greater than Zr content as substitution of Nb by Zr will alter the phase constitution from single β phase to α '+' β phase thus increase the Young's modulus of the alloy. The authors claimed that the Zr/Nb:0.3 ratio is most superior as in Ti-20Nb-6Zr (compared to Ti-16Nb-10Zr, Ti-18Nb-8Zr and Ti-24Nb-2Zr) due to its super-elasticity and combined performance.	⁷⁷
Ti-19Nb-14Zr	67	19	14	14	-	-	-	-	β -type Ti alloys offer the lowest Young's modulus. However, there exist other methods such as precipitation, texture orientation, porosity structure and processing routes that could enhance the development of a desirable metallic biomaterial of low Young's modulus.	⁷⁸
Ti-18-20Nb-5-6Zr	74-77	18-20	5-6	45-55	-	-	-	-		
Ti-4Nb-15Zr	81	4	15	-	-	-	-	-	In terms of corrosion resistance, Ti-13Nb-13Zr has greater value than the Ti-5Nb-13Zr and Ti-20Nb-13Zr alloys.	⁷⁹
Ti-5Nb-13Zr	82	5	13	-	-	-	-	-		
Ti-20Nb-30Zr	50	20	30	-	-	-	-	-		
Ti-22Nb-6Zr	72	22	6	-	-	-	-	-		
Ti-20Nb-15Zr	65	20	15	-	-	-	-	-		
										⁸⁰

Ti	Nb	Zr	Ta	E (GPa)	TS (MPa)	YS (MPa)	Strain%	Elong%	Arguments :	Ref
Ti-35Nb-15Zr	50	35	15	1.2-10.8 (Porous)	73-1530 C (Porous)	-	-	-	The Nb, Zr concentrations and sintering temperature will affect the phase compositions and microstructures of Ti-Nb-Zr alloys.	
Ti-35Nb-5Zr	60	35	5	65/59.8 Ela	-	874	-	-	The addition of Zr in Ti-35Nb-xZr helps reducing Young's modulus while increasing the tensile strength and ductility of the alloy. Besides, it also stabilises the β -phase. Experiment showed osseointegration of this alloy.	81
Ti-35Nb-10Zr	55	35	10	58.8 Ela	-	-	-			
Ti-35Nb-15Zr	50	35	15	62.9 Ela	-	-	-			
Ti-20Nb-13Zr	-	-	-	-	-	-	-	-	Laser nitriding treatment tends to increase corrosion and wear resistance for Ti-Nb-Zr alloy.	82
Ti-5Nb-15Zr	80	5	15	-	-	-	-	-	Using nanotechnology surface treatment in galvanostatic anodization on Ti-15Zr-5Nb alloy surface. The layer outcome displays a nanotube-like porosity that can stimulate the formation of the bone, cell attachment and offers good corrosion resistance.	83
Ti-35Nb-3Zr	-	-	-	-	-	-	-	-	Ti-35Nb-xZr alloys showed an equiaxed β -phase microstructure and the β -phase stabilises with the increasing addition of Zr.	84
Ti-35Nb-5Zr	-	-	-	-	-	-	-	-		
Ti-35Nb-7Zr	-	-	-	-	-	-	-	-		
Ti-35Nb-10Zr	-	-	-	-	-	-	-	-		
Ti-25Nb-6.25Zr	-	-	-	50	-	-	-	-	Ti-25Nb-6.25Zr has the lowest average YM (50 GPa average value) among all the ternary BCC β Ti-25Nb-xZr systems.	85
Ti-25Nb-12.5Zr	-	-	-	60	-	-	-	-		
Ti-25Nb-18.75Zr	-	-	-	58	-	-	-	-		
Ti-25Nb-25Zr	-	-	-	56	-	-	-	-		
Ti-24Nb-2Zr	74	24	2	-	200-800	-	-	-	The ω -phase is a Ti-rich phase. The formation and growth of ω -phase particles will lead to the increase of β -phase particles in the β -phase matrix. The ω -phase also inhibits α'' -phase formation in the β matrix.	86
Ti-34Nb-25Zr	51	34	25	62±3.6	839±31.8	810±48.0	1.31	14.8±1.6	The Ti-Nb-Zr alloys displayed excellent ductility and cytocompatibility. They exhibited low Young's modulus, sufficient tensile strength, ability to sustain compression test with no cracking, or fracturing.	87
Ti-30Nb-32Zr	38	30	32	65±4.2	794±10.1	782±18.8	1.2	13±1.8		
Ti-28Nb-35.4Zr	36.6	28	35.4	64±4.5	755±28.3	729±26.3	1.14	11.3±1.5		
Ti-24.8Nb-40.7Zr	34.5	24.8	40.7	63±4.2	704±49.5	682±52.9	1.08	9.9±1.1		
Ti-35Nb-10Zr	55	35	10	50	900	850	-	13	The change of Zr content may induce dynamical recovery and recrystallization during hot forging of as-cast alloys. Needle like particles or ω -precipitates were observed after aging treatment.	88
	55	35	10	90	1300	1240	-	9		
Ti-41.1Nb-7.1Zr	51.8	41.1	7.1	65±1	490±27	490±27	-	16±3	A complete recrystallization occurs after heat treatment at 1000 °C/2 h followed by cold working. Tantalum tends to increase tensile strength and elongation yet decrease Young's modulus.	89
Ti-5Nb-9Zr	86	5	9	62.3-72.4					The author argued that α'' -type Ti alloys has higher potential than β -type Ti alloys in biomedical application as they offer lower cost, lighter weight and lower Young's modulus.	90
Ti-10Nb-9Zr	81	10	9	54.4-67.2						
Ti-15Nb-9Zr	76	15	9	38.8-39.0	850					

2.7 Research Objectives/Motivation

After reviewing the literature around the next generation Titanium alloys for medical implants, specifically Ti-Nb-Zr alloys, it gives an implication that these alloys are of great interest in the implants research as it generates massive benefit in the medical aspect. However, more studies and research are necessitated to realising these alloys into application. Currently, there is no mutual agreement between published papers in which elemental composition is most suitable and could yield the lowest Young's modulus. Although it has been reported in most papers that β -phase contributed to lowest Young's modulus, the best composition is yet to be investigated. Thus, this thesis aims to clarify these issues as well as to realise three objectives which are:

- To determine the proportion of Ti, Nb, and Zr elements in Ti-Nb-Zr alloys to find a good combination that yields a low Young's modulus that is closer to that of the bone (less than 50 GPa).
- To observe the phase diagrams of the alloys with component in multiple proportion, to observe the number and amount of the phases present at different designated temperatures and compositions.
- To understand the logic behind the microstructure and phases observed in Ti-Nb-Zr alloys.

The nature of the research for this thesis has been planned in order to meet the objectives and address the issues as stated. First of all, data were collected based on past experiments by various scholars, professionals which were verified through publications. Problems concerning the fabrication method, the implication behind lowering the elasticity and the alloy's proportion will be highlighted under the literature review section. One of the main goals of literature review is to observe the relationship between the alloys' composition and their Young's moduli. Three graphs with an increasing order of Ti wt%, Nb wt% and Zr wt% in the Ti-Nb-Zr alloys with regards to Young's modulus were plotted. The graphs serve as a purpose to monitor the effect of element composition on the Young's modulus value and also to address the relationship between the both factors.

Besides relying on the observation, analysis from the literature review, experiments will be carried out to gather evidence to support the hypothesis and assumptions made. The intended experiments and their setting parameters will be based on applicable standards, recommendations from the papers associated with the judgement made during the analysing process. Experiments will include microstructure observation with optical microscope and Scanning electron microscope (SEM), phase analysis with X-ray diffractometer (XRD) and Thermo-Calc, microhardness testing, nanoindentation and Young's modulus measurement.

The microstructure characterization is employed to understand the implications of different element composition in producing the various outcome of microstructure and phases of the alloys. The phase analysis aims to analyse the effect of different phases in alteration of Young's modulus. XRD will be used to identify the phases of the samples, whereas Thermo-Calc is applied to observe the phase diagram, the number and amount of the phases present at different designated temperatures and compositions. Thus, the collaboration package between microscopy observation and phase analysis can be used to link the relationship between the element's composition and the Young's modulus value. Hardness of the samples will be compared in nano and micro scale to ensure the results obtained are compatible. Young's modulus will be measured via nanoindentation system. The necessary measurements will be done at least twice to confirm the stability and reliability of the testing equipment and also the samples fabricated.

In this report, efforts would be done to understand the logic behind the microstructure or phases observed in Ti-Nb-Zr alloys. Discussion and analysis of the findings and the contribution factors that lead to the results obtained will be outlined. The alteration of composition decided has been based on an arbitrary selection which utilises intervention such as research, feasibility study and testings. However, through systematic analysis, detailed experiments and phase diagram studies, a suitable set up proportion of the new generation Ti-Nb-Zr alloy could be achieved.

This page is intentionally left blank

CHAPTER 3



Methodology

- 3.1 Fabrication of β -phase Ti-Nb-Zr Alloys
- 3.2 Microstructure Characterisation
- 3.3 Alloy Assessment

3.1 Fabrication of β -phase Ti-Nb-Zr Alloys

For the present work, the samples were fabricated in the Department of Materials Science and Engineering at Beihang University, Beijing, China via conventional arc melting furnace. The raw materials used were Titanium, Niobium and Zirconium. Titanium was obtained from titanium sponge with 99.7% impurity. Pure Niobium from Niobium pieces of 99.95% purity. Pure Zirconium with 99.5% purity was extracted from Zirconium pieces.

The compositions of the alloys for this research are Ti-xNb-7Zr alloys containing 23, 28, 33% wt. Nb. They are Ti-23Nb-7Zr, Ti-28Nb-7Zr, Ti-33Nb-7Zr. (all chemical compositions in this work are in wt.% Table 14). The compositions were decided based on the analysis derived from the literature review of past experiments by various researchers.

Table 14: Purity and wt% of Ti, Nb and Zr

Elements	Ti	Nb	Zr
Purity	99.7%	99.95%	99.5%
Ti-23Nb-7Zr	70% wt.	23% wt.	7% wt.
Ti-28Nb-7Zr	65% wt.	28% wt.	7% wt.
Ti-33Nb-7Zr	60% wt.	33% wt.	7% wt.

Ti is chemically active at high temperatures thus the production of Ti alloys in conventional arc melting furnaces is not feasible and requires a controlled environment, vacuum or inert gas like Argon.

In the process, the metal pieces were weighed and divided into desired size. The metal pieces were then charged into the furnace. The arc melting furnace is DHL-400 type Magnetron-Arc Furnace, shown in Figure 14. The ingots were remelted 5 times in the furnace. As expected, the applied electromagnetic field is capable of stirring the alloy to enhance the uniform distribution of alloying elements. The finished samples were thin disc shape with a dimension of 45-50mm in diameter and 10mm in height, as shown in Figure 15.



Figure 14: Vacuum arc melting furnace schematic diagram⁹¹

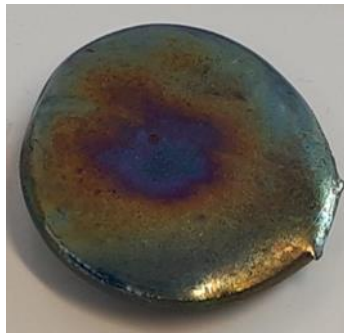


Figure 15: Sample shows homogeneous after melting and casting process

3.1.1 Solution Treatment of Samples

The samples were then homogenized at 1000°C, which is above the β transus temperature⁹² where the $\alpha \rightarrow \beta$ transformation is expected to take place for Ti-Nb-Zr alloy. They were heated for 1 hr under argon atmosphere before water quenched to room temperature. Solution treatment helps to reduce the grain size of Ti-Nb-Zr alloy and also to enhance the microstructure homogeneity of the alloy. The disc-shaped specimens were then prepared for measurement of elastic modulus, microhardness measurement, microstructure examination, and phase analysis by using electrical discharge machining (EDM).

3.1.2 Sectioning of Samples

There are few issues need considering during the machining process. Firstly, Ti with low thermal conductivity tends to succumb to rapid tool wear as heat dissipation is inhibited during cutting. Galling between Ti alloys and the cutting tool occurs easily due to its low hardness and high chemical reactivity properties⁹³. The high strength Ti alloys will significantly reduce the normal tool life. A relatively low Young's modulus property may lead to poor surface finish due to spring-back and chatter phenomenon in the cutting process⁹⁴.

Owing to the concerning aforementioned problems, the sectioning of Ti alloys was performed using Wire cut Electrical Discharge Machine (WEDM) (Figure 16) which does not affect the mechanical properties of the alloy while on the other hand is able to reduce material waste and provide a better surface finish to the end product. This technique discharges the electrified current by means of a taut thin wire, which acts as the cathode and is guided alongside the desired cutting path, as wide as three inches and a positioning accuracy of ± 0.0002 ". This precision allows complex, highly detailed and very small pieces items to be produced or machined⁹⁵. Besides, it minimises the direct contact between Ti-alloy and the cutting tool which is beneficial to eliminate chatter, mechanical stress and vibration as much as possible⁹⁶. This cutting process was done by a machine workshop, Toolcraft Pty Ltd at Holden Hill, Adelaide.

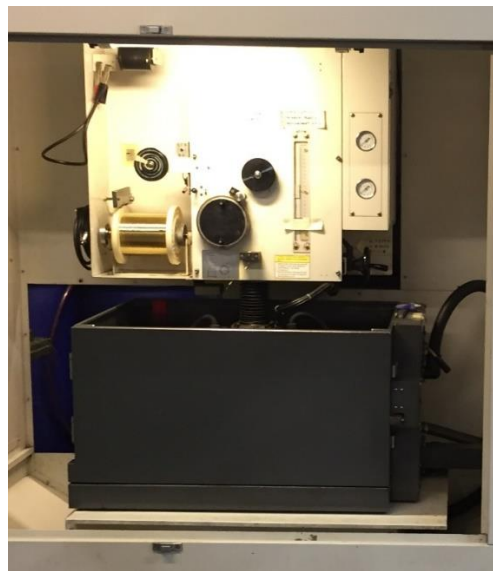


Figure 16: Wire Electric Discharge Machine (WEDM) from Toolcraft

The sectioned sample is shown in Figure 17. The cut surface appeared to be dim as compared to a normal cutting surface which is shiny.

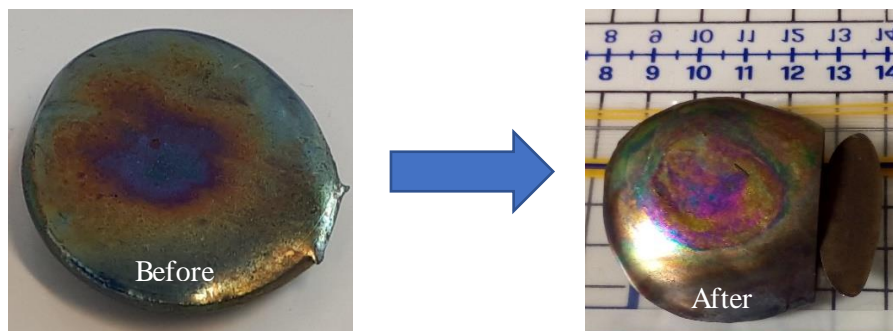


Figure 17: Before and after sectioning the sample with WEDM

As the cut pieces are still too big for mounting and XRD analysis, the samples were cut into smaller pieces at about 5mm in thickness with the diamond cutter (Struers Minitom) as shown in Figure 18. The cutting process took about 50 minutes for one cut.

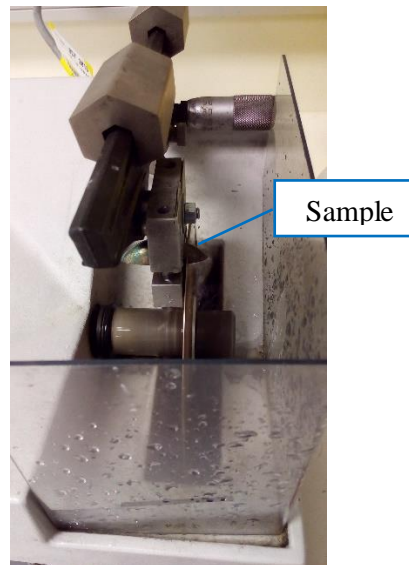


Figure 18: Diamond cutting machine used to cut the samples into adequate pieces for microscope and XRD test

3.2 Microstructure Characterization

Prior to microscopic examination from micro scale to nano scale, the samples were mounted (Figure 20) prior to grinding and polishing. Since titanium alloy is prone to mechanical deformation and scratching owing to its extreme ductility, specific advice and recommendations are required to overcome the typical behaviour of titanium. Struers, the equipment supplier recommended a three-step, automatic method via chemical- mechanical polish to necessitate an excellent and reproducible finishing result for titanium alloy. The proven procedure is illustrated in Figure 19 according to method suggested in ASM Handbook, Volume 9: Metallography and Microstructures. This process was carried out on a Tegramin 25 polishing machine (Struers) as shown in Figure 21.

Preparation Method			
Grinding			
Step	PG 		FG 
		Surface	MD-Mezzo
	Abrasive	Type	Diamond
		Size	#220
	Suspension/ Lubricant	Water	DiaPro Allegro/Largo 9
		rpm	300
	Force [N]/ specimen	40***	30
	Time (min)	Until Plane	5

Polishing			
Step	OP 		
	Surface	MD-Chem	
	Abrasive	Type	Colloidal Silica
		Size	0.04 μm
	Suspension/ Lubricant	OP-S*	
		rpm	150
	Force [N]/ specimen	30	
	Time (min)	5**	

Figure 19: 3-step, automatic grinding and polishing method for titanium alloys⁹⁷

The first step in the grinding process is plane grinding. The alloy was ground using silicon carbide foil of 220 grid size, at 300 rpm with a force of 15N. The lubricant used was water and samples were ground for 5 minutes until they are plane and flat. Plane grinding is then followed by a single fine grinding step with resin bonded diamonds in a rigid disc on a hard surface such as MD-Largo, an abrasive 9 μm diamond suspension. The lubricant recommended at this stage is DiaPro Allegro with the grinding speed of 150 rpm running for approximately 5 minutes. A high force of 40N was suggested during this process to discard the additional surface scratches, impurities and to enhance the surface finishing prior to the last step. The final step of the process involved a chemical-mechanical polishing method. The disc used was MD-Chem of abrasive type colloidal silica, size 0.04μm. OP-S was combined with hydrogen peroxide (H₂O₂) as lubricant in the chemical-mechanical polishing process. The mixture was 90% OP-S with varying concentration of 10-30% H₂O₂. This lubricant is established for polishing titanium and titanium alloys by accommodating the chemical additions without turning into a gel-like viscosity. The silica suspension was applied to continuously remove the residue product from the reaction between hydrogen peroxide and titanium to ensure the surface cleanliness and was free of mechanical deformation. Load applied was decreased to 15 N to avoid pencil shapes in single sample preparation of mounted samples, and the time used was 20 minutes at 150rpm. At the last 20-30 seconds of the OP-S preparation step, to ensure a clean sample, water was applied as a cleaning agent to rinse the sample, rotating cloth and holder.



Figure 20: Mounting machine for sample preparation

The samples were then etched to remove the deformed layer deposited during grinding and polishing also to reveal the microstructural detail of the polished mount or the crystalline structure of the sample. The samples were etched using modified Kroll's solution (3% HF, 5% HNO₃ and 92% H₂O). The samples were immersed into the solution for approximately 60 seconds (Figure 22), flushed with water and then dried in a fume cupboard. It is very important not to over etch or under etch the sample, otherwise the main features would be either obscured or indistinguishable.



Figure 21: Polishing machine



Figure 22: Samples in etching process

3.2.1 Microstructure Examination

Optical Microscopy and Scanning Electron Microscopy are fundamental inspection methods in microstructure examination. Both techniques are distinguished by the source of the beams used to analyse the sample. For optical microscopy, a beam of light is applied to the sample, whereas for scanning electron microscopy, a beam of electrons is used to interact with the sample.

In comparison, the purpose of using optical microscope is an ideal and immediate method to observe the microstructure straight away after the sample preparation. It was also used to confirm that the surface polishing was done accurately before proceeding with more tests. The scanning electron microscopy on the other hand offers an incredibly detailed topographical and compositional information. Three types of detectors are applicable in SEM., which are Secondary Electron Detector (SED), a Back-Scattered Electron Detector (BSED), and an Energy Dispersive Spectrum Detector (EDS). All these detectors were used to observe the fabricated samples. SED was used to observe the topographical information. BSED was used most frequently to view the basic topographical and basic compositional information, which was associated with EDS to obtain detailed chemical compositional data⁹⁸.

3.2.1.1 Optical Microscopic Observation



Figure 23: ZEISS Optical Microscope used for porosity and microscope observation

Microstructure of the samples were observed under microscope from magnification at minimum 5x to maximum 100x using Zeiss Axio Imager Polarizing Microscope (Figure 23).

3.2.1.2 SEM with EDS Analysis

Microstructure observation of the samples were carried out using Scanning Electron Microscope Quanta 450 with EDS Analyser (Figure 24). Samples prepared must be able to fit on the sample stage and

withstand the vacuum conditions as well as the high energy electrons beam. It is necessary to check the vacuum level before proceeding. The vacuum indicator light must be displayed in green with pressure $<9e-3$ mbar and to ensure that the sample holder will not touch the SEM column by CCD. The chamber must be vented before placing in and taking out the sample. The stub in the sample holder was then mounted and screwed just right or otherwise the thread will be damaged. The height of the sample holder including the stub was adjusted to below 10 of the scale by using Z knob of the stage controller on the SEM chamber door. The door was closed, and the pump was activated. When the pressure dropped to less than $9e-3$ mbar and the vacuum indicator was presented in green, the electron beam was switched on. CCD monitor was then activated. It is important to make sure the sample holder will not hit the SEM column during the whole process. The centre position of SEM was set and position X and Y of the control panel (F) was confirmed.



Figure 24: Scanning Electron Microscope Quanta 450 with EDS Analyser

The samples are mounted on a stub of metal with carbon adhesive. The adhesive was extended to slightly overlapping the sample at the top of the mounting. This step was necessitated to prevent charging, a phenomenon that happens when the number of incident electrons is greater than the number of electrons escaping from the sample, resulting in a negative charge builds up at the point where the beam hits the sample. This scenario may cause unusual effects such as abnormal contrast and image deformation and shift⁹⁹.

The quantitative analyses of elemental constitution (wt% of Ti, Nb and Zr) were also calculated with EDS analyser from the same equipment using EDAX software. As a general rule for comparison, the same settings such as KV, working distance, magnification, spot size, beam current, scanning speed and live time were applied for all spectra and the setting conditions were recorded in Table 15.

Table 15: Operating conditions for quantitative analysis using EDS on Quanta 450 SEM

Parameter	Value Settings
Accelerating Voltage	20 kV
Beam Current	120 pA
Spot size	4
Scan rate	≤ 300 ns
Live time	100 seconds
Working Distance (WD)	9~10mm
Magnification	50x-20000x

3.2.2 Thermo Calc Phase Analysis

The ternary diagram for Ti-Nb-Zr alloy was produced with Thermo Calc software, one of the methods available in CALPHAD. Thermo-calc software was accessed via The University of Adelaide. The diagram was created with 3 axes representing the weight percentage of each element at selected temperatures. The diagram itself represents an equilibrium state, implication of stable or metastable regions existed within the solution of the alloy substances. The ternary diagram for Ti-Nb-Zr was produced at various temperatures, ranging from 27°C to 627°C to observe the changes and alteration of phases according to the temperature. Binary diagram for Ti-Nb, Ti-Zr and Nb-Zr were plotted to identify the phases present within a wide range of temperature at different concentration of the elements. Scheil Solidification Simulation was used to predict the phases exist at the specific temperature or at equilibrium state. Another function applied was ‘Property model calculator’ to study the transition temperature of each phase.

3.2.3 Phase Analysis (XRD)

Phase analyses of the alloys were conducted on an x-ray diffractometer (Rigaku MiniFlex600 XRD - Figure 25). The samples used for XRD analysis must be polished to ensure a smooth surface were cut to a maximum of 5mm in thickness due to the limited gap in the sample holder. The scanning speed was set at 1.25° min⁻¹. CuK_α ($\lambda = 1.5418\text{Å}$) radiation was used at the operating condition of 40 kV and 15 mA. The XRD data were collected over the 2 θ range of 30–80° with a step size of 0.02°. Preparation of the sample was done carefully without the exposure of any unrelated elements on the X-ray.

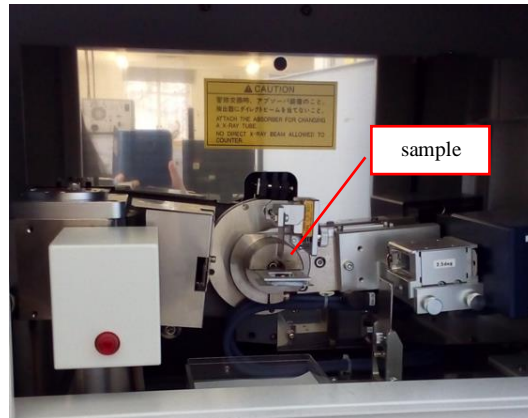


Figure 25: XRD Machine

3.3 Alloy assessment

The methods used to assess the hardness properties and Young's modulus of the alloys are microhardness tester and nanoindentation system.

3.3.1 Microhardness Measurements

Microhardness measurements were made on the polished surfaces of the samples by using LM 700AT Microhardness Tester (Figure 26) with Vickers diamond pyramid indenter to observe the alloy's ability to resist plastic deformation when a compressive force is applied. The hardness samples were obtained from the three groups of samples having different element constituents. The Vickers hardness was measured at the surface of the sample with a load of 100 gf and a holding time of 20 s. The diagonal length of the square is approximately $70\mu\text{m}$. The distance between 2 micro indentations should be at least 3 times its diagonal length. Thus, the indentation was distanced $250\mu\text{m}$ from each other. An average of 7 readings was taken from each sample with a triangular matrix (Figure 27).



Figure 26: LM 700AT Microhardness Tester

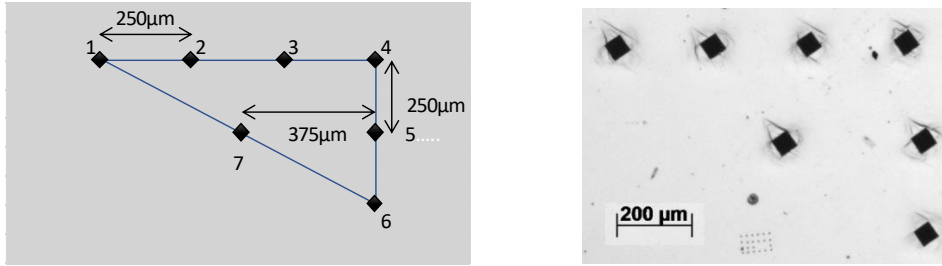


Figure 27: Matrix for microhardness measurements

3.3.2 Young's Modulus and Nanoindentation

Nanoindentation measurements were made on the polished surfaces of the samples after microhardness test. The test is carried out with IBIS Nanoindentation System (Figure 28) with Berkovich indenter according to ISO 14577 Test Method. This instrument is aiming to measure the mechanical properties of materials with small volumes. The materials properties measured for this thesis are elastic modulus and hardness. The range and resolution of the force and displacement (depth of penetration), is in the mN, μm nm resolution. An average of 24 readings was taken from each sample in a rectangular matrix (Figure 29). The distance between the indentations is $15\mu\text{m}$. Figure 30 compares the indentation between the micro size and nano size. The test results were plotted in the graphs with force (P-mN) against depth of penetration (ht- μm).

Table 16: Specifications for Nanoindentation

Head	Specifications
Load range	500 mN
Minimum contact load	5 μN
Depth range	20 μm
Working distance	61 μm



Figure 28: IBIS Nanoindentation machine

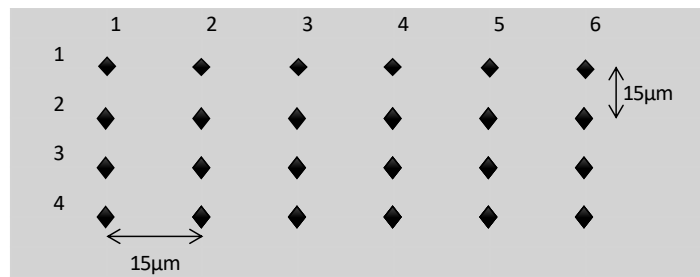


Figure 29: Matrix for nanoindentation measurements

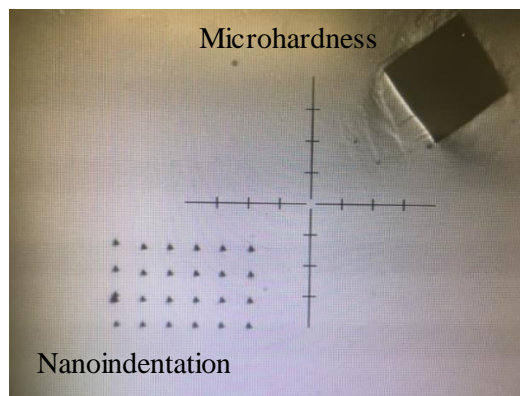


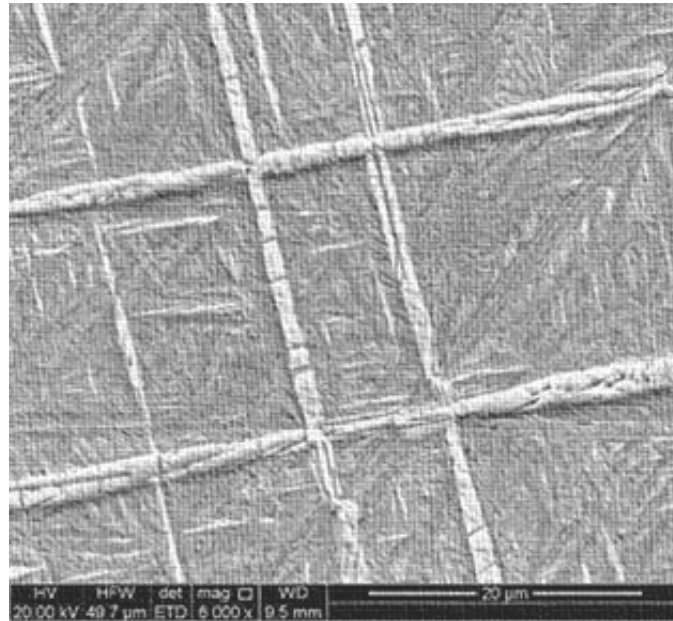
Figure 30: Microhardness and Nanoindentation marks

Summary of Chapter 3: Methodology

This chapter explains the fabrication process, experiments, testing conducted for alloys analysis and assessment purposes. The samples were casted through arc melting. Samples preparation was carried out according to the metallographic standards for titanium alloy. Optical microscope and SEM with EDS analyser were used for microstructure examination. XRD was employed to analyse the phases presented. Microhardness tester and nanoindentation system were utilised to measure the hardness properties and Young's modulus.

This page is intentionally left blank

CHAPTER 4



Results

- 4.1 Microstructure Results (Optical & SEM)
- 4.2 Thermo Calc Results
- 4.3 XRD Results
- 4.4 Microhardness Results
- 4.5 Nanoindentation Results
- 4.6 Chemical Composition Results
- 4.7 Homogeneity

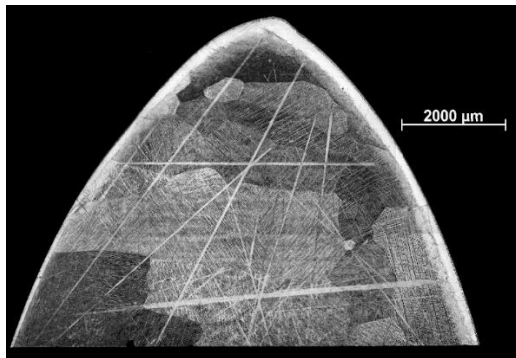
4.1 Microstructure Results

The microstructure of the alloys was observed through two sets of equipment, which are optical microscope and SEM with EDS. The optical microscope is a faster way to produce the magnified surface image of the samples, to observe the porosity, grains, and grain boundaries and to compare the etched and unetched samples. SEM was employed to observe the surface morphology of the sample in depth, and EDS to analyse the chemical composition of the alloys at specified spots as well as to map the chemical composition over the entire surface of the alloy.

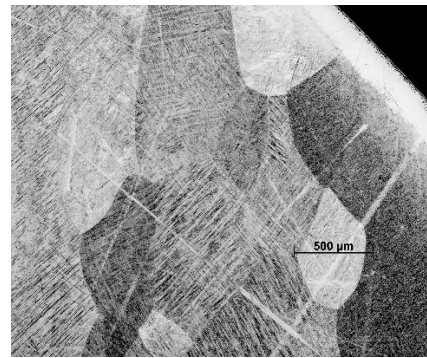
4.1.1 Optical Microscopy

i) Sample 1 – Ti-23Nb-7Zr

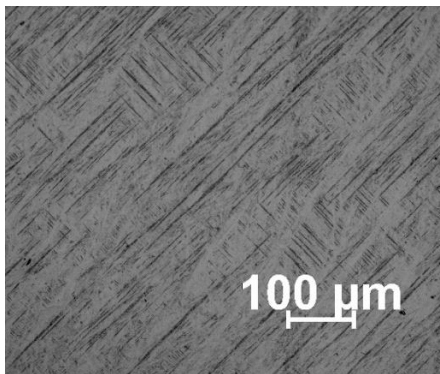
a) Etched, Magnification 5X



b) Etched, Magnification 5X



c) Etched, Magnification 50X



d) Etched, Magnification 50X

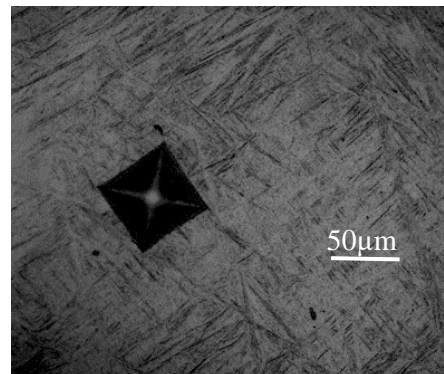


Figure 31: Optical images of sample 1 – Ti-23Nb-7Zr

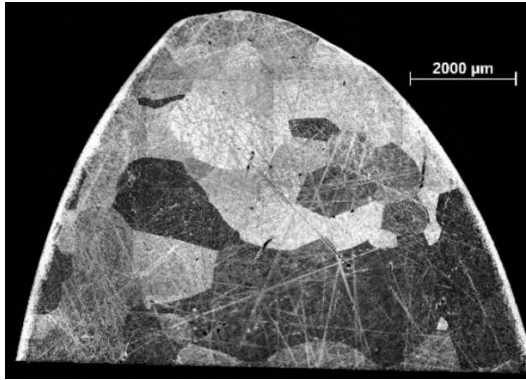
Figure 31 gives an overall bright field optical micrograph of Ti-23Nb-7Zr alloy. Figure 31 a) reveals a clear polycrystalline structure of coarse grains with varying size and orientation. Most of the grains are seen elongated horizontally while a small number of the grains are in nodular shape. The lengthened grains are concentrated on the left, bottom and top sides, oriented in landscape mode. The grains size ranges from few hundred to thousands of microns with their varying shapes. The recrystallized beta grains are observed along the prior beta grain boundaries¹⁰⁰. Majority of the grains have the acicular

martensitic structure aligned in one direction whereas some of the grains are noticed with the lamella structures that are perpendicular to each other. A minority of Widmanstätten structure is also embedded in some of the grains, especially those near to the outer surface of the sample.

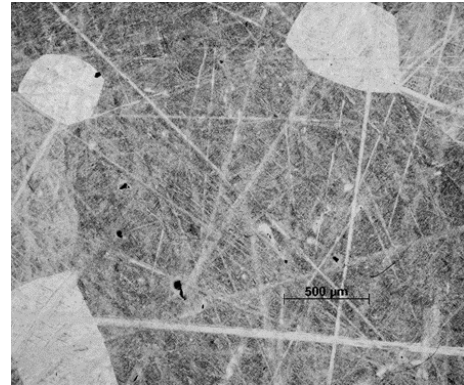
Figure 31 b) shows alpha (martensite) of different structure and orientation embedded in the coarse grain of β matrix. The morphology revealed two distinctive martensitic structure upon the etching process. They are acicular alpha and Widmanstätten alpha. However, the Widmanstätten alpha structure is densely located near the edges and as it started approaching the centre of the sample, the alpha structure gradually converted into acicular shape. A couple of grains are compacted with the martensitic structure with some grains are having scarcely scattered alpha. Also, the observation displayed a grain can be consisted of either one type or a combination of multiple structure. The mildly intersecting needle-like structure also appeared in some of the grains which are low deformation twins. And when they come across the grain boundaries or meet another twin, the deformation twins “pinch off” and discontinued next to the internal boundaries. Figure 31 c) is of 50 magnification that shows the presence of thin lamellae resembling needles in a basketweave appearance, a characteristic of alpha (martensitic) structure, oriented in multiple directions, perpendicular to each other. There are also some deformation twins, which appear needle-like and intersecting each other. The discontinued lines (needles) are longer in one direction (measuring about $500\mu\text{m}$) compared to the needles in the opposite direction (approximately $100\mu\text{m}$). In Figure 31 d), the acicular martensitic structure spreads randomly across the surface via Widmanstätten pattern. The primary, secondary and tertiary α ’ are also observed.

ii) Sample 2 – Ti-28Nb-7Zr

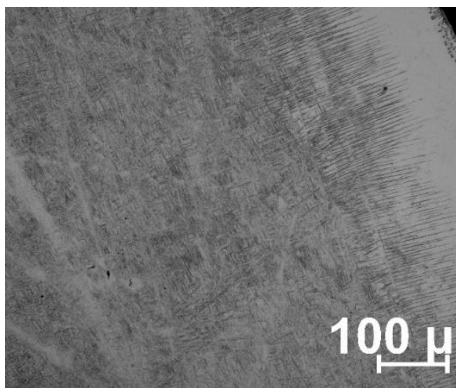
a) Etched, Magnification 5X



b) Etched, Magnification 5X



c) Etched, Magnification 20X



d) Etched, Magnification 50X

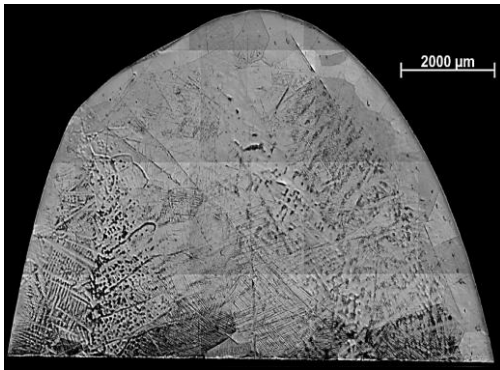


Figure 32: Optical images of sample 2 – Ti-28Nb-7Zr

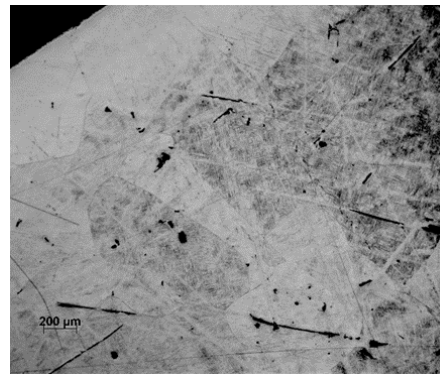
Figure 32 gives an overview bright field optical image of Ti-28Nb-7Zr alloy. The presence of polycrystalline grains in Figure 32 a), sample 2, are visibly smaller than the grains size in sample 1 with heterogeneous grains consisted of elongated and spheroidal grains although the elongated grains are more dominant and concentrated at the bottom. The grains are not equiaxed and orientated in varying direction. The grains size, however also varies from a few hundred to thousands of microns meter. In Figure 32 b) fine acicular martensite was present within the coarse grain. Some pores are observed originated from the impurities found. There is a notably large difference in the grains size in this figure. Figure 32 c) shows the presence of thin acicular α' martensitic structure, with the needle like structure. This structure became longer, more profound and aligned when approaching the surface boundary. The α' martensitic structure expands uni-directionally near the boundary of the sample, whereas the martensitic structure at the centre scatters in disorganized direction. Besides, the discontinued needle-like structure that is closer to the centre is very fine/thin and substantially shorter than the acicular martensite near the boundary. The majority martensitic structure is in basketweave pattern which is low-deformed. Figure 32 d) shows discontinued, fine acicular alpha in the non-uniform Widmanstätten microstructure. The majority needle-like structure is shorter than $50\mu\text{m}$, and they are longer in size horizontally versus vertically.

iii) Sample 3 – Ti-33Nb-7Zr

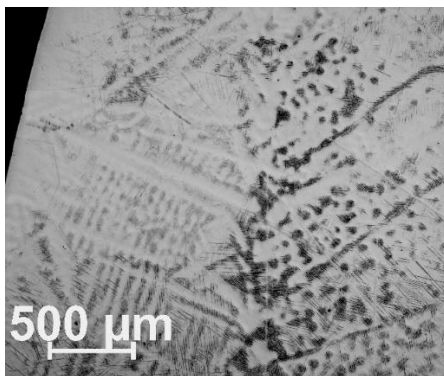
a) Etched, Magnification 5X



b) Etched, Magnification 5X



c) Etched, Magnification 5X



d) Etched, Magnification 100X

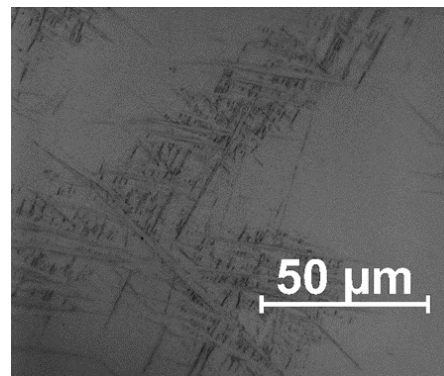


Figure 33: Optical images of sample 3 – Ti-33Nb-7Zr

Figure 33 resembles an overall bright field optical image of Ti-33Nb-7Zr alloy. The polycrystalline coarse grains in Figure 33 a) are subtle compared to samples 1 and 2. The average grains size for sample 3 is more homogeneous among all samples (along the sample boundary) although also differ in size and orientation. However, nodular shaped grain size is more dominant in this sample. Fine needle-like martensitic structure dispersed over the surface randomly but mostly centralised at the bottom. Some grains have relatively small amount of or none martensitic structure. In Figure 33b) acicular martensitic structure arranged in the basketweave pattern is prominent at some bigger grains but scarcely distinguished in smaller grains. This structure is not found on the white straight lines, but few black lines appear in some part of the white ones. There is a broader quantity of pores or impurities in this sample, with the biggest pore stretches to a length of 100μm. Figure 33 c) features a negative and positive image usually produced in photography. The left region favours the negative image whereas the right part is more related to the positive image. Very fine acicular martensitic structure is embedded in platelet and are distributed crosswise across the surface. The dendrite structure is displayed explicitly in the left region of the picture. The primary dendrite arm branches up to 50μm. In Figure 33 d), discontinued acicular martensite structure is observed perpendicular to each other as shown in the basketweave pattern. This structure only contributes to a mere 40% of the total surface. Additionally,

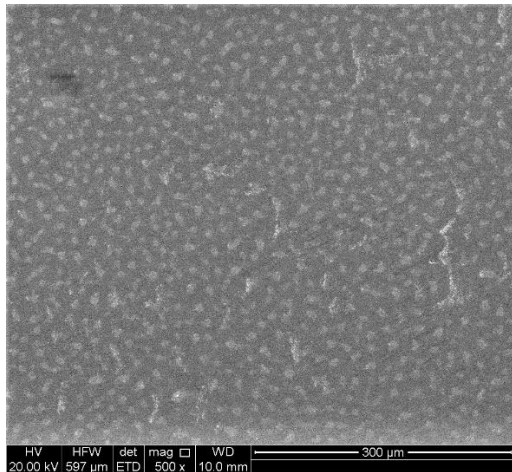
several pipette shaped lines are observed spanning diagonally in varying length along the acicular martensite structure. The longest pipette shaped line is of 100 μ m in length.

4.1.2 SEM Results

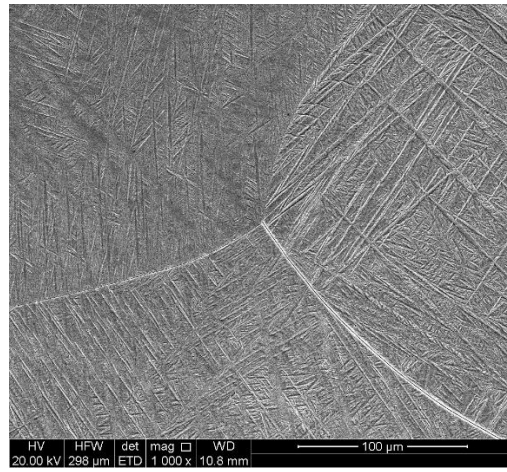
The SEM micrographs were observed before and after etching process.

i) Sample 1 – Ti-23Nb-7Zr

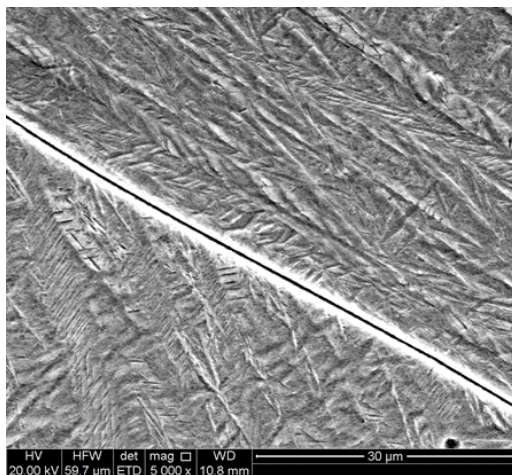
a) Unetched, Magnification 500X



b) Etched, Magnification 1000X



c) Etched, Magnification 5000X



d) Etched, Magnification 6000X

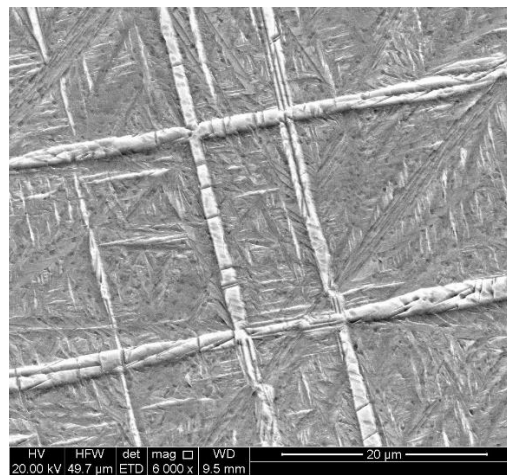


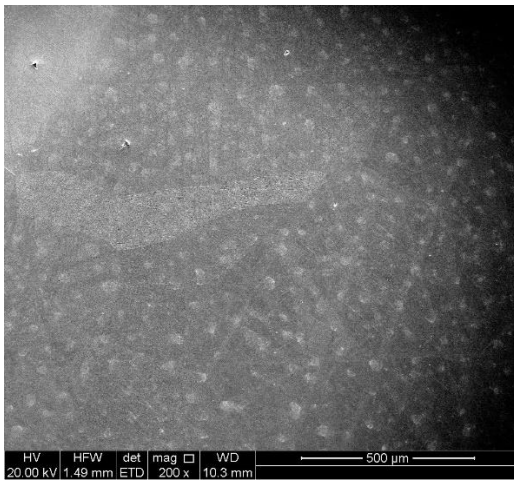
Figure 34: SEM micrographs for Ti-23Nb-7Zr

Figure 34 a) indicates the surface morphology of Ti-23Nb-7Zr with 500X magnification. A uniform distribution of dim light spots was apparently distributed all over the surface. There are approximately 15-17 spots within the length of 300 μ m. Figure 34 b) shows the intersection/boundaries between three beta matrix grains. The acicular martensitic structure between the three grains represents a trend of varying orientation and coarseness of the basketweave structure. The strands in the grain of the coarser structure wove about 100 μ m. The strands in the finer structure formed a discontinued needle-like structure. In the grain of coarser structure, the primary α'' appears raised and is identical to a hump on

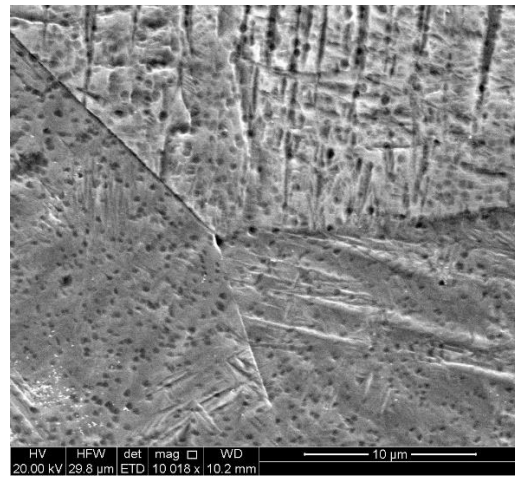
the surface. Whereas the acicular alpha in the grain with fine basketweave pattern resembles a trough which seems submerged below the surface. The deformed twins in the coarser structure indicated a “pinch off” effect before discontinued at the grain boundaries. The nucleation of grains is initiated at the prior beta grain boundaries with the recrystallized beta grains also observed. Additionally, both fine and coarse prior beta grain boundaries are distinguishable in the same figure. The structure in Figure 34 c) consists of acicular (secondary) alpha, the transformed beta. Prior beta grain boundary is prominent in the white region of straight line. Disoriented acicular alpha grain nucleated on crystallographic planes of the prior beta matrix is observed. A series of acicular alpha structures is noticed oriented in the same alignment near the left edge of the sample, which is very similar to the slip band structure. Figure 34 d) shows an obvious basketweave pattern consisted of deformation-induced α'' martensite in a beta matrix which is formed by the quenching process¹⁰¹. The sharp α'' martensite stretches irregularly within the structure. The transformed platelets of alpha arranged in columnar line crossing each other with the width and length of 10 μ m and 100 μ m respectively. Pores of width less than 5 μ m were scattered all over the area. Various sizes of thin lath martensitic microstructures are embedded in a matrix of coarse laths stretching diagonally across the surface.

ii) Sample 2 – Ti-28Nb-7Zr

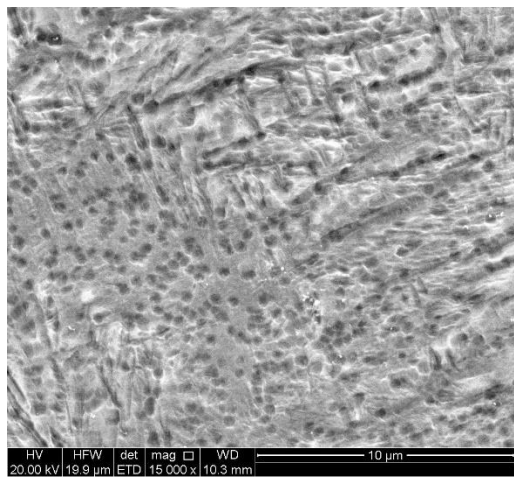
a) Etched, Magnification 200X



b) Etched, Magnification 10000X



c) Etched, Magnification 15000X



d) Etched, Magnification 2500X

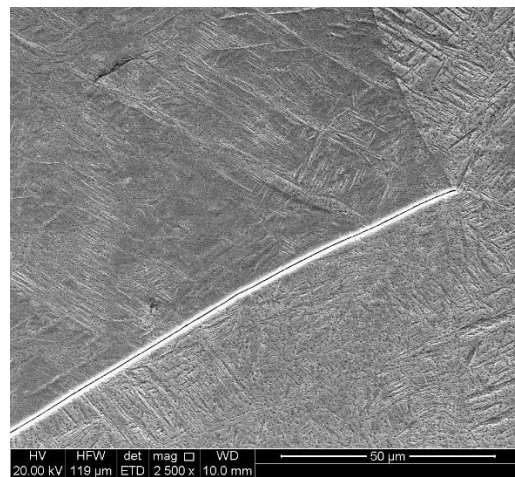


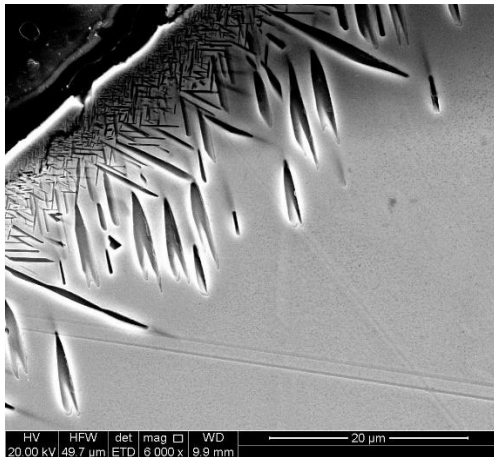
Figure 35: SEM micrographs for Ti-28Nb-7Zr

Under 200X magnification (Figure 35 a), it is noticeable that the distribution of the white phase is relatively uniform. The fine, white phase is the unresolved alpha precipitation in an aged beta matrix with dark background. Approximately 6 spots are scattered within a 50 μ m range. During the precipitation of alpha, it solidified as dendrite, which then slowly nucleated and grew into beta grains. This figure shows the cross sectional of the dendritic structure, where the white phases are the tertiary dendrite arms. Figure 35 b) shows the intersection of three individual grains at magnification of 10000X. The grains have different structure and orientation. Twinned athermal α'' martensite is heavily precipitated in the top grain, favouring a platelike structure with most of them aligned vertically. Acicular martensitic structure is moderately dispersed in the bottom right structure and aligned in the horizontal direction. However, the acicular martensite structure is rarely observed in the left bottom grain. In Figure 35 c) equiaxed pores of 500nm are distributed across the surface at a distance of 20 μ m from each other. An evident of thin film of alpha phase (light) is clearly seen at the prior beta grain

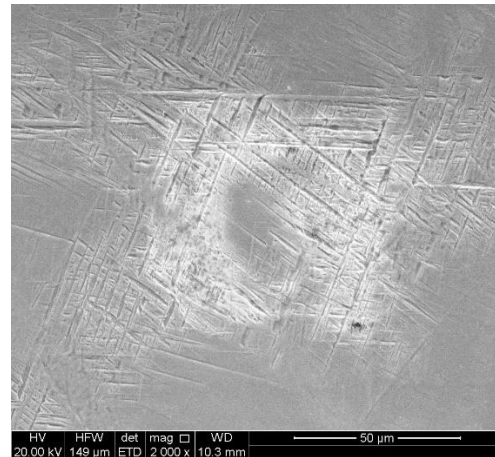
boundaries as illustrated in Figure 35 d), where precipitation normally occurs on multiple orientations planes. Although the bigger grain demonstrated an irregular orientation of platelike structure, some parts are observed having this structure aligned continuously in the same position. The coarseness and amount of martensitic structure changes in between the varying grains and are dissimilar from each other. The lath martensite on the top right corner is shared between two grains.

iii) Sample 3 – Ti-33Nb-7Zr

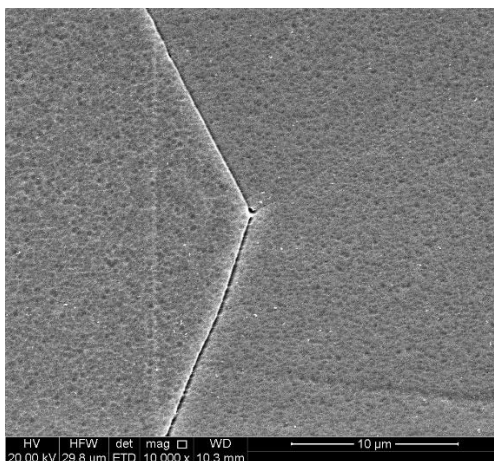
a) Etched, Magnification 6000X



b) Etched, Magnification 2000X



c) Etched, Magnification 10000X



d) Etched, Magnification 5000X

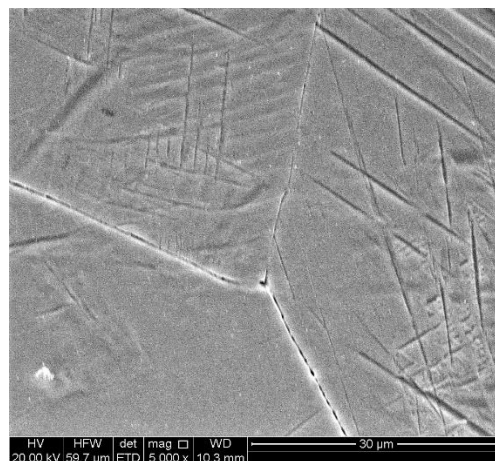


Figure 36: SEM micrographs for Ti-33Nb-7Zr

Figure 36 illustrates the surface morphology of Ti-33Nb-Zr alloy. As illustrated in Figure 36 a), the twinning deformation happened drastically at the surface boundary. The length of the twin varying from shortest at around 1μm to as long as 20μm. The smallest twinning structure is densely assembling at the surface boundary and subsequently expanded in size and length when growing inward. They then stopped abruptly at about 20μm from the edge. No trace of acicular martensitic structure is sighted in the beta matrix in Figure 36 a & c), indicating that this is a stable and dominant β alloy. In Figure 36 b), a random distribution of acicular martensitic structure is observed with lath martensite oriented in

multidirectional. Twinning and slip bands are seen intertwined with each other. Figure 36 c) clearly demonstrates a full beta matrix across the faces of the sample. Pores of similar cavity are densely populated throughout the whole area. Grain boundary of prior beta shows a distinct trim through the grain. Figure 36 d) shows long grains of alpha transformed along certain beta matrix planes, similar to platelike appearance. The thin needle like structure spans from a few μm to $30\mu\text{m}$ and it is fractionally crisscrossing each other. The grain boundary does not show a continued clear cut. In fact, there were few breaks along it and it is blurry. However, it is noted that the lath is much finer in this sample.



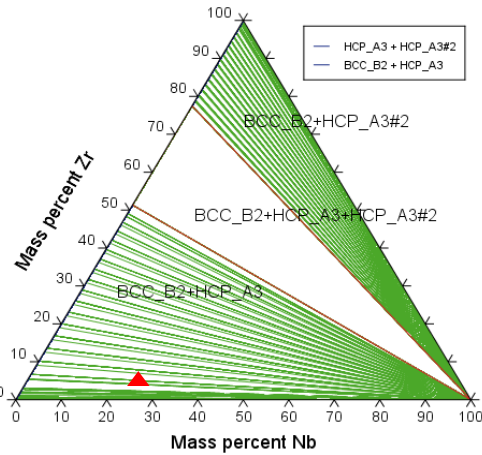
Figure 37: Comparison of acicular and lath martensitic structure

Figure 37 compares the martensitic structure between the samples with the same magnification, which is at 5000x. Sample 1 owns the coarsest and thickest martensitic structure. Not only the size gradually decreases from sample 1 to sample 3, the quantitative observation displays a diminishing amount of martensite from sample 1 to 3 as well. However, the length of the needle structure is comparable between samples 1 and 3.

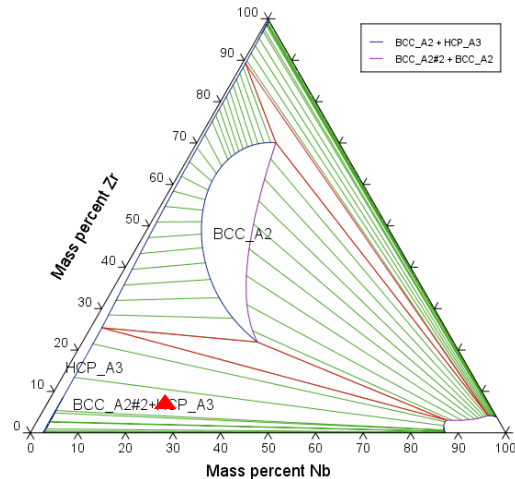
4.2 Thermo Calc Results

The diagram was created with 3 axes representing the weight percentage of each element at elevated temperatures. The diagram itself represents an equilibrium state, implication of stable or metastable regions existed within the solution of the alloy substances. The ternary diagram for Ti-Nb-Zr was produced at various temperatures, ranging from 27°C to 627°C to observe the changes and alteration of phases according to the temperature.

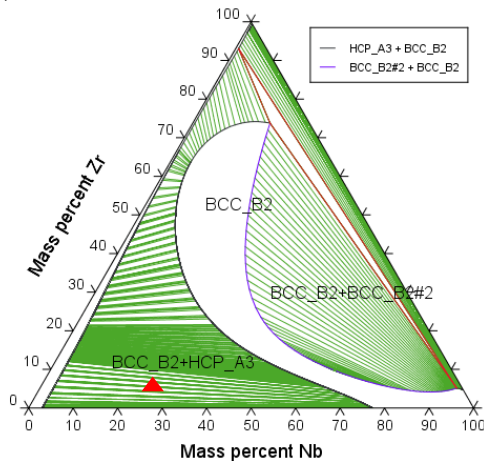
a) 27°C



b) 517°C



c) 557°C



d) 627°C

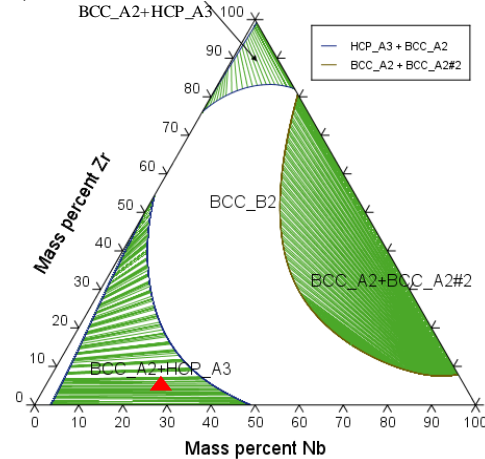
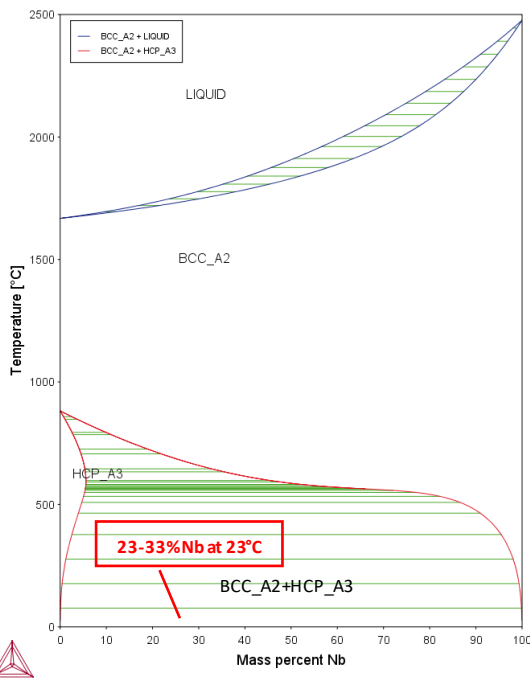


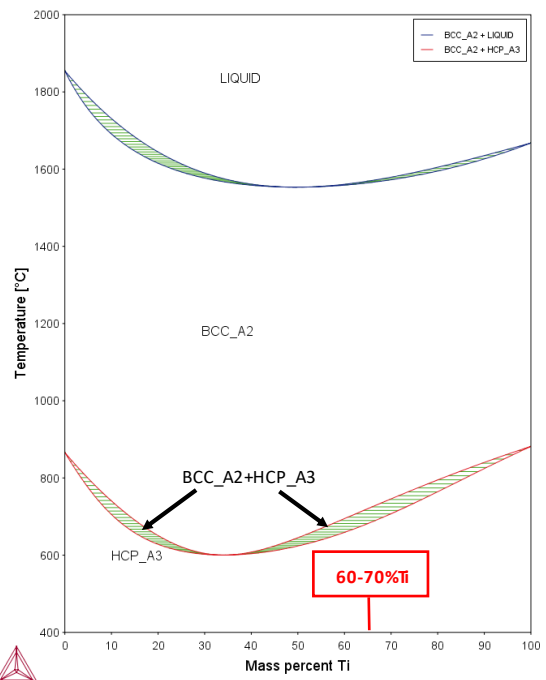
Figure 38: Ternary diagram for Ti-Nb-Zr alloy with increasing temperature, region of interest: ▲

The ternary phase diagram in Figure 38 shows a significant scenario in the transformation of phases in Ti-Nb-Zr alloy with the increasing of temperature. The region of β phase expands as the temperature rises. At higher temperatures, α phase becomes unstable and the crossover from α to β phase takes place at a maximum titanium concentration of 72%, as shown in Figure 38 (d). It also suggests that at higher temperature than 627°C, almost any range of element composition will transform into BCC- β phase. It also indicates that a better solubility of alloying element can be achieved at higher temperatures¹⁰¹.

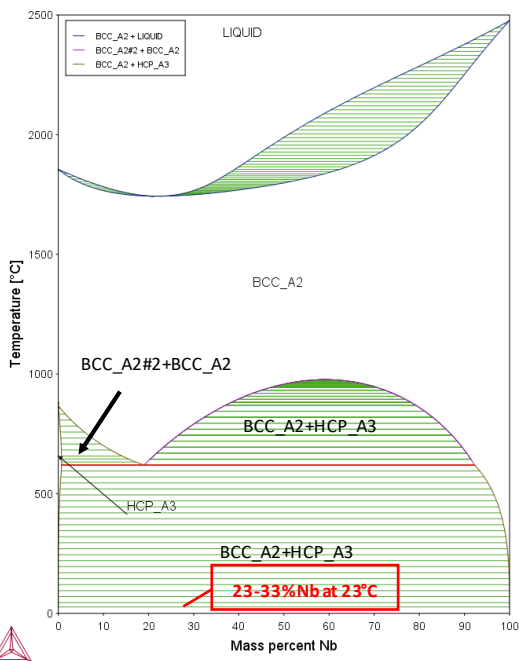
a) Ti-Nb



b) Ti-Zr



c) Nb-Zr



d) Ti-Nb-Zr

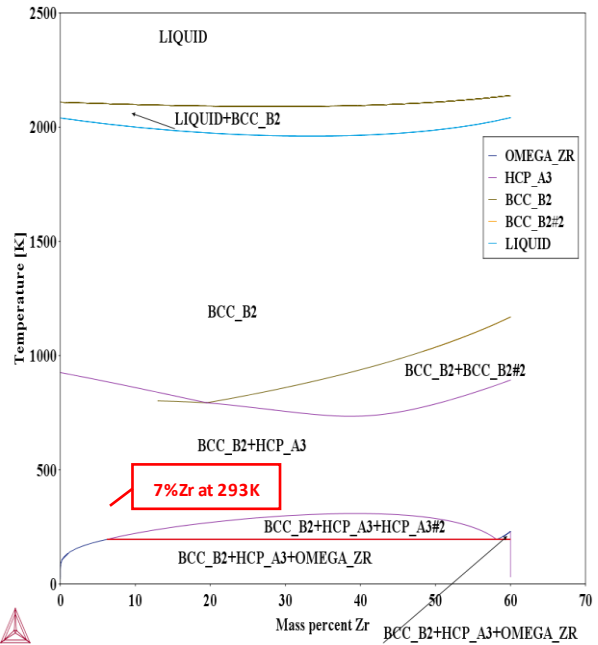


Figure 39: Phase diagrams for the alloying elements with region of interest defined

Figure 39 indicates the phases exist within the solubility of the alloying elements. Binary diagram for Ti-Nb, Ti-Zr and Nb-Zr were plotted at elevated temperature against increasing wt% of the elements. The plots gave a result that there were 2 phases that could possibly exist in the metallographic structure of the samples. At room temperature, both compound of Ti-Nb and Nb-Zr produce BCC+HCP phase

while the solution of Ti-Zr gives an HCP phase. The ternary diagram of multicomponent solid solution of Ti-Nb-Zr alloy synthesizing an existence of the BCC+HCP phase at room temperature.

4.3 XRD analysis

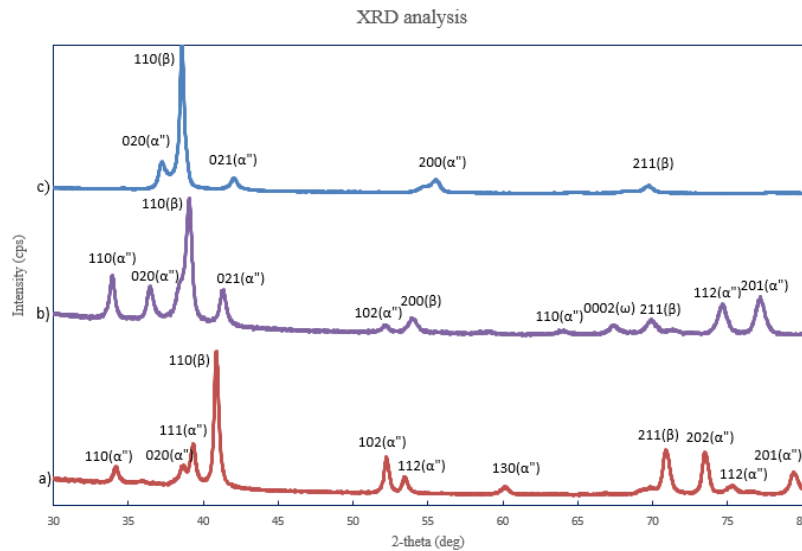


Figure 40: XRD profiles for the three samples a) Ti-23Nb-7Zr, b) Ti-28Nb-7Zr, and c) Ti-33Nb-7Zr

Figure 40 shows the X-ray diffraction patterns of solution treated samples based on XRD profiles from the literatures focusing on Ti-Nb-Zr alloys of similar fabrication process^{77,102}. The results from the experiments were consistent with the phases indicated in the literatures, indicating that the alloys are composed of α'' phase (orthorhombic martensite) in the beta matrix. The 110(β) phase contributes to the highest intensity for all samples, at around 40°. Most peaks are diffracted in the Ti-23Nb-7Zr sample, with predominant α'' martensite in beta matrix. A low intensity peak representing ω phase is traced in sample 2, Ti-28Nb-7Zr alloy at 68° of structure 0002 with large fractions of peaks composed α'' and β . The XRD characterization of the samples subjected to 33wt% of Nb indicated that less peaks were identified. Moreover, the corresponding peaks identified a relatively fewer α'' phase in sample 3. In addition, appearance of peaks broadening, and shortening is also notified through plot 1 to plot 3. Nonetheless, it was found that with increasing Nb addition, the diffraction peaks move towards low angle direction with further explanation discussed in Section 5.3.

4.4 Microhardness Results

Microhardness results of seven individual points for each sample are listed in Table 17. The microhardness for sample 1 ranges from 183.7HV to 199.4HV. Sample 2 has the lowest hardness at point 1 with 179.8HV and hardest indentation at point 6 with 188.4HV. Sample 3 of 33%Nb has an overall lower hardness average that spans between 150.5HV to 156.5HV.

Table 17: Microhardness results of the samples (each of 7 points) with average and standard deviation

Points	Hardness (HV)		
	Ti-23Nb-7Zr	Ti-28Nb-7Zr	Ti-33Nb-7Zr
1	189.4	179.8	156.5
2	185.4	180.9	154.8
3	190.2	186.5	152.4
4	186.9	182.9	153.6
5	183.7	188.0	150.5
6	199.4	188.4	154.3
7	191.3	185.5	155.8
Average	189.5	184.6	154.0
STDEV	5.147	3.416	2.049

Figure 41 displays the point number where the hardness was measured. Since the surface of the indentation was conspicuous after the etching process, nevertheless the comparison of the hardness can be distinguished and justified from the plastic deformation and surface morphology from the microscopy figure.

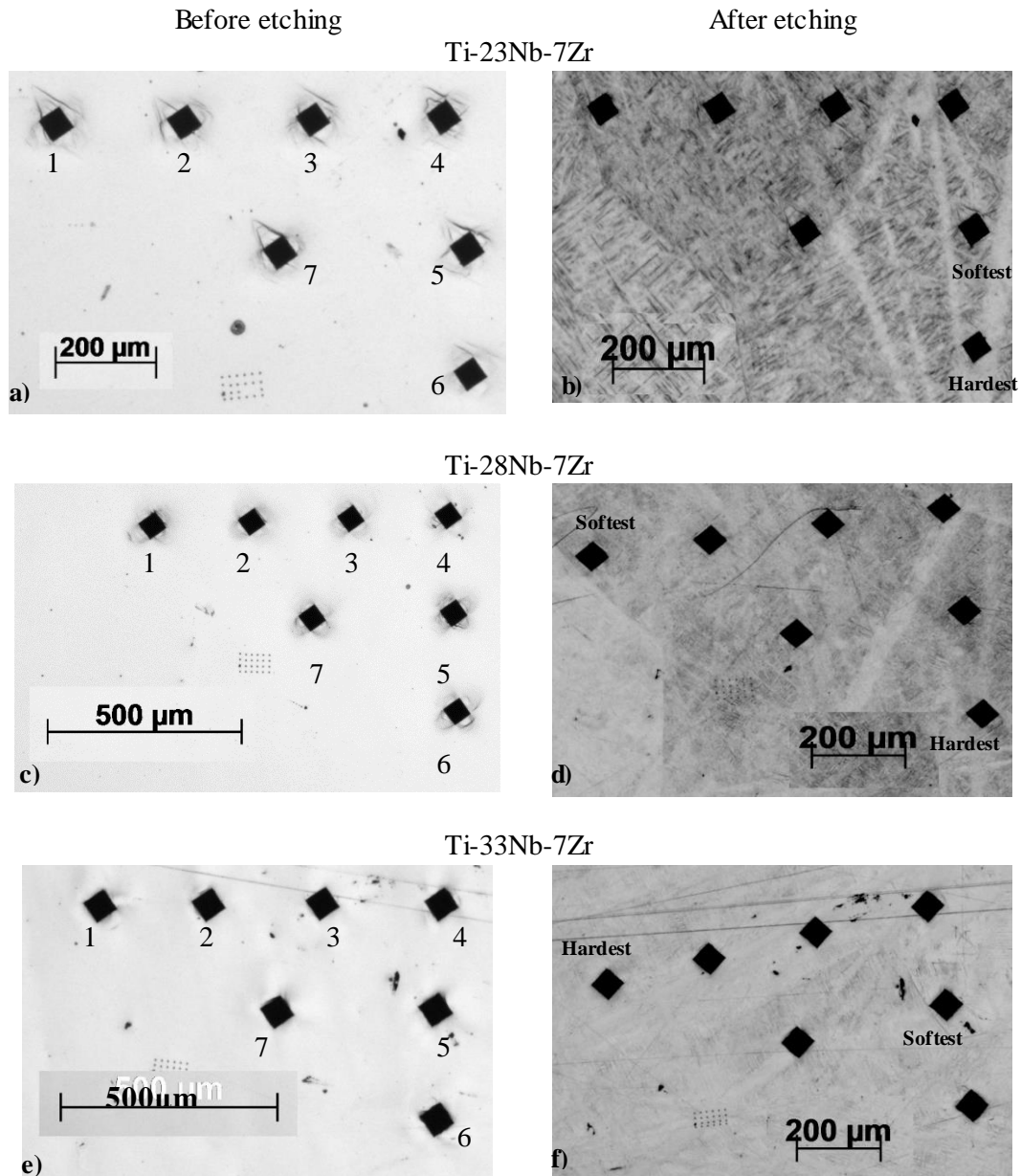


Figure 41: Comparison of hardness points before and after etching and marking of points

Sample 1 has an exceptional high hardness at point #6 in Figure 41 a), and it is noticeable from the plastic deformation around the marks as point #6 has the least deformation. Shown in Figure 41 b), point #6 is the only point located in the range of the white line, whereas the rest of the points were situated on the martensite structure in the beta matrix. All the points measured were taken within one single grain.

All the points measured in sample 2 (Figure 41 d) happened to be located within the same grain. The range of difference between the biggest and smallest hardness value is 8.6HV. All points, except point #4 and #6, are measuring the martensitic structure in the beta matrix. Those two points basically sit in the intersection between the martensitic structure and the white line. However, their hardness values are

quite different as point #4 was measured of 182.9HV and point #6 is hardest of all with 188.4HV. Point #1, with the lowest hardness value is closest to the grain boundary.

The morphology characteristic in sample 3 displays a stable beta matrix with less proportional of martensitic structure. Point#5 possesses the softest spot in associated with the greatest plastic deformation appeared in the indentation. The hardness values are more consistent with the range differs at only 6 HV with low standard deviation of 2. All the measurements were also located on the same grain.

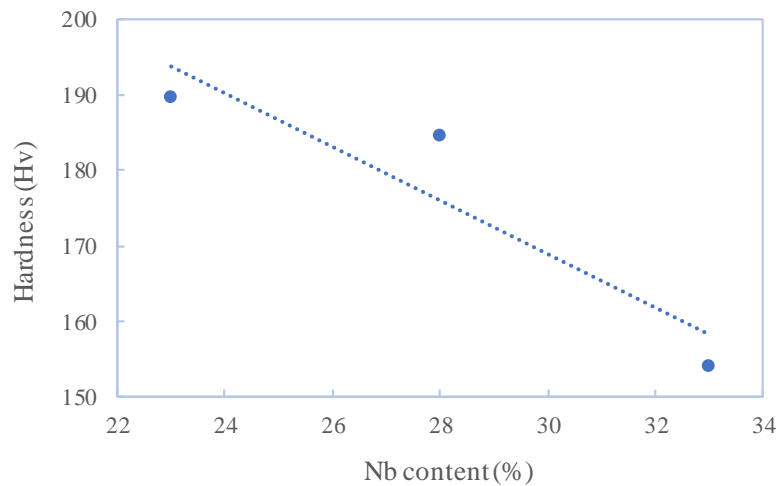


Figure 42: The changes of Vickers hardness with increasing of Nb content%

Figure 42 interprets the changes of microhardness value in conjunction with the percentage increases in Nb content. The hardness drops from increasing the Nb from 23% to 33%.

4.5 Nanoindentation Results

ISO 14577 is the standard for Nanoindentation Testing Method. Hardness and Young's Modulus results obtained are shown in Table 18.

Table 18: Nanoindentation hardness and Young's modulus results for the samples (each of 24 points) with average and standard deviation

Indentation	HV			Young's Modulus (GPa)		
	Ti-23Nb-7Zr	Ti-28Nb-7Zr	Ti-33Nb-7Zr	Ti-23Nb-7Zr	Ti-28Nb-7Zr	Ti-33Nb-7Zr
1	285.460	237.892	316.364	44.886	38.036	49.122
2	290.265	231.428	245.154	46.680	37.597	39.745
3	248.982	231.950	249.694	40.092	37.915	40.423
4	244.682	234.844	254.712	39.446	37.705	41.521
5	239.874	223.174	240.697	38.700	36.124	38.695
6	250.808	235.292	247.651	40.829	38.448	40.014
7	252.410	215.040	243.604	40.958	35.434	39.420
8	244.256	229.250	258.067	39.541	37.143	41.721
9	237.461	230.104	247.002	37.903	37.497	39.802
10	244.663	224.365	264.394	39.269	36.400	42.362
11	247.716	232.768	254.338	40.410	37.092	40.709
12	-	224.778	260.251	39.449	36.572	42.032
12	242.492	239.047	264.069	39.427	39.302	42.851
13	243.239	235.523	257.532	39.844	38.276	42.000
14	240.062	230.790	264.936	38.620	36.888	42.461
15	253.217	236.601	252.459	41.496	37.584	41.333
16	233.725	238.562	240.593	37.544	38.855	39.181
17	233.131	234.273	249.837	37.794	37.807	40.418
18	239.840	240.190	261.017	39.395	39.412	42.164
19	250.340	231.297	260.745	39.900	37.619	41.924
20	247.747	239.650	262.209	40.548	38.884	42.611
21	229.715	224.805	261.924	37.221	36.623	42.387
23	-	222.730	257.637	-	36.050	42.064
24	-	225.029	253.466	-	36.222	40.907
Average	247.6	231.2	257.0	40.0	37.5	41.5
STDEV	14.837	6.503	14.712	2.250	1.067	2.024

Table 18 compares the nanohardness value and Young's modulus results for the samples. The analysis has shown a close relation between the hardness value and the elastic modulus. The results from the table exhibit a higher hardness value yields a stiffer material with greater elastic modulus. 28wt% Niobium in the sample appear to offer the lowest hardness value at 231HV, also the lowest Young's modulus with 37.5GPa. The biggest percentage of Niobium at 33% measured the hardest value at 257HV and subsequently the highest Young's modulus at 41GPa. In contrary to that, the alloys with

the lowest alloying element composition at 23%Nb marked a medium value of both hardness (247.6HV) as well as the Young's modulus (40GPa).

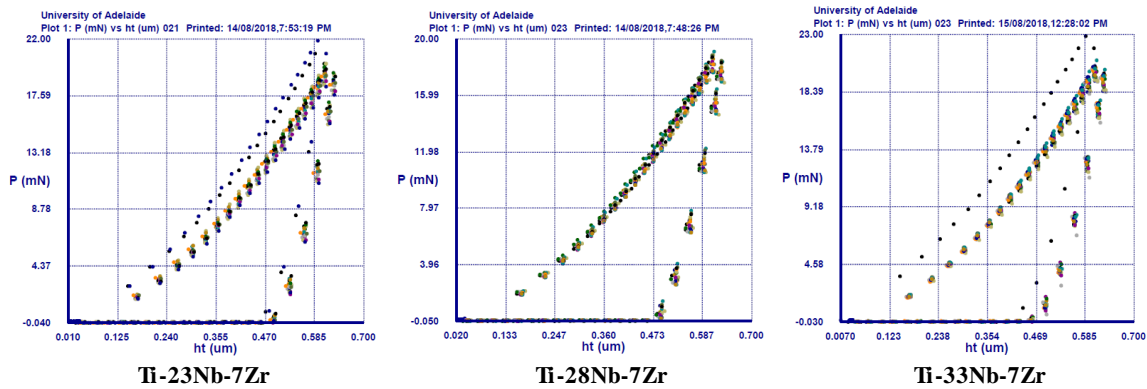


Figure 43: Load-displacement curves for three samples. The curves were plotted through nanoindentation system.

Figure 43 plots the graph of the applied load, P(mN) versus the depth of the penetration ht(μm). The curve with 28%Nb has a narrower range of dispersion of readings. The applied load is lower, around 20mN compared to 23% Nb (22mN) and 33% (23mN). The penetration depths range between 0.627 to 0.629μm.

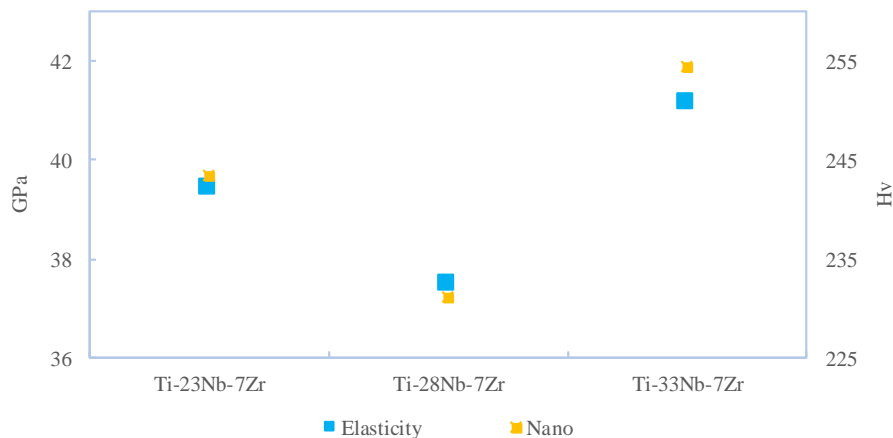


Figure 44: Comparison of Young's Modulus and Nanohardness with increasing of Nb Content %

The comparison of the Young's modulus and Nanohardness with elevating Nb content is illustrated in Figure 44. The hardness has a direct impact in Young's modulus which is proportionally linked. The increment of Nb from 23% to 28% shows a decrease in both nanohardness and Young's modulus which corresponds to the microhardness result. However, the hardness and Young's Modulus was increased while adding the Nb from 28% to 33%, which is conflicting with the trend shown in microhardness results. Shown in Figure 45, microhardness of the samples decreases with the increment of Nb content whereas the nanoindentation results exhibit an inconsistent trend whereby the hardness initially decreases at 28wt% Nb but rises at 33wt% Nb. The discrepancy in the result in terms of the hardness pattern observed is mainly caused by the point of indentation. While microhardness is measuring the

average hardness over the large area, nanoindentation gives a very localized hardness. For example, nanoindentation gives the hardness within the grain, microhardness is the average value of different grains. Furthermore, within the grain itself, there are made up of different phases which produce different hardness. This scenario will be further discussed in section 5.5.

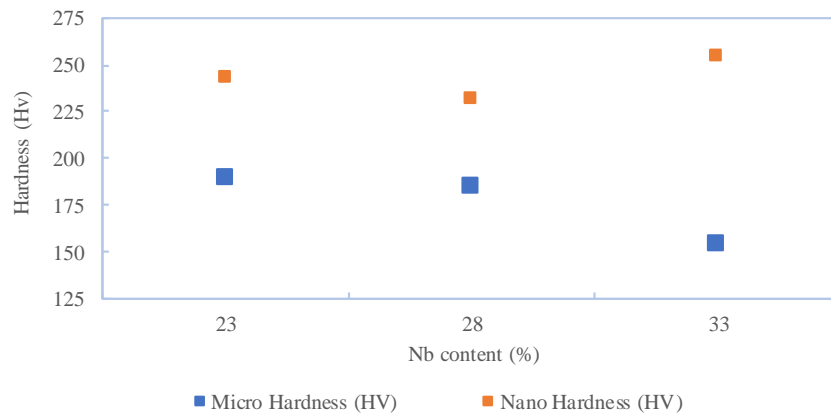


Figure 45: Comparison of hardness in micro and nano scale

4.6 Chemical Composition Results

1) Sample 1 – Ti-23Nb-7Zr

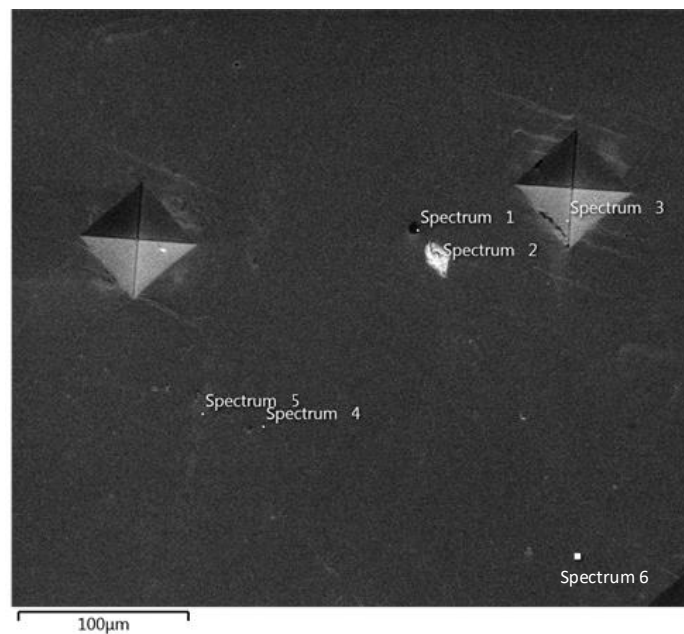


Figure 46: Electron Image for EDS analysis (Ti-23Nb-7Zr)

Table 19: Chemical composition from EDS analysis for Ti-23Nb-7Zr

Spectrum	Ti wt%	Nb wt%	Zr wt%
1	69.0	23.9	7.2
2	69.7	22.9	6.4
3	68.2	24.2	7.6
4	69.8	23.0	7.2
5	70.0	23.0	7.1
6	69.2	23.5	7.3
Average	69.3	23.4	7.1
STDEV	0.66	0.54	0.40

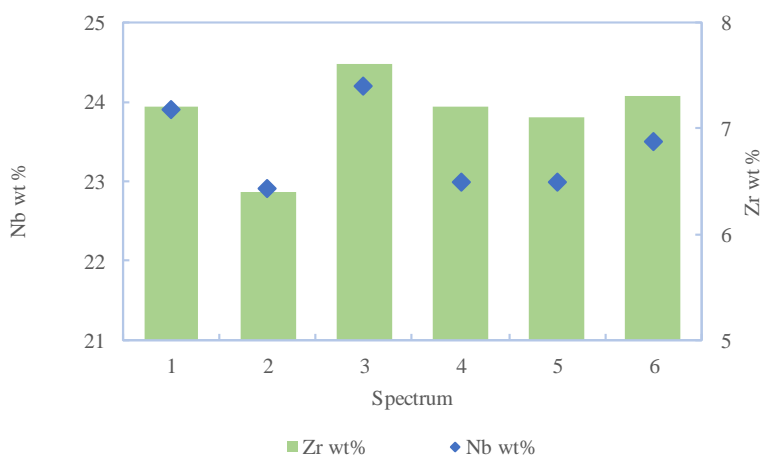


Figure 47: Chemical composition from EDS analysis for Ti-23Nb-7Zr

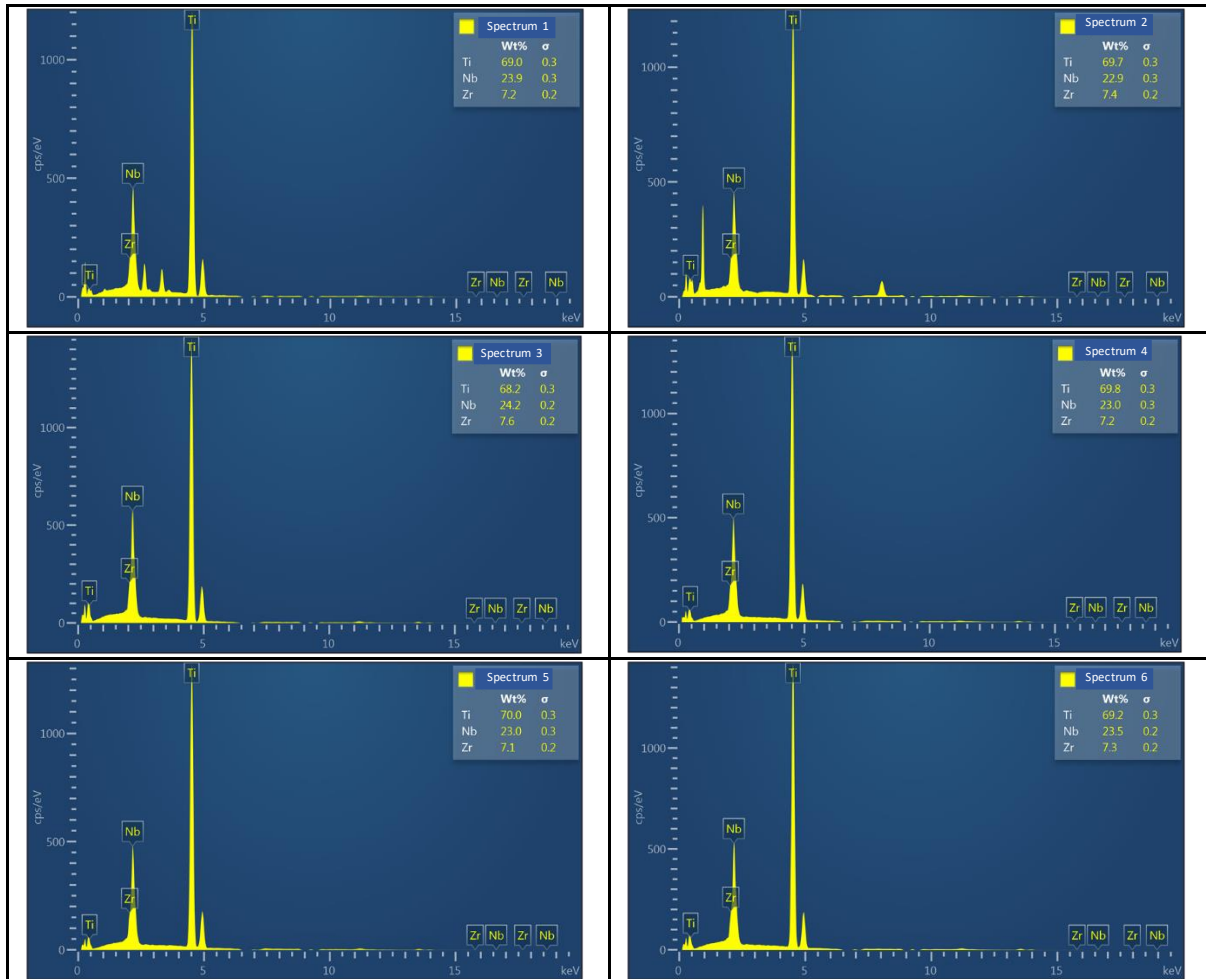


Figure 48: Spectrum analysis from EDS (Ti-23Nb-7Zr)

The Nb content of spectrum 1 and 3 (listed in Table 19) are higher in comparison to other spectrums. Spectrum 1 fall on a black spot under the SEM image which normally hints a possible presence of impurity. The round circumference of the dark pore measures about 5 μ m in diameter. Spectrum 3 was taken from the microhardness indentation at point 4 and the Nb and Zr content are 1.2wt% and 0.6wt% higher respectively than the specified content for the fabrication process. Overall, the compositional weightage for the three elements are very close to the percentage determined in the fabrication by a marginal difference of +1.7% +1.4% for Nb and Zr wt% respectively. The trend of chemical content in Figure 47 shows both Nb and Zr contents are aligned with each other. A higher content of Zr is found with a higher content of Nb and vice versa. The spectrum analysis from EDS was shown in Figure 48.

2) Sample 2 – Ti-28Nb-7Zr

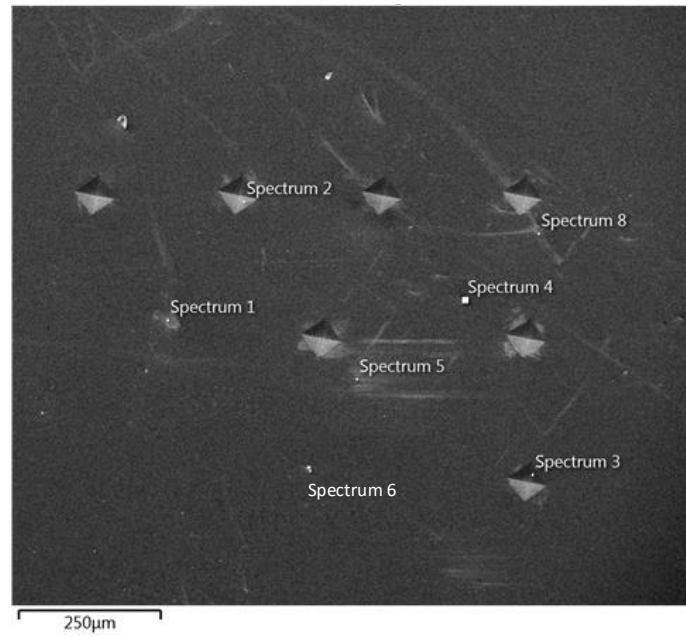


Figure 49: Electron Image for EDS analysis (Ti-28Nb-7Zr)

Table 20: Chemical composition from EDS analysis for Ti-28Nb-7Zr

Spectrum	Ti wt%	Nb wt%	Zr wt%
1	65.4	27.8	6.9
2	64.2	28.5	7.3
3	69.5	24.9	5.6
4	64.8	28.3	6.9
5	64.8	28.3	6.9
6	63.9	29.0	7.1
Average	65.4	27.8	6.8
STDEV	2.06	1.47	0.60

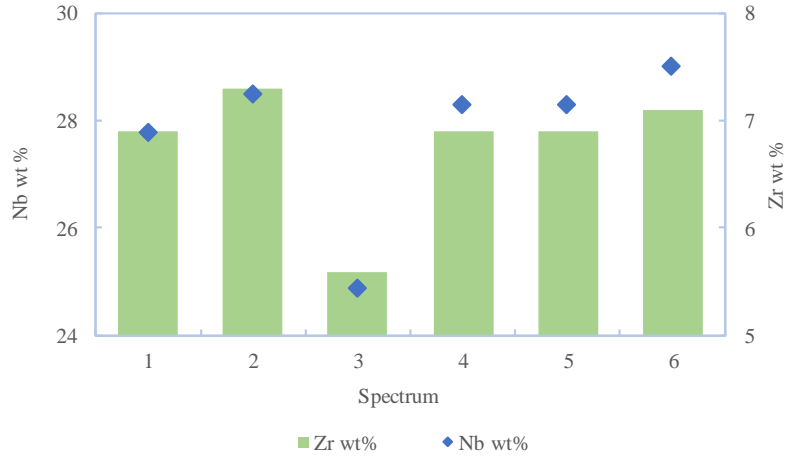


Figure 50: Chemical composition from EDS analysis for Ti-28Nb-7Zr

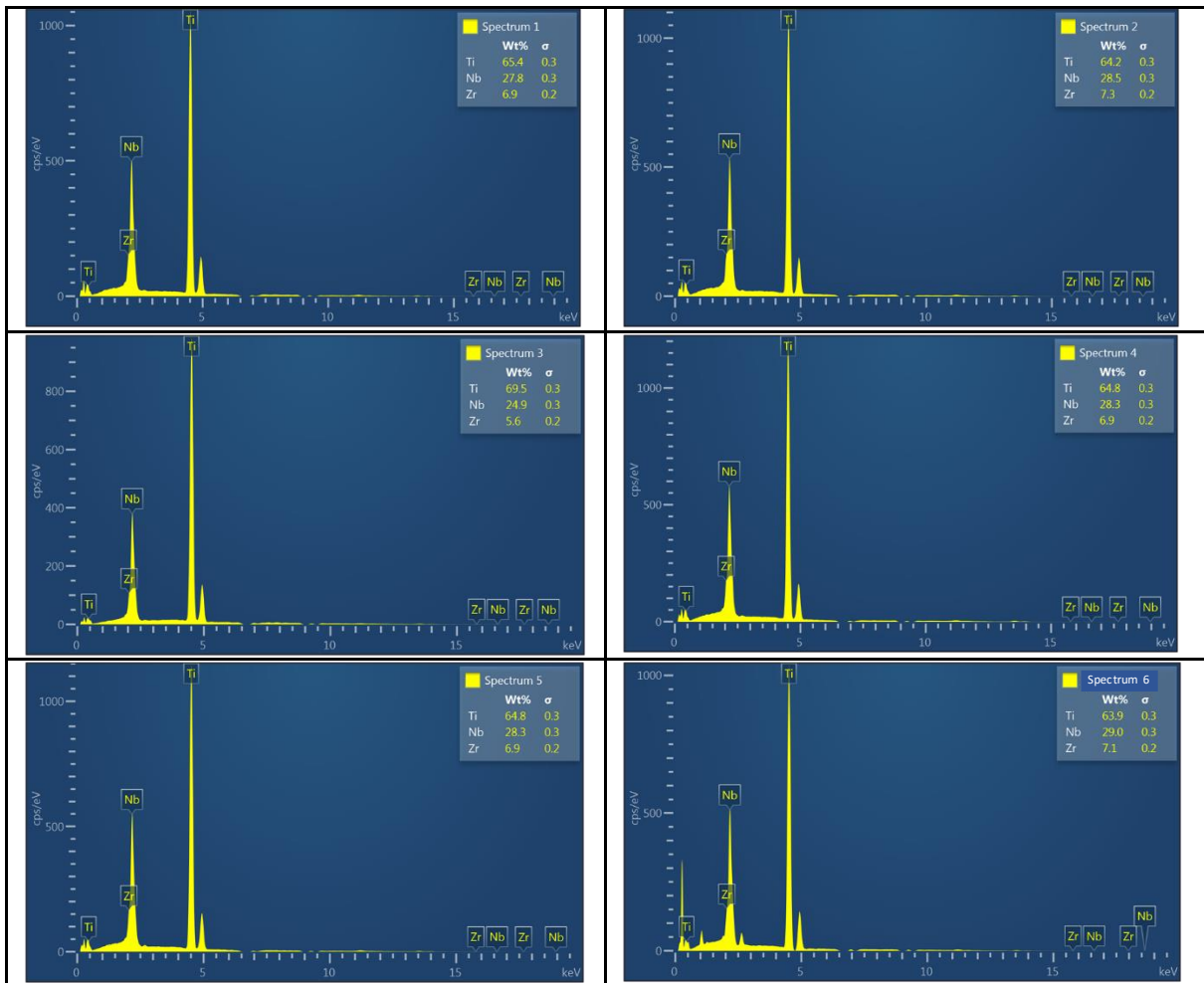


Figure 51: Spectrum analysis from EDS (Ti-28Nb-7Zr)

The average wt% for Nb and Zr in sample 2 (Figure 49) are lower than the specified alloying component determined during the fabrication although they are contained within the acceptable range. The negligible difference of Nb is -0.7% whereby Zr wt% is differ by -2.9%. This significance discrepancy

is due to spectrum 3 which has only 24.9 wt% Nb and 5.6 wt% Zr, since all the other points are closely matched to 28 wt% Nb and 7wt% Zr. Spectrum 3 is taken from the microhardness indentation point 6 as shown in Figure 49. The highest wt% content of Nb and Zr were observed in spectrum 7 and spectrum 2 respectively. The Nb and Zr content in Figure 50 agree with each other whereby both compositions rise and fall simultaneously. The spectrum analysis from EDS was shown in Figure 51.

3) Sample 3 – Ti-33Nb-7Zr

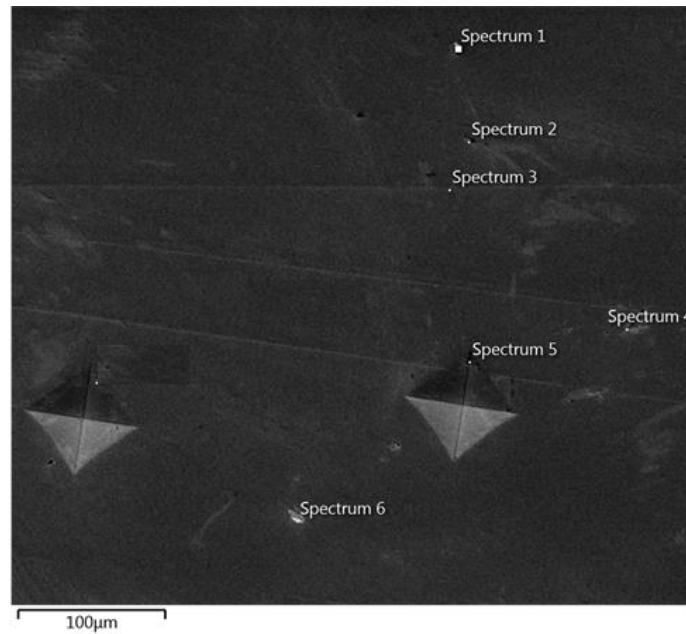


Figure 52: Electron Image for EDS analysis (Ti-33Nb-7Zr)

Table 21: Chemical composition from EDS analysis for Ti-33Nb-7Zr

Spectrum	Ti wt%	Nb wt%	Zr wt%
1	58.2	34.3	7.6
2	59.1	33.6	7.3
3	59.1	34.8	7.1
4	58.4	34.2	7.4
5	64.5	29.3	6.3
6	58.6	33.9	7.4
Average	59.7	33.2	7.2
STDEV	2.40	1.92	0.46

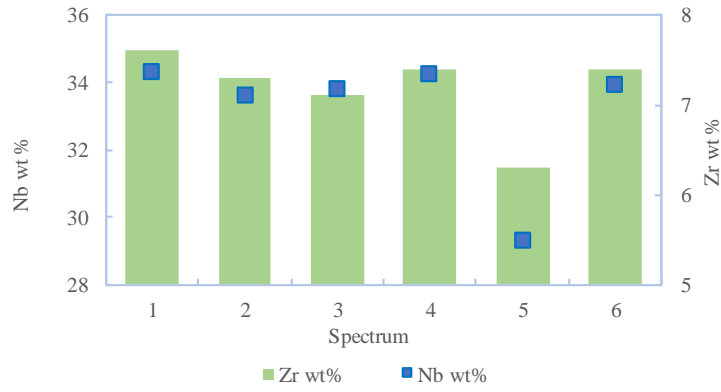


Figure 53: Chemical composition from EDS analysis for Ti-33Nb-7Zr

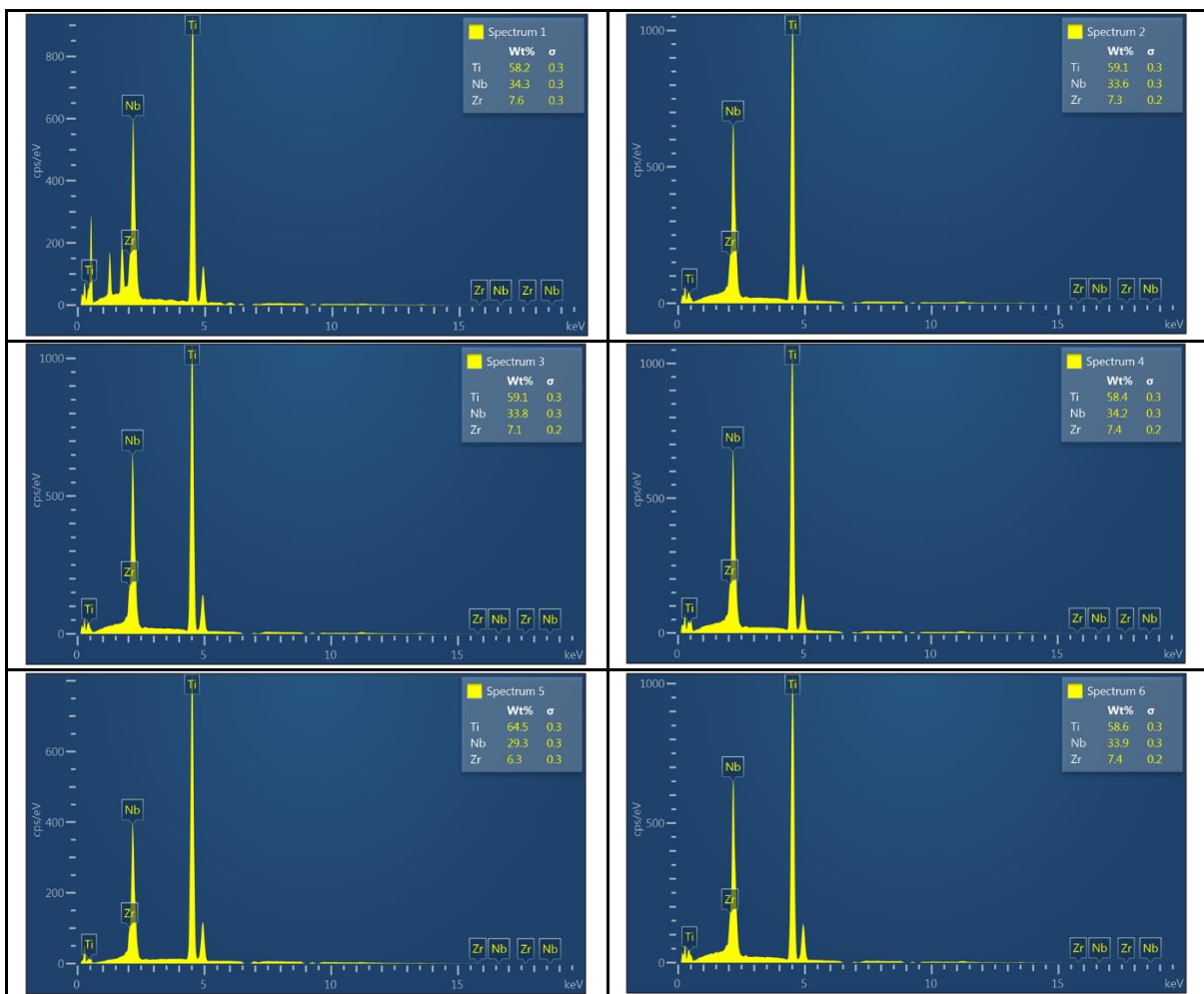


Figure 54: Spectrum analysis from EDS (Ti-33Nb-7Zr)

The same situation is also observed in sample 3 with one of the spectrums, which is spectrum 5, having an exceptional low wt% of both Nb and Zr. Nb content is 3.7wt% lower and Zr 0.7wt% lower. Spectrum 5 is located within the microhardness indentation. The deviation element composition for sample 3 is greater as the Nb wt% range spans between 5.5wt%. The range between the highest and lowest wt% for

Zr is 1.3wt%. Spectrum 3 which measures the line includes of highest content of Nb% whereas spectrum 1 which touches the white mark as displayed in Figure 52. However, the overall alloying element composition result shown in Table 21 is very close to the designed alloy. The Nb content is directly proportional to Zr content as displayed in Figure 53. The spectrum analysis from EDS was shown in Figure 54.

4.7 Homogeneity

The mapping images tabulated in Figure 55 exhibited a uniformly distributed alloying element across the surface of all samples. The colour mapping exhibits a finely-dispersed particles of Ti, Nb and Zr spreading across the surface evenly. No particular space is observed without colour which clearly displays the homogeneity of the samples with regards to an effective fabrication process and solution treatment.

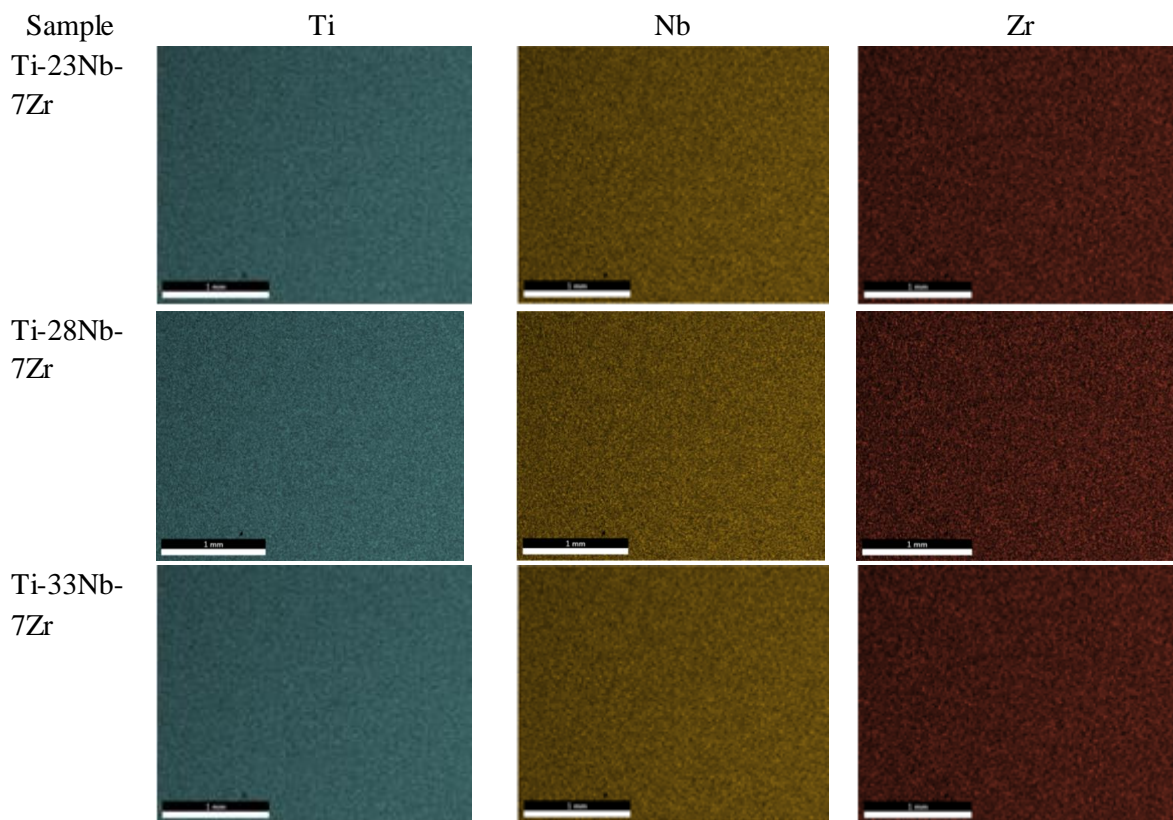


Figure 55: Mapping images of sample alloys via EDS analyser

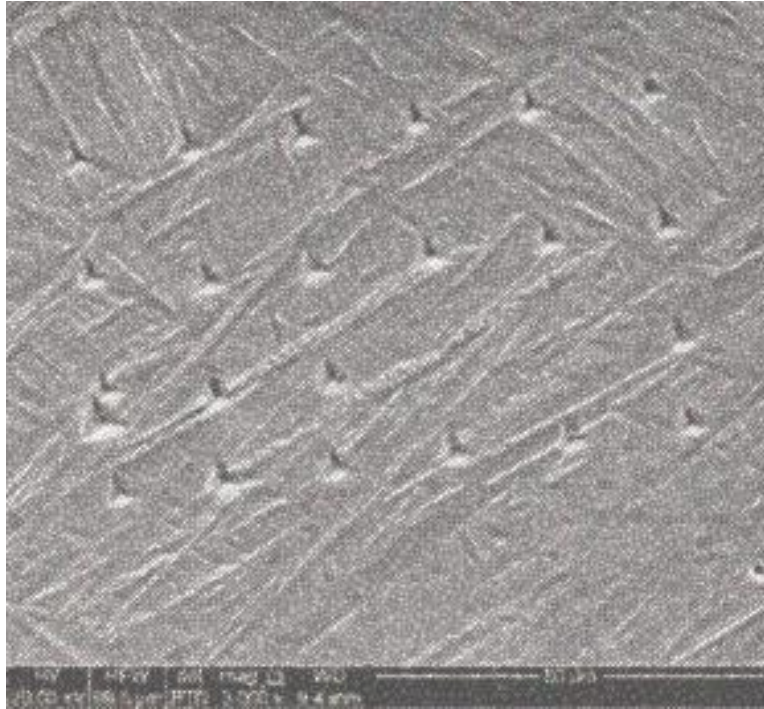
Summary of Chapter 4: Results

In this chapter, the results of microstructural examination, phase composition, elemental analysis and mechanical properties of Ti-Nb-Zr alloys in specified composition are described. The microstructure and phase analysis have shown a structure of $\alpha''+\beta$ in all alloys and they are homogeneous. The microhardness indicates the addition of Nb content tends to lower the hardness. Whereas in

nanohardness, the reading decreases from 23wt% to 28wt% Nb but increases back at 33wt% Nb. All alloys were measured with Young's modulus ranging from 37 to 41GPa.

This page is intentionally left blank

CHAPTER 5



Discussion

- 5.1 Phase Analysis
- 5.2 Microscopy Analysis
- 5.3 XRD Analysis
- 5.4 Microhardness
- 5.5 Nanoindentation
- 5.6 Homogeneity
- 5.7 Etching Process

5.1 Phases Analysis

Martensite is a function of Nb content, a β stabilizing element. The addition of Nb decreases the martensite structure hence decreases the alpha phase volume fraction. The presence of two or more phases in the samples can be explained as according to phase diagram of Ti-alloy as illustrated in Figure 56.

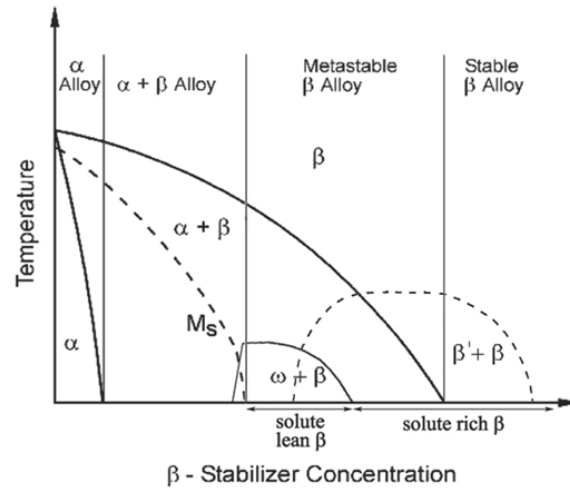


Figure 56: Schematic phase diagram of titanium alloys with the decomposition products of the β -phase¹⁰³

The phase diagram of titanium alloys with β stabiliser shows at zero β stabiliser content there is still a chance of the existence of β phase in the ($\alpha + \beta$) phase field. All three samples retain the beta matrix at room temperature, thus they are termed $\alpha + \beta$ alloy. The heating process transformed the alloy from α to β phase. Then, on cooling from the β -transus temperature, α started to precipitate and grain boundary films of α started to grow (Figure 57). The α phase then grows in Widmanstätten plate from the grain boundary α . The α phase however, did not dissolve into the β solution and instead it stabilised against transformation. All the α plates in a colony will be of the same orientation, often inherited from the grain boundary α . In sample 1, of lower Nb content (β -stabiliser), the α plates grew vigorously to fill the grain, eventually creating a coarser and thicker martensitic structure at a larger quantity. As the Nb content is increased, the development of α is thus inhibited, in compliance with the microstructure exhibited in sample 3 which consisted dominantly of β -phase matrix. Subsequently, the results from the phase diagram (Figure 38) posted that a better solution of Nb and Zr suppresses the alteration of β to α effectively and therefore leads to a stable and steady increase of β phase. When the Nb concentration increases, the α phase slowly diminishes. A more homogeneous microstructure is observed, and this is caused by the high dissolution of niobium in the titanium matrix⁵¹.

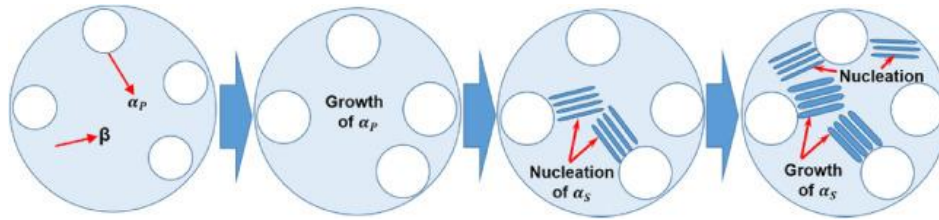


Figure 57: The evolution process of α_p and α_s phases when cooled from a two-phase field in Ti-alloys¹⁰⁴

The phase diagrams in Figure 56 and those produced from Thermo-calc software (Figure 38 and Figure 39) simulate an existence of BCC (β) and HCP (α) phase in the alloy synthesized. However, the XRD analysis (Figure 40) has proven the presence of BCC (β) and orthorhombic (α'') phase instead, which goes in line with the results obtained from the microscopy results from both optical microscope and SEM. Although there is a discrepancy between α and α'' in the results, it is important to remember that Thermo Calc is a prediction of phases in an equilibrium state that shows the phases formed if given sufficient time to transform. In the reality or actual situation, it is essential to factor in various dependents such as cooling rate, heating rate, work hardening process in order to produce the phase desired. α (HCP) is martensite transformed from β (BCC). α'' (orthorhombic) on the other hand is the deformed martensite as a result of quenching or deformation. The quenching process experienced by the samples during then solution treatment had a significant impact on the transformation of the phase which generates the detection of the (orthorhombic) $\alpha'' + \beta$ phase instead of the (HCP) $\alpha + \beta$ phase.

5.2 Microscopy Analysis

Microscopy analysis will be based on results obtained from two sets of equipment which are optical microscope and SEM with EDS analyser.

5.2.1 Optical microscopy

The optical microstructure results disclose that most of the structure inherited the acicular or lamellar alpha which grows from the nucleation of beta matrix crystallographic planes. It is the most common transformed product from β (beta) upon cooling¹⁰⁵. From the optical microscopy, the existence of two phases which are α'' (martensite) and β (beta) is verified. The needle-like structure is formed consequent to the cooling rate. The cooling rate is so fast that the crystals nucleate not only all over the grain boundaries but also in the grain. The immediate nucleation transformed the grains into structure of "longish" needles ("acicular growth", laths) or plates aligned in same preferred direction within one grain¹⁰⁶. According to Pederson 2002, a faster cooling rate favours a more basketweave or Widmanstätten structure¹⁰⁷ which probably provides the reason behind the finding of a high distribution of this structure located near the surface edge. This is also supported by the observation at Figure 31 b) with Widmanstätten structure detected at the edge and acicular martensitic in the centre of the sample. The quantitative metallography reviewed an inconsistency of alpha structure spreading across

multigrain with some grains having a denser martensite. It is believed that the discrepancies content of β -stabilizing elements may have resulted this scenario. A grain composed of higher Nb composition, the β -stabilizer, will inhibit the precipitation of alpha structure hence a relatively smaller amount of martensitic structure is observed. Additionally, some grains contain solely acicular or Widmanstätten structure whereas there are also a number of grains consisting of both structures. Some authors suggested that the basketweave structure is initiated not only from the nucleation and growth directed from the β grain boundaries but also within the β grains¹⁰⁸. Acicular martensite however is nucleated from the grain boundaries and both structures will stop growing when they collided with each other.

The elongated horizontally structure shown in Figure 31 a) is a consequence of effect from the quenching process. When the cooling started from the surface, the nucleation of the dendrite structure and columnar crystals began to grow and extended into the centre of the sample in an inward direction which resulted in the outcome of horizontally elongated structure. Since the cooling rate is slower at the centre of the sample, larger elongated grains at higher concentration are observed in the centre of the sample (Figure 27 a). The comparison of grain size between the 3 samples shows a smaller grain size observed in sample 3, especially surrounding the surface boundary. It is believed that quenching process for sample 3 may have been completed more efficient than the other two samples.

The “pinch off” effect in Figure 31 b) is due to the shear strain involved in the deformation-twinning process, which happens during quenching due to the cooling rate discrepancy between the surface and the centre¹⁰⁹. Increased strain and temperature can affect the shape and size of twinning¹¹⁰. The type of twin structure deformation depends highly on the quenching rate¹¹¹, which is evident in Figure 36 a) where the heavily induced deformed structure is observed near the surface owing to the speedy quenching rate occurs in situ. On the other hand, it has been reported that twinning is beneficial in increasing ductility of alloy, and as a result, the low-cycle fatigue life is improved¹¹².

This acicular microstructure is also effective in increasing toughness due to its chaotic ordering. Acicular alpha is formed in the interior of the grains by direct nucleation from the grain boundaries and within the grain itself, resulting in randomly oriented needles with a basketweave appearance. The basketweave pattern is beneficiary as it acts as interlocking system to resist the crack propagation caused by cleavage within the grain. This function could be further enhanced with finer grain. Acicular ferrite is also known to produce high angle boundaries between the grains. This further reduces the chance of cleavage as these boundaries impede crack propagation. Widmanstätten structure is coarser than acicular structure, developed from cooling prior to high heating temperature but less than critical cooling rate. Widmanstätten structure is characterized by its low impact values and low percentage elongations¹¹³. The static bending strength and nominal fracture toughness decrease with larger martensite needles¹¹⁴. The size and length of needle size decrease from sample 1 to 3, and so is the

hardness. The results confirmed that materials with higher hardness have a lower bending strength and fracture toughness.

5.2.2 Scanning Electron Microscopy

The bright dots spotted in Figure 34 a) are the precipitation of unresolved primary equiaxed alpha in a transformed beta matrix. The ASM handbook suggested that the white region is an indicative of less heat treatment response. Precipitation of alpha during aging of beta results in some darkening of the aged beta structure¹⁰¹.

The mechanism slip band is generated in Figure 34 c) where the dislocations are multiplied with cross slip. This is an occurrence of high quenching rate, whereby the large quenched-in stresses tend to encourage the gliding of dislocations¹¹⁵. Besides slip, the presence of alpha twinning structure was also noticed (both in Figure 31 b and Figure 34 c), an indicative of deformation within the grain subsequent to high quenching rate. It is believed that the fabrication process also contributes to this scenario whereby the ingots were remelted 5 times. The alternating rising and dropping of temperature cause the crystals to start forming and diffusing repeatedly which leads to plane slipping and disarranging. The intermittent nucleation process might also indirectly trigger the deformation. However, the significant factor is due to the immense quenching rate.

Figure 35 shows a series of coarse laths, transformed or developed in the early course of the martensitic transformation. Coarse laths are formed in the earliest stage of the martensitic transformation sequence as suggested by the typical initiation site for martensitic phase transformation, whereby the flat end of the coarse laths is attached to the prior beta grain boundary. This is proven by the observation in Figure 35 d denoting that the lath was initiated from the grain boundaries and grow inward into the grain. Above the M_s temperature, the beta phase is soft and has a low defect density, thus it is vulnerable against the nucleation of martensitic lath. Consequently, the coarse lath regions represent “softer” zones in the martensitic structure. Further down the quenching process, the retained martensitic is progressively hardened by the transformation strain resulted from the reduced temperature and the increasing density of dislocations or shape deformation involved in the martensitic transformation. As the transformation proceeds, these dislocations and deformations cause an increasing resistance to the progressing martensitic transformation and the coarse laths split into thinner laths. Thus, thinner laths are harder than coarse laths owing to its dense deformations¹¹⁶.

The equiaxed pores observed in Figure 35 are developed from the titanium sponge used as raw material in the alloy fabrication. This form of structure is preferable as the pores resemble the spongy structure of cancellous bone which is lighter and less dense. More effectively, this porous structure enhances osseointegration that promotes bone in growth and stability¹¹⁷.

Both optical and SEM microscopy acknowledge the existence of twinning and slip band. Twinning and slip are competitive yet complementary mechanisms for different crystal deformation under various systems and certain parameters or situations. Twinning has a more heterogeneous deformation while slip deformation appears to be more homogeneous. The deformation caused by twinning can lead to fracture along the boundaries. This phenomenon is particularly observed in β transition metals at low temperatures. Of the three common crystalline structures BCC (β), FCC, and HCP (α), the HCP structure is the most likely to form deformation twins due to its arbitrary shape change as well as insufficient amounts of slip systems¹¹⁸.

5.3 XRD Analysis

In the XRD result, it was found that the diffraction peaks move towards low angle direction by increasing the Nb content. The shifting effect is a consequence of the lattice dilation induced by the addition of Nb. The spacing calculation revealed a prodigious lattice dilation through expansion of lattice parameters by increasing Nb. With respect to the unit-cell volume of pure α or β titanium, the unit cell volume for these alloys is increased in accordance to the element content. Another significant benefit through the addition of β stabilizers is related to the lowering of Young's modulus. This is realized by the expansion of unit cell volume which could reduce the bonding force of the lattice⁹⁰.

The peak analysis in Figure 40 c, which is sample 3, exhibits fewer α' peaks compared to the other samples. This phenomenon suggests a lower quantity of martensitic structure is identified in sample 3, which is supported by the evidence from the microscopy results. The XRD profile for sample 3 also displays a noticeably smaller number of periods which is explained by Girgsdies. F, who verified that the smaller the crystal, the smaller the number of periods¹¹⁹. This statement can also be related to Section 4.2.1 whereby it is discussed that sample 3 has the smallest grain size compared to other samples.

However, the intensity of beta peaks in Ti-based alloys such as (200), (211) are reported to be weaker than other alloys due to various consequences from the testing method, secondary phase and microstructure texture subjected to treatments involved^{120,121,122}. Overall, the XRD analysis of the samples gave a combination of beta phase, α' martensite phase, and very limited omega phase (sample 2). However, the intensity peaks were not able to provide a clarity on the constitution of each phase.

5.4 Microhardness

The results from the microhardness indicated that Ti-23Nb-7Zr is the hardest among all samples. This phenomenon also clearly exhibits a relationship between the surface morphology and the surface hardness. The significant content of Nb in sample 3 has contributed to the stability of beta matrix in the structure with the finding of the highest volume of beta phase. The formation of the alpha phase is prohibited by the β stabilizing element as the results show a decreasing of martensite structure with

increasing Nb content¹²³. Therefore, the addition of Nb, a β -stabiliser brings an effective implication in lowering the Vickers hardness, as it inhibits the transformation of martensitic structure that has potential in hardening the alloys. While a higher density of martensite increases the hardness of the sample, the greater proportion of beta matrix actually offers a lower hardness.

5.5 Nanoindentation

The hardness measured exhibits a difference in the micro and nano scales, especially for sample 3. Microhardness results show a decreasing trend of hardness from sample 1 to 3 due to the amount of martensitic α' phase in the microstructure. In contrast, the nanohardness results obtained for sample 3 is greatest among all samples.

The statement provided by both microhardness and nanohardness can be verified through various factors. Firstly, the derivation of hardness value. The formula derived for hardness and Young's modulus measured from nanoindentation are as in Equation 1 and Equation 2¹²⁴.

$$H_{rr} = \frac{F_{max}}{A_p(h_c)}$$

Equation 1

$$E_r = \frac{\sqrt{\pi}}{2C\sqrt{A_p(h_c)}}$$

Equation 2

H_{rr} is the indentation hardness, F_{max} is the maximum test force and $A_p(h_c)$ is the projected area of contact of the indenter evaluated at a depth of h_c , E_r is the reduced modulus of indentation contact, and C is the compliance of contact. The simplification of the formula explained that at maximum force, the projected area of contact will determine the value of hardness. Thus, a bigger contact area will project a softer value in hardness hence a lower Young's modulus. This configuration strongly agrees with the microhardness results in which the smaller indentation (contact area) reads a higher hardness value.

The opposing statement achieved in nanoindentation could be speculated by the surface or points of measurement. Figure 58 shows the nanoindentation surface of the samples. As displayed in sample 1, some of the indentation fall on the acicular martensitic structure owing to its higher concentration of α' phase. In sample 2, most of the measurements were directed on the beta matrix which is of softer compound compared to the martensitic structure. Although sample 3 has a wider coverage of beta matrix, its lath martensite is thinner due to β -stabiliser that prohibited the growth or widening of martensite. As rectified previously, a thinner lath is harder than a coarse lath because the coarse lath is formed during the early stage of martensitic transformation, close to the M_s temperature where β (softer) has just started to transform. The thin lath is the finished product of the martensitic transformation that contain greater dislocation thus is harder. It is believed that the indentation conducted for sample 3 was actually measuring the laths instead of the matrix, which eventually gives the highest nanohardness

value in the test. Microhardness has measured a reasonably broader area with a combination of martensitic embedded in the β matrix. Thus, its reading is reasonably acceptable.

Another point to be considered is the grain size of the samples. Hardness increases with decreasing particle size, which explains the finding obtained in nanoindentation with sample 3 of smallest grain size having the highest hardness. Small grains also improve the overall strength of the sample as they increase the slip bands and the grain boundaries act as an obstacle for crack propagation.

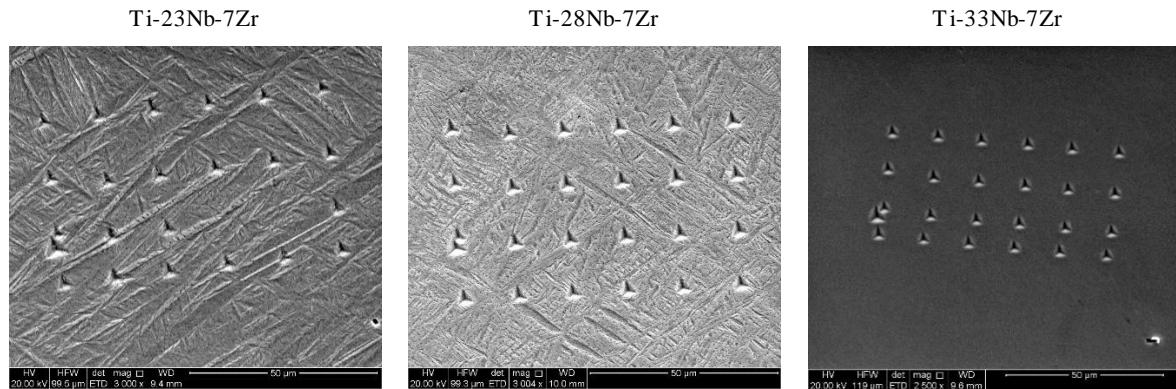


Figure 58: Microstructure of the nanoindentation

Although all samples are of $\alpha''+\beta$ phases, the amount of orthorhombic martensitic structure in sample 1 is considerably greater than all other samples and the platelike structure is coarsest in size. Whereas, a modest quantity of martensite is observed in sample 3 associated with finer platelike structure, which consequently attributes to denser proportion of beta matrix that gives lower hardness. The microstructure results are correlated to microhardness outcome.

Furthermore, it could be anticipated that sample 3 has less pores as the spongy structure of Ti is 10 wt% less than sample 1 and 5 wt% less than sample 2. A porous surface morphology on a material implies a depreciation in hardness due to lack of atomic bonding on the surface that could inhibit plastic deformation. In addition, the result depends very much on the surface purity and contamination of the materials as any fine particles adhered to the surface may either slightly or significantly increase or decrease the surface hardness. There is also a possibility that the residual stresses present after the quenching process could contribute to the enhancement of hardness¹²⁵.

The nanohardness magnitude for samples 1 and 2 is about 28% and 25% higher than the microhardness. In an experimental work reported by Qian,L, et al., 2005, the authors concluded that nano-indentation hardness is about 10–30% magnitudes larger than the microhardness of the same measured materials. The main reason can be explained by the analysis of the nano-indentation hardness which uses the projected contact area at peak load instead of the residual projected area used in microhardness measurement. As the projected contact area at peak load is always smaller than the residual projected area, the nanohardness is thus always larger than microhardness¹²⁶.

Nanoindentation is basically gaining its popularity over the last 20 years, where researchers have been looking into the mechanical properties at nanoscale, as their properties literally differ from the bulk properties mainly due to surface effect¹²⁷. Nanoindentation is more widely used in measuring thin films and microelectromechanical systems (MEMS)¹²⁸. In terms of reliability between microhardness and nanoindentation tester, both have their specific applications and they are actually complementing each other in a unique way. Microhardness is used to measure the bulk properties of a material, while nanoindentation is used to study the nano properties of the material.

5.6 Homogeneity

The element composition result from EDS analyser has proven a compatible alloying weightage specified and an effective fabrication process conducted. The variation of element composition for sample 1 is very much narrow in range compared to sample 2 while sample 3 displays the widest span of range (STDEV in Table 19, Table 20 and Table 21). The homogeneity of the element composition across the surface is subject to the incremental alloying element. Thus, a higher percentage of alloying element tends to challenge the uniform distribution of the chemical across. The results obtained from the microhardness were either containing the highest or lowest alloying element which propose that the alloying elements are either being exposed or submerged after the mechanical deformation. However, the overall homogeneity level for all samples are acceptable and reasonably good. More importantly, all regions identified had shown an uniformly dispersed Ti(NbZr) solid solution. No unmelted Ti, Nb or Zr particles were traced even though these elements display very different melting point, especially Nb of highest melting temperature. The diffusion of the alloying elements into Ti was well combined due to the fabrication process that involved 5 times remelting process and homogenization at 950°C for 1 hour.

5.7 Etching Process

The etched crystal structure of sample 3 is difficult to be distinguished under optical microscope as insufficient sharp contrasts were detected. Greyish images instead of distinctive black and white were captured. Most of the images were not as explicit as sample 1 and sample 2. Vague grain boundaries incorporated with indistinct martensitic structure suggesting insufficient etching effect. The average etching time for all samples were about 60 seconds. However, the phenomenon only persisted for sample 3 indicating a desirable possibility that sample 3 may have better corrosion resistant. The formation of the gaseous by-products through the chemical reaction between the etchant and the exposed surfaces for all samples were noticed of different rate with sample 3 requiring extended seconds to start the bubbling process.

Summary of Chapter 5: Discussion

This chapter discusses the findings of the results obtained from Chapter 4. Both optical and scanning electron microscopy features the existence of α'' embedded in beta matrix which was transformed from the fabrication process. In addition, slip band and twinning structures were also observed and they were formed during the quenching process. Both mechanisms were most noticeable near the grain boundaries. XRD analysis had confirmed the presence of α'' and β phases through the peaks. The intensity of β peaks are stronger than most of the α'' peaks. The martensite lath is coarser in sample 1 while sample 3 has the finest lath. And the proportion of beta matrix is largest in sample 3. The microhardness of sample 1 is highest which indicates the addition of Nb gives more effective implication in lowering the Vickers hardness. In nanohardness, sample 3 was measured with highest hardness. The discrepancy in the results between micro and nanohardness can be speculated through the point of indentation. While microhardness is measuring the average hardness of grains, nanoindentation only focus on a localised area. Microhardness can measure the lamella structure of $\alpha''+\beta$ at the same time, but nanohardness may only concentrate on either the martensite lath, beta matrix or even the pores.

This page is intentionally left blank

CHAPTER 6



Conclusions

- 6.1 Concluding Remarks
- 6.2 Suggestions for Future Work

6.1 Concluding Remarks

This study investigated the effects of the alloying element in lowering the Young's modulus of Ti-Nb-Zr alloys and to develop a new content of Nb and Zr that offers the Young's modulus of less than 50GPa. To realise the challenge, a course of investigation methods and experiments was sequentially conducted such as literature review, research on the fabrication process, microstructure characterisation and alloys assessment. Thermo calc was employed to predict the phase transformed prior to designing the alloy. The alloy was designed after a thorough research in multi-discipline fields and justification. Essential areas that were highlighted were the study of different phase, especially α , α' and β phases; the microscopy observation to compare the effect and alteration of phase, microstructure, hardness and Young's modulus through the increment of Nb element.

Two phases were predicted through Thermo calc software. Due to the software limitation which only applies for alloys in equilibrium state, the changes of the phase due to deformation or other application were not factored in. However, the results obtained from Thermo calc software were almost similar to the XRD results, provided that distortion happened during the sample actual fabrication process. Microscopy results have further proven the findings of Thermo Calc and XRD by showing the same phases and microstructure identified ($\alpha'+\beta$) through different analysing techniques. The hardness measurements for both micro and nano scales had shown a competent outcome. The Young's modulus result showed that the alloys offer a reduced level of Young's modulus 39.7, 37.5 and 41.7GPa respectively which are all less than the target of maximum 50 GPa. All testings had been effectively completed according to the plan.

In conclusion, the three new generation Ti alloys (Ti-23Nb-7Zr, Ti-28Nb-7Zr and Ti-33Nb-7Zr) were successfully designed and fabricated using casting. The experimental work showed that these alloys with new composition of alloying elements has achieved Young's modulus below 50GPa and have shown a good performance in alloying assessment and microstructure characterization. The objectives aimed for this thesis have all been fulfilled.

6.2 Suggestions for Future Work

This research may be further extended, primarily the validation of these new alloys in the biomedical aspects. Biocompatibility tests such as cell culture or toxicity test are vital since the designed alloy is meant to be implanted *in vivo*. Besides, the corrosion resistance of these alloys should also be identified to be considered applicable *in vivo*.

Electron backscatter diffraction (EBSD) technique through SEM could also be used to study the microstructural-crystallographic characterisation of the alloys. This technique involves the understanding of structure, crystal orientation and phase of materials which is very beneficial as the information available in this field is very limited and insufficient. Additionally, the determination of the constitution of various phases in a sample is most encouraged to confirm its implication on the mechanical properties of the alloys.

The essential mechanical properties such as surface tribology, fatigue test, compression and tensile test are necessary for orthopaedic implants application. These implants are targeted to restore the functionality and mobility of bones to enable patients to return to their normal activities. Our daily activities involve lots of movement that will induce friction, compression, tension, and twisting on the implants. Besides, the continuous cyclic movement from the activities will gradually increase the fatigue failure. Therefore, by having the data/results from the mentioned mechanical tests, it is believed that the properties of the alloys can be further explored and improved thus the prospects of this alloy could be uplifted.

7.0 References

- ¹ The CALPHAD methodology, Sweden, viewed 13 May 2018. <http://www.thermocalc.com/products-services/databases/the-calphad-methodology/>.
- ² Gallivan MD 2014, Institute of Santa Barbara, California, viewed 16 Feb 2018, <http://gallivanmd.com/technology/hip_implants.php>.
- ³ Patty Grace 2015, Hip Replacements Soar Among Young Adults, Linked In, viewed 16 Feb 2018, <<https://www.linkedin.com/pulse/hip-replacements-soar-among-younger-adults-patricia-grace>>.
- ⁴ Nicki Bourlioufas 2016, Orthopaedic joint replacement surgery rates jump in developed nation as populations age, Australian Society of Orthopaedic Surgeons (ASOS) 2018, viewed 17 Feb 2018, <<https://www.asos.org.au/orthopedic-surgery-rates-jump-in-developed-nation-as-populations-age.html>>.
- ⁵ Australian Institute of Health and Welfare 2018, reports and statistics older people, Australia, viewed 17 Feb 2018, <<https://www.aihw.gov.au/reports-statistics/population-groups/older-people/overview>>.
- ⁶ Joon Park & RS Lakes 2007, *Biomaterials, An Introduction*, 3rd edition, Springer Science+Business Media, LLC, New York.
- ⁷ Basketter DA1, Angelini G, Ingber A, Kern PS, Menné T 2003, 'Nickel, chromium and cobalt in consumer products: revisiting safe levels in the new millennium', *Contact Dermatitis*, vol. 49(1), pp. 1-7.
- ⁸ Basketter DA1, Briatico-Vangosa G, Kaestner W, Lally C, Bontinck WJ 1993, 'Nickel, cobalt and chromium in consumer products: a role in allergic contact dermatitis?', *Contact Dermatitis*, vol. 28(1), pp. 15-25.
- ⁹ Joon Park & RS Lakes 2007, *Biomaterials, An Introduction*, 3rd edition, Springer Science+Business Media, LLC, New York, pp. 102.
- ¹⁰ ASM Aerospace Specification Metals, Inc 2018, AISI type 316L stainless steel, viewed 18 Feb 2018, <<http://asm.matweb.com/search/SpecificMaterial.asp?bassnum=MQ316Q>>.
- ¹¹ Joon Park & RS Lakes 2007, *Biomaterials, An Introduction*, 3rd edition, Springer Science+Business Media, LLC, New York, pp. 104-105.
- ¹² Joseph R. Davis 2010, *Nickel, Cobalt, and Their Alloys*, ASM International - Technology & Engineering, pp. 369.
- ¹³ M Niinomi, M Nakai, J Hieda 2012, 'Development of new metallic alloys for biomedical applications', *Acta Biomaterialia*, vol. 8, pp. 3888-3903.
- ¹⁴ Joon Park & RS Lakes 2007, *Biomaterials, An Introduction*, 3rd edition, Springer Science+Business Media, LLC, New York, pp. 109.
- ¹⁵ Domingo J. 2002, 'Vanadium and tungsten derivatives as antidiabetic agents', *Biol Trace Elem Res*, vol. 88, pp.97-112.
- ¹⁶ Boyce B, Byars J, McWilliams S, Mocan M, Elder H, Boyle I, et al 1992, 'Histological and electron microprobe studies of mineralization in aluminum-related osteomalacia', *Br Med J*, vol. 45, pp. 502-8.
- ¹⁷ Joon Park & RS Lakes 2007, *Biomaterials, An Introduction*, 3rd edition, Springer Science+Business Media, LLC, New York, pp. 111.
- ¹⁸ M Niinomi, M Nakai, J Hieda 2012, 'Development of new metallic alloys for biomedical applications', *Acta Biomaterialia*, vol. 8, pp. 3888.
- ¹⁹ Jonathan Black 2006, *Biological Performance of Materials: Fundamentals of Biocompatibility*, Fourth Edition, CRC Press, London.
- ²⁰ Egon Perilli 2017, 'Biomaterials, hard tissue', lecture notes distributed in the topic ENGR7702 Biomaterials, Medical Device Research Institute, Flinders University, Bedford Park, 18 October.
- ²¹ Egon Perilli 2017, 'Biomaterials, hard tissue', lecture notes distributed in the topic ENGR7702 Biomaterials, Medical Device Research Institute, Flinders University, Bedford Park, 18 October.
- ²² Black J, Hastings GW 1998, *Handbook of biomaterials properties*, Chapman and Hall, London UK.
- ²³ Yuhua Li, Chao Yang, Haidong Zhao, Shengguan Qu, Xiaoqiang Li and Yuanyuan Li 2014, 'New Developments of Ti-Based Alloys for Biomedical Applications', *Materials*, vol. 7, pp. 1709-1800.
- ²⁴ Sumner DR, Turner TM, Igloria R, Urban RM, Galante JO 1998, 'Functional adaptation and ingrowth of bone vary as a function of hip implant stiffness', *J Biomech*, vol.31, pp. 909-917.
- ²⁵ Egon Perilli 2017, 'Biomaterials, hard tissue', lecture notes distributed in the topic ENGR7702 Biomaterials, Medical Device Research Institute, Flinders University, Bedford Park, 18 October.
- ²⁶ Huiskes R 1990, 'The various stress patterns of press-fit, ingrown, and cemented femoral stems', *Clin Orthop Relat Res*, vol. 261, pp.27-38.
- ²⁷ Egon Perilli 2017, 'Biomaterials, hard tissue', lecture notes distributed in the topic ENGR7702 Biomaterials, Medical Device Research Institute, Flinders University, Bedford Park, 18 October.
- ²⁸ Niinomi M, Hattori T, Morikawa K, Kasuga T, Suzuki A, Fukui H, et al. 2002, 'Development of low rigidity β -type titanium alloy for biomedical applications', *Mater Trans*, vol. 43, pp. 2970-7.
- ²⁹ Williams DF 2008, 'On the mechanisms of biocompatibility', *Biomaterials*, vol. 29, pp. 2941-53.
- ³⁰ M. Geetha, A.K. Singh, R. Asokamani, A.K. Gogi 2009, 'Ti based biomaterials, the ultimate choice for orthopaedic implants – A review', *Progress in Materials Science*, vol. 54, pp. 397-425.
- ³¹ Egon Perilli 2017, 'Biomaterials, hard tissue', lecture notes distributed in the topic ENGR7702 Biomaterials, Medical Device Research Institute, Flinders University, Bedford Park, 18 October.
- ³² Arne Biesiekierski, James Wang, Mohamed Abdel-Hady Gepreel, Cuie Wen 2012, 'A new look at biomedical Ti-based shape memory alloys', *Acta Biomaterialia*, vol. 8, pp. 1661-1669.
- ³³ Hallab NJ, Anderson S, Stafford T, Glant T, Jacobs JJ 2005, 'Lymphocyte responses in patients with total hip arthroplasty', *J Orthop Res*, vol. 23(2), pp. 384-91.
- ³⁴ Dikici B., Esen Z., Duygulu O., Gungor S. 2015, Corrosion of Metallic Biomaterials. In: Niinomi M., Narushima T., Nakai M. (eds) *Advances in Metallic Biomaterials*. Springer Series in Biomaterials Science and Engineering, vol 3. Springer, Berlin, Heidelberg.
- ³⁵ Mudali KU, Sridhar TM, Raj B 2003, 'Corrosion of bio implants', *Sadhana*, vol. 28, pp.601-637.
- ³⁶ Niinomi M 2002, 'Recent metallic materials for biomedical applications', *Metall Mater Trans A*, vol. 33, pp 477-86.
- ³⁷ M Niinomi, M Nakai, J Hieda 2012, 'Development of new metallic alloys for biomedical applications', *Acta Biomaterialia*, vol. 8, pp. 3888-3903.
- ³⁸ Y Li, C Yang, H Zhao, S Qu, X Li and Y Li 2014, 'New Developments of Ti-Based Alloys for Biomedical Applications', *Materials*, vol. 7, pp. 1709-1800.
- ³⁹ Ilona Hoffmann 2014, 'Magnesium-titanium alloys for biomedical applications', PhD thesis, University of Kentucky, Lexington, Kentucky, USA.
- ⁴⁰ Amir Mahyar Khorasani, Moshe Goldberg, Egan H. Doeven, Guy Littlefair 2015, 'Titanium in Biomedical Applications - Properties and Fabrication: a Review', *Journal of Biomaterials and Tissue Engineering*, vol. 5, pp. 593-619.

- ⁴¹ Mitsuo Niinomi, Yi Liu, Masaki Nakai, Huihong Liu and Hua Li 2016, 'Biomedical titanium alloys with Young's moduli close to that of cortical bone', *Regenerative Biomaterials*, pp. 173–185.
- ⁴² Amir Mahyar Khorasani, Moshe Goldberg, Egan H. Doeven, Guy Littlefair 2015, 'Titanium in Biomedical Applications - Properties and Fabrication: A Review', *Journal of Biomaterials and Tissue Engineering*, vol. 5, pp. 593–619.
- ⁴³ Appel F, Oehring M, Paul J, Klinkenberg C, Carneiro T 2004, 'Physical aspects of hot-working gamma-based titanium aluminides', *Intermetallics*, vol.12, pp. 791-802.
- ⁴⁴ Polmear I 2005, 'Light alloys: from traditional alloys to nanocrystals', Butterworth-Heinemann.
- ⁴⁵ Zhao S P, Lv S K and Hao W J 2003, 'Titanium Alloys and Surface Modification', Harbin: Harbin Institute of Technology Press.
- ⁴⁶ Kim HY, Kim JI, Inamura T, Hosoda H, Miyazaki S 2006, 'Effect of thermo-mechanical treatment on mechanical properties and shape memory behavior of Ti-(26-28) at.% Nb alloys', *Mater Sci Eng A*, vol. 438, pp.839-43.
- ⁴⁷ Williams JC, Hickman BS, Marcus HL 1971, 'The effect of omega phase on the mechanical properties of titanium alloys', *Metall Trans*, vol. 2, pp. 1913-9.
- ⁴⁸ Pio John S. Buenconsejo, Hee Young Kim, Hideki Hosoda, Shuichi Miyazaki 2009, 'Shape memory behavior of Ti–Ta and its potential as a high-temperature shape memory alloy', *Acta Materialia*, vol. 57, pp. 1068–1077.
- ⁴⁹ Hickman BS 1969, 'Omega phase precipitation in alloys of titanium with transition metals', *Trans Metall Soc AIME*, vol.245, pp.1329-36.
- ⁵⁰ Nakai M, Niinomi M, Oneda T 2012, 'Improvement in fatigue strength of biomedical β -type Ti–Nb–Ta–Zr alloy while maintaining low Young's modulus through optimizing α -phase precipitation', *Metall Mater Trans A*, vol. 43, pp.294–302.
- ⁵¹ X Rao, CL Chun, YY Zheng 2014, 'Phase composition, microstructure, and mechanical properties of porous Ti–Nb–Zr alloys prepared by a two-step foaming powder metallurgy method', *Journal of Mechanical Behaviour Biomedical Materials*, vol. 37, pp. 27-36.
- ⁵² Motyka, M., Baran-Sadleja, A., Sieniawski, J., Wierzbinska, M. and Gancarczyk, K., 2018. Decomposition of deformed α' (a'') martensitic phase in Ti–6Al–4V alloy. *Materials Science and Technology*, pp.1-13.
- ⁵³ Pang, E.L., Pickering, E.J., Baik, S.I., Seidman, D.N. and Jones, N.G., 2018. The effect of zirconium on the omega phase in Ti-24Nb-[0–8] Zr (at.%) alloys. *Acta Materialia*, 153, pp.62-70.
- ⁵⁴ Yang, J., Yu, H., Yin, J., Gao, M., Wang, Z. and Zeng, X., 2016. Formation and control of martensite in Ti–6Al–4V alloy produced by selective laser melting. *Materials & Design*, 108, pp.308-318.
- ⁵⁵ Yang, J., Yu, H., Yin, J., Gao, M., Wang, Z. and Zeng, X., 2016. Formation and control of martensite in Ti–6Al–4V alloy produced by selective laser melting. *Materials & Design*, 108, pp.308-318.
- ⁵⁶ Xing Wang, Ligang Zhang, Ziyi Guo, Yun Jiang, Xiaoma Tao, Libin Liu 2016, 'Study of low-modulus biomedical β Ti–Nb–Zr alloys based on single-crystal elastic constants modeling' *Journal of the mechanical behaviour of biomedical materials*, vol. 2, pp. 310-318.
- ⁵⁷ Li Y, Xiong J, Wong C, Hodgson P, Wen C. 2009, 'Ti6Ta4Sn alloy and subsequent scaffolding for bone tissue engineering', *Tissue Eng A*, vol. 15, no. 10.
- ⁵⁸ Donachie M. 2000, *Titanium: A technical guide*, 2nd ed, Materials Park, OH: ASM International, USA.
- ⁵⁹ YL Zhou, M Niinomi 2008, 'Microstructures and mechanical properties of Ti–50 mass% Ta alloy for biomedical applications', *Journal of Alloys and Compounds*, vol. 466, pp. 535-542.
- ⁶⁰ William D. Callister, Jr. 2007, *Materials Science and Engineering – An Introduction*, 7th edn, 1. William D. Callister, J., *Materials Science and Engineering – An Introduction*. 7th ed. 2007, USA: John Wiley & Sons, Inc., USA.
- ⁶¹ Metalary 2018, viewed 05-March, <https://www.metalary.com/titanium-price/>
- ⁶² M Niinomi, M Nakai, J Hieda 2012, 'Development of new metallic alloys for biomedical applications', *Acta Biomaterialia*, vol. 8, pp.3888-3903.
- ⁶³ Congqin Ning, Dongyan Ding, Kerong Dai, Wanyin Zhai, Lei Chen 2010, 'The effect of Zr content on the microstructure, mechanical properties and cell attachment of Ti–35Nb–xZr alloys', *Biomed. Mater.*, vol. 5 045006.
- ⁶⁴ Rajamallu Karre, Manish K. Niranjana, Suhash R. Dey 2015, 'First principles theoretical investigations of low Young's modulus beta Ti–Nb and Ti–Nb–Zr alloys compositions for biomedical applications', *Materials Science and Engineering*, vol. 50, pp. 52–58.
- ⁶⁵ X. Rao, C.L.Chun, Y.Y.Zheng 2013, 'Phase composition, microstructure, and mechanical properties of porous Ti–Nb–Zr alloys prepared by a two-step foaming powder metallurgy method', *Journal of the mechanical behaviour of biomaterials*, vol. 34, pp. 27-36.
- ⁶⁶ Rajamallu K, Manish K Niranjana, Kei Ameyama and Suhash R Dey 2017, 'Phase stability and elastic properties of β Ti–Nb–X (X = Zr, Sn) alloys: an ab initio density functional Study', *Modelling Simul. Mater. Sci. Eng.*, vol. 25.
- ⁶⁷ Tokunaga, T., Matsumoto, S., Ohtani, H. and Hasebe, M., 2007. Thermodynamic calculation of phase equilibria in the Nb–Ni–Ti–Zr quaternary system. *Materials transactions*, 48(2), pp.89-96.
- ⁶⁸ Gasik, M.M. and Yu, H., 2009. Phase Equilibria and Thermal Behavior of the Biomedical Ti–Nb–Zr Alloy. na.
- ⁶⁹ Niobium-Titanium-Zirconium Ternary Alloy Phase Diagram (based on 1961 Mikheev V.S.)
- ⁷⁰ Kumar, K.H., Wollants, P. and Delaey, L., 1994. Thermodynamic calculation of Nb–Ti–V phase diagram. *Calphad*, 18(1), pp.71-79.
- ⁷¹ Tokunaga, T., Matsumoto, S., Ohtani, H. and Hasebe, M., 2007. Thermodynamic analysis of the phase equilibria in the Nb–Ni–Zr system. *Materials transactions*, 48(9), pp.2263-2271.
- ⁷² Y Li, C Yang, H Zhao, S Qu, X Li and Y Li 2014, 'New Developments of Ti-Based Alloys for Biomedical Applications', *Materials*, vol. 7, pp. 1709-1800.
- ⁷³ YL Zhou, M Niinomi 2008, 'Microstructures and mechanical properties of Ti–50 mass% Ta alloy for biomedical applications', *Journal of Alloys and Compounds*, vol. 466, pp. 535-542.
- ⁷⁴ M Niinomi, M Nakai, J Hieda 2012, 'Development of new metallic alloys for biomedical applications', *Acta Biomaterialia*, vol. 8, pp.3888-3903.
- ⁷⁵ CH Park, CS Lee, YJ Kim, JH Jang, JY Suh, JW Park 2011, 'Improved pre-osteoblast response and mechanical compatibility of ultrafine grained Ti–13Nb–13Zr alloy', *Clin. Oral Impl. Res.*, vol. 22, pp. 735–742.
- ⁷⁶ VAR Henriques, ET Galvani, SLG Petroni, MSM Paula, TG Lemos 2010, 'Production of Ti–13Nb–13Zr alloy for surgical implants by powder metallurgy', *J Mater Sci*, vol.45, pp. 5844–5850.
- ⁷⁷ JY Zhang, F Sun, YL Hao, N Gozdecki, E Lebrun, P Vermaut, R Portier, T Gloriant, P Laheurte, F Prim 2013, 'Influence of equiatomic Zr/Nb substitution on superelastic behavior of Ti–Nb–Zr alloy', *Materials Science & Engineering*, vol. 563, pp. 78–85.
- ⁷⁸ MT Mohammed, ZA Khan, AN Siddiquee 2014, 'Beta Titanium Alloys: The Lowest Elastic Modulus for Biomedical Applications: A Review', *International Journal of Materials and Metallurgical Engineering*, vol.8.
- ⁷⁹ A. Robin and O. A. S. Carvalho 2013, 'Influence of pH and Fluoride Species on the Corrosion Behavior of Ti–xNb–13Zr Alloys in Ringer's Solution', *Advances in Materials Science and Engineering*, vol. 2013.
- ⁸⁰ X Rao, CL Chun, YY Zheng 2014, 'Phase composition, microstructure, and mechanical properties of porous Ti–Nb–Zr alloys prepared by a two-step foaming powder metallurgy method', *Journal of Mechanical Behaviour Biomedical Materials*, vol. 37, pp. 27-36.
- ⁸¹ C Ning, D Ding, K Dai, W Zhai, L Chen 2010, 'The effect of Zr content on the microstructure, mechanical properties and cell attachment of Ti–35Nb–xZr alloys', *Biomed. Mater.*, vol. 5.

- ⁸² MA Hussein, AM Kumar, BS Yilbas, N Al-Aqeeli 2017, 'Laser Nitriding of the Newly Developed Ti-20Nb-13Zr at.% Biomaterial Alloy to Enhance Its Mechanical and Corrosion Properties in Simulated Body Fluid', *Journal of Materials Engineering and Performance*, vol.26, pp. 5553–5562.
- ⁸³ JMC Moreno, C Vasilescu, SI Drob, M Popa, P Drob, E Vasilescu 2013, 'Electrodeposition, Characterization, and Corrosion Stability of Nanostructured Anodic Oxides on New Ti-15Zr-5Nb Alloy Surface', *Journal of Nanomaterials*, vol. 2013.
- ⁸⁴ YH Jeong, HC Choe, WA Brantley 2012, 'Electrochemical and surface behavior of hydroxyapatite/Ti film on nanotubular Ti–35Nb–xZr alloys', *Applied Surface Science*, vol. 258, pp. 2129–2136.
- ⁸⁵ K Rajamallu, MK Niranjan, SR Dey 2015, 'First principles theoretical investigations of low Young's modulus beta Ti–Nb and Ti–Nb–Zr alloys compositions for biomedical applications', *Materials Science and Engineering C*, vol. 50, pp. 52–58.
- ⁸⁶ Q Li, M Niinomi, M Nakai, Z Cui, SL Zhu, XJ Yang 2011, 'Improvements in the Superelasticity and Change in Deformation Mode of β -Type TiNb24Zr2 Alloys Caused by Aging Treatments', *Metallurgical and materials transaction*, vol. 42A, pp. 2811–2843.
- ⁸⁷ S Ozan, J Lin, Y Li, R Ipek, C Wen 2015, 'Development of Ti–Nb–Zr alloys with high elastic admissible strain for temporary orthopedic devices', *Acta Biomaterialia*, vol. 20, pp. 176–187.
- ⁸⁸ J Málek, F Hnilica, J Vesely', B Smola, S Bartáková, J Vanek 2012, 'The influence of chemical composition and thermo-mechanical treatment on Ti–Nb–Ta–Zr alloys', *Materials and Design*, vol. 35, pp. 731–740.
- ⁸⁹ LM Elias, SG Schneider, S Schneider, HM Silva, F Malvisi 2006, 'Microstructural and mechanical characterization of biomedical Ti–Nb–Zr(–Ta) alloys', *Materials Science and Engineering*, vol.432, pp. 108–112.
- ⁹⁰ Qing Liu, Qingkun Meng, Shun Guo, Xinqing Zhao 2013, ' α' Type Ti–Nb–Zr alloys with ultra-low Young's modulus and high strength', *Progress in Natural Science, Materials International*, vol. 23, issue 6, pp. 562–565.
- ⁹¹ Product » Vacuum Metallurgy Equipment » Arc Furnace, viewed 30-Sep-2018, <http://www.sky.ac.cn/html/en/index.php?ac=article&at=read&did=377>
- ⁹² J.L. Murry 1987, Phase Diagram of Binary Titanium Alloys, ASM International, Metals Park.
- ⁹³ Peters, M. and Leyens, C. 2003, 'Chapter 8. Fabrication of titanium alloys', *Titanium and Titanium Alloys*, Willey-VCH, Germany, pp. 245–261.
- ⁹⁴ Anand Pai 2016, 'Why is difficult to machining titanium and titanium alloys?', viewed 2-July, https://www.researchgate.net/post/Why_is_difficult_to_machining_titanium_and_titanium_alloys
- ⁹⁵ Wire Cut EDM (Electrical Discharge Machining), viewed: 04-July, <https://www.thomasnet.com/articles/custom-manufacturing-fabricating/Wire-Cut-EDM>
- ⁹⁶ Ho. K. and Newman. S 2003, 'State of the art electrical discharge machining (EDM)', *International Journal of Machine Tools and Manufacture*, 43(13), pp. 1287–1300.
- ⁹⁷ Taylor, B. and Weidmann, E., 2008. Metallographic preparation of titanium, struers application notes. *Struers Den. Rosendahls Bogtryk*.
- ⁹⁸ Goldstein, J. ed., 2012. Practical scanning electron microscopy: electron and ion microprobe analysis. Springer Science & Business Media.
- ⁹⁹ Troubleshooting: edge effect, charging, sample damage, 2014, MyScope training for advanced research, Australian Microscopy and Microanalysis for Research Facility, viewed 15-August, <http://www.ammr.org.au/myscope/sem/practice/principles/troubleshooting.php>.
- ¹⁰⁰ Guo, L., Fan, X., Yu, G. and Yang, H., 2016. Microstructure control techniques in primary hot working of titanium alloy bars: A review. *Chinese Journal of Aeronautics*, 29(1), pp.30–40.
- ¹⁰¹ Kumar, K.H., Wollants, P. and Delacy, L., 1994. Thermodynamic assessment of the Ti-Zr system and calculation of the Nb-Ti-Zr phase diagram. *Journal of alloys and compounds*, 206(1), pp. 121–127.
- ¹⁰² Zhu, Y., Meng, Q., Guo, S., Qi, L., Xiao, W., Ping, D. and Zhao, X., 2016. Anomalous phase stability of surface and interior in a metastable Ti-Nb-Zr alloy. *Materials Letters*, 169, pp.210–213.
- ¹⁰³ Gepreel, M.A.H., 2013. Texturing tendency in β -type Ti-alloys. In *Recent developments in the study of recrystallization*. InTech.
- ¹⁰⁴ Meng, M., Fan, X.G., Yang, H., Guo, L.G., Zhan, M. and Gao, P.F., 2017. Precipitation of secondary alpha in competition with epitaxial growth of primary alpha in two-phase titanium alloys. *Journal of Alloys and Compounds*, 714, pp.294–302.
- ¹⁰⁵ Gammon, L.M., Briggs, R.D., Packard, J.M., Batson, K.W., Boyer, R. and Dombay, C.W., 2004. Metallography and microstructures of titanium and its alloys. *ASM Handbook*, 9, pp.899–917.
- ¹⁰⁶ H. Föll (Iron, Steel and Swords script), Widmanstätten Structure, viewed 3-Oct-2018, https://www.tf.uni-kiel.de/matwis/amat/iss/kap_8/illustr/s8_4_2.html.
- ¹⁰⁷ Pederson, R., 2002. *Microstructure and Phase transformation of Ti-6Al-4V* (Doctoral dissertation, Luleå tekniska universitet).
- ¹⁰⁸ [Damkroger, 1989 #102]
- ¹⁰⁹ Doherty, R.D., Hughes, D.A., Humphreys, F.J., Jonas, J.J., Jensen, D.J., Kassner, M.E., King, W.E., McNelley, T.R., McQueen, H.J. and Rollett, A.D., 1997. Current issues in recrystallization: a review. *Materials Science and Engineering: A*, 238(2), pp.219–274.
- ¹¹⁰ NEWMAN, J. 1994. The influence of grain size and grain size distribution on methods for estimating paleostresses from twinning in carbonates. *Journal of Structural Geology*, 16, 1589–1601.
- ¹¹¹ Ping, D.H., Yamabe-Mitarai, Y., Cui, C.Y., Yin, F.X. and Choudhry, M.A., 2008. Stress-induced α' martensitic (110) twinning in β -Ti alloys. *Applied Physics Letters*, 93(15), p.151911.
- ¹¹² Sun, Q.Y., Song, S.J., Zhu, R.H. and Gu, H.C., 2002. Toughening of titanium alloys by twinning and martensite transformation. *Journal of materials science*, 37(12), pp.2543–2547.
- ¹¹³ Bodnar, R.L. and Hansen, S.S., 1994. Effects of austenite grain size and cooling rate on Widmanstätten ferrite formation in low-alloy steels. *Metallurgical and Materials Transactions A*, 25(4), pp.665–675.
- ¹¹⁴ Prokofeva, I.L., Taratorina, M.V. and Shermazan, I.V., 1978. Effect of martensite needle size on the mechanical properties of steel 45 after induction hardening. *Metal Science and Heat Treatment*, 20(10), pp.795–798.
- ¹¹⁵ Kroggel, R., Schierig, H., Schiffmann, R. and Siebert, P., 1985. Slip bands in quenched Al–Zn alloys. *Crystal Research and Technology*, 20(2), pp.251–254.
- ¹¹⁶ Morsdorf, L., Tasan, C.C., Ponge, D. and Raabe, D., 2015. 3D structural and atomic-scale analysis of lath martensite: effect of the transformation sequence. *Acta Materialia*, 95, pp.366–377.
- ¹¹⁷ Van Grunsven, W., 2014. *Porous metal implants for enhanced bone ingrowth and stability* (Doctoral dissertation, University of Sheffield).
- ¹¹⁸ Courtney, T.H., 2005. *Mechanical behavior of materials*. Waveland Press.
- ¹¹⁹ Girgsdies, F., Peak Profile Analysis in X-ray Powder Diffraction. *Fritz-Haber-Institut der MPG, Berlin*.
- ¹²⁰ Kim, J.I., Kim, H.Y., Hosoda, H. and Miyazaki, S., 2005. Shape memory behavior of Ti–22Nb–(0.5–2.0)O (at%) biomedical alloys. *Materials transactions*, 46(4), pp.852–857.
- ¹²¹ Sun, F., Prima, F. and Gloriant, T., 2010. High-strength nanostructured Ti–12Mo alloy from ductile metastable beta state precursor. *Materials Science and Engineering: A*, 527(16–17), pp.4262–4269.

-
- ¹²² Hao, Y.L., Li, S.J., Sun, S.Y., Zheng, C.Y. and Yang, R., 2007. Elastic deformation behaviour of Ti–24Nb–4Zr–7.9 Sn for biomedical applications. *Acta biomaterialia*, 3(2), pp.277-286.
- ¹²³ Li, S., Hao, Y., Yang, R., Cui, Y. and Niinomi, M., 2002. Effect of Nb on microstructural characteristics of Ti-Nb-Ta-Zr alloy for biomedical applications. *Materials transactions*, 43(12), pp.2964-2969.
- ¹²⁴ Lucca, D.A., Herrmann, K. and Klopstein, M.J., 2010. Nanoindentation: Measuring methods and applications. *CIRP annals*, 59(2), pp.803-819.
- ¹²⁵ Menčík, J., 2012. Uncertainties and errors in nanoindentation. In *Nanoindentation in Materials Science*. InTech.
- ¹²⁶ Qian, L., Li, M., Zhou, Z., Yang, H. and Shi, X., 2005. Comparison of nano-indentation hardness to microhardness. *Surface and Coatings Technology*, 195(2-3), pp.264-271.
- ¹²⁷ Qian, L., Xiao, X. and Wen, S., 2000. Tip in situ chemical modification and its effects on tribological measurements. *Langmuir*, 16(2), pp.662-670.
- ¹²⁸ Qian, L., Xiao, X., Sun, Q. and Yu, T., 2004. Anomalous relationship between hardness and wear properties of a superelastic nickel–titanium alloy. *Applied Physics Letters*, 84(7), pp.1076-1078.